ENDOCYTOSIS

Reticulon 3–dependent ER-PM contact sites control EGFR nonclathrin endocytosis

Giusi Caldieri,[1]* Elisa Barbieri,[1]* Gilda Nappo,[1]* Andrea Raimondi,[4]* Massimo Bonora,[6] Alexia Conte,[1] Lisette G. G. C. Verhoef,[1]† Stefano Confalonieri,[1] Maria Grazia Malabarba,[1,2] Fabrizio Bianchi,[3]‡ Alessandro Cuomo,[3] Tiziana Bonaldi,[3] Emanuele Martini,[1] Davide Mazza,[4] Paolo Pinton,[6] Carlo Tacchetti,[4,5] Simona Polo,[1,2] Pier Paolo Di Fiore,[1,2,3]§‖ Sara Sigismund[1]§‖

The integration of endocytic routes is critical to regulate receptor signaling. A nonclathrin endocytic (NCE) pathway of the epidermal growth factor receptor (EGFR) is activated at high ligand concentrations and targets receptors to degradation, attenuating signaling. Here we performed an unbiased molecular characterization of EGFR-NCE. We identified NCE-specific regulators, including the endoplasmic reticulum (ER)–resident protein reticulon 3 (RTN3) and a specific cargo, CD147. RTN3 was critical for EGFR/CD147-NCE, promoting the creation of plasma membrane (PM)–ER contact sites that were required for the formation and/or maturation of NCE invaginations. Ca^{2+} release at these sites, triggered by inositol 1,4,5-trisphosphate (IP_3)–dependent activation of ER Ca^{2+} channels, was needed for the completion of EGFR internalization. Thus, we identified a mechanism of EGFR endocytosis that relies on ER-PM contact sites and local Ca^{2+} signaling.

Although clathrin-mediated endocytosis (CME) represents the best-characterized internalization route into cells (*1*), several nonclathrin endocytic (NCE) pathways exist that specify diversified functions and/or the fates of individual cargoes (*2*).

Ligand-induced internalization of epidermal growth factor receptor (EGFR) occurs through both CME and NCE, depending on growth conditions and cellular context (*3*–*6*). At a low epidermal growth factor (EGF) dose (1 ng/ml), EGFRs are primarily internalized by CME and recycled back to the plasma membrane (PM), with ~30% of receptors targeted to degradation (*7*). At high physiological EGF concentrations (20 to 100 ng/ml), NCE gets activated in parallel to CME. EGFRs entering via NCE (~40%) are predominantly trafficked to the lysosome for degradation, leading to signal extinction (*7*, *8*). Thus, NCE might serve as a negative regulator of EGFR signaling in response to excessive stimuli.

EGFR-NCE is apparently distinct from other endocytic pathways (table S1). It is cholesterol- and dynamin-dependent, but caveolin-independent, and requires EGFR ubiquitination and proteins harboring ubiquitin-binding domains (*4*, *8*). However, a detailed understanding of its molecular workings is lacking. Such knowledge would help in our understanding of how the cell has developed different mechanisms of endocytosis to control the balance between positive and negative regulation of receptor signaling. Moreover, given the established role of EGFR in oncogenesis (*9*), it might provide insights into possible mechanisms of tumorigenesis, because NCE displays the characteristics of a tumor suppressor mechanism. Here, we provide a comprehensive molecular portrait of the pathway and details of the mechanism underlying NCE.

Results

Molecular characterization of EGFR-NCE

To identify proteins involved in EGFR-NCE, we performed analysis by stable isotope labeling with amino acids in cell culture (SILAC) of purified EGFR-containing NCE vesicles (*10*). Vesicles were purified under conditions of inducible clathrin gene silencing or knockdown (KD) (Fig. 1A and fig. S1). Although this approach only yielded a partially purified vesicle fraction, the high discriminatory power of SILAC allowed us to identify EGFR-NCE candidates by comparing vesicles from EGF-stimulated clathrin KD cells versus unstimulated cells, which represented the "background" (Fig. 1B).

Three experiments yielded overlapping proteomes (~60%) (Fig. 1C and table S3, spreadsheet 1), with a bimodal distribution of SILAC ratios (Fig. 1D and table S3, spreadsheet 2). The major peak, centered on a high-to-low (H/L) ratio of ~1 (log_2 ratio of ~0), represents proteins equally present in the two samples (presumably contaminants); the minor peak, centered on H/L ratio ~2.3 (log_2 ratio ~1.2), should be enriched in EGFR-NCE components. To select candidates for validation, we applied high-confidence filters: proteins present in the top 20%, ranked by H/L ratios, in three out of three replicates and robustly quantified [ratio count (RC) >2]. This selection process yielded 151 proteins (Fig. 1D and table S3, spreadsheet 3), of which 101 were tested in validation experiments (table S3, spreadsheets 3 and 4).

Validation of SILAC candidates

To validate candidates, we silenced their expression in inducible clathrin KD cells and analyzed EGFR internalization following stimulation with high-dose EGF [fig. S2A (1)]. We scored an effect on EGFR-NCE for 43 candidates (table S4, spreadsheets 1 and 2). These candidates were then screened for their effects on (i) EGFR-NCE upon transient clathrin KD (to obtain replicates and exclude clonal effects); (ii) EGFR-CME at low EGF doses; (iii) transferrin receptor (TfR)–CME; and (iv) surface EGFR number, because this might affect the internalization constants [fig. S2A (2), and table S4, spreadsheets 3 to 9]. After deconvolution analysis [fig. S2A (3)], we derived a list of nine EGFR-NCE regulators, which included signal-transduction, RNA-binding, and endoplasmic reticulum (ER)–mitochondrial proteins (Fig. 2A), not previously implicated in internalization pathways (table S1 and fig. S2, D to G).

RTN3 is a critical regulator of EGFR-NCE

Of the nine candidate EGFR-NCE regulators, the ER tubulation factor reticulon 3 (RTN3) (*11*) showed one of the strongest phenotypes (Fig. 2A). KD of RTN3 resulted in ~50% reduction in EGF internalization at a high dose (Fig. 2B), compatible with the proportion of EGFRs entering via NCE (*4*). The double RTN3 and clathrin KD reduced EGF internalization almost to the levels observed under dynamin KD (Fig. 2, B and C, and fig. S2B), demonstrating its requirement for EGFR-NCE. Conversely, RTN3 KD had a minor impact on EGFR internalization at low EGF doses and no effect on transferrin (Tf) internalization (Fig. 2, B and D).

Another ER-shaping factor, REEP5, also had a substantial effect on NCE (Fig. 2A). RTN3 and REEP5 form a complex with another reticulon, RTN4, and this complex is implicated in cortical ER tubulation (*11*, *12*). However, RTN4 KD did not affect EGFR internalization (Fig. 2B and fig. S2C), which indicates a specific function of RTN3 and REEP5 in NCE.

NCE preferentially targets EGFRs to degradation (*7*). Accordingly, RTN3 KD delayed EGFR and EGF degradation (Fig. 2, E and F), reduced EGFR trafficking toward multivesicular bodies (MVBs) (fig. S3A), and increased EGF-induced signaling (Fig. 2G).

[1]Fondazione Istituto FIRC di Oncologia Molecolare (IFOM), Via Adamello 16, 20139 Milan, Italy. [2]Dipartimento di Oncologia ed Emato-Oncologia (DiPO)—Università degli Studi di Milano, Via Festa del Perdono 7, 20122 Milan, Italy. [3]Istituto Europeo di Oncologia, Via Ripamonti 435, 20141 Milan, Italy. [4]Centro Imaging Sperimentale, Istituto Scientifico San Raffaele, Via Olgettina 52, 20132 Milan, Italy. [5]Dipartimento di Medicina Sperimentale, Università degli Studi di Genova, Genoa, Italy. [6]Section of Pathology, Oncology and Experimental Biology and Laboratory for Technologies of Advanced Therapies Center, Department of Morphology, Surgery and Experimental Medicine, University of Ferrara, Ferrara, Italy.
*These authors contributed equally to this work.
†Present address: Center for Genomic Science of IIT@SEMM, Istituto Italiano di Tecnologia, Via Adamello 16, 20139 Milan, Italy.
‡Present address: SBReMIT—Institute for Stem-Cell Biology, Regenerative Medicine and Innovative Therapies, Casa Sollievo della Sofferenza, Viale Cappuccini s.n.c., 71013 San Giovanni Rotondo, Foggia, Italy. §These authors contributed equally to this work. ||Corresponding author. Email: sara.sigismund@ifom.eu (S.S.); pierpaolo.difiore@ifom.eu (P.P.D.F.)

RTN3 is required for the maturation of NCE intermediates at the PM

We characterized EGFR-NCE by electron microscopy (EM). In control cells, gold-labeled EGFR was detectable in clathrin-coated pits (CCPs) and in tubular invaginations [(TIs); diameter ≈ 80 nm] (Fig. 3, A and B, and fig. S3B). TIs persisted in clathrin KD cells (Fig. 3, A and B), which suggests that they might represent the structures mediating EGFR-NCE. TIs are morphologically reminiscent of clathrin-independent carriers (*13*, *14*), although the two pathways show distinct functional requirements (table S1) (*15*).

In RTN3 KD cells, TIs were significantly reduced in number (Fig. 3, A and B), whereas no effect was observed on CCPs (Fig. 3B), which indicates that TIs are NCE intermediates whose formation and maturation are RTN3-dependent. Note that dynamin KD did not reduce TI number (Fig. 3B); rather, it increased the ratio of long (>300 nm) versus short TIs (~150 to 300 nm) (Fig. 3C). A similar phenotype was observed for CCPs, with a shift toward longer CCPs (>200 nm) (Fig. 3C), as previously reported (*16*). These data argue that dynamin is involved in the fission of TIs (and CCPs), whereas RTN3 could act upstream, at the level of TI maturation. Indeed, the RTN3 KD phenotype appeared epistatic to the dynamin one, because the double KD RTN3 and dynamin closely resembled the single RTN3 KD phenotype (Fig. 3B).

We then followed gold-EGFR internalization by discriminating PM-connected from internalized structures with ruthenium red (RuR) (fig. S3, C and D). In control cells, EGFR present in RuR-positive structures (CCPs and TIs) decreased over time, with a parallel increase of internalized receptors (Fig. 3, D and E, and fig. S3D). In clathrin KD and RTN3 KD cells, gold-EGFR in intracellular structures significantly decreased (~50%), accompanied by an increase in RuR-positive structures (Fig. 3, D and E, and fig. S3D), consistent with the inhibition of CME and NCE, respectively. In double clathrin and RTN3 KD cells, internalization was almost completely blocked (>80%), in agreement with ^{125}I-labeled EGF internalization assays (Fig. 3F).

RTN3 localizes in close proximity to active EGFR

By immunofluorescence (IF), we confirmed that RTN3 is an ER-resident protein (fig. S3, E to G), located in the peripheral ER and colocalized with cortical ER markers involved in ER-PM contact sites, namely, E-Syt1 and STIM1 [fig. S3F and (*17*, *18*)]. This result was verified by immuno-EM, which showed that RTN3 was exclusively associated with ER, and no PM signals, above background, could be evidenced (fig. S3H).

By proximity ligation assays, RTN3 and activated EGFR were found in close proximity (within ~30 nm) upon EGF stimulation (fig. S4A). To better define the RTN3 and EGFR association, we used superresolution microscopy and Förster resonance energy transfer (FRET). With the first approach, we observed, with high-EGF use, increased coclustering of EGFR and RTN3 [amplitude of the correlation (C_0)] and an increase of cluster size (R_c) at the cell periphery versus cells stimulated with low EGF dose or unstimulated (Fig. 4A). By FRET, a higher signal between RTN3 and EGFR was registered with high EGF dose compared with basal conditions (Fig. 4B). The signal was specific, because no signal was detectable for the pair TfR-RTN3 (fig. S4B). The EGFR-RTN3 FRET signal is compatible with the scenario that peripheral ER comes into close proximity with active EGFR on EGF stimulation. Indeed, other cortical

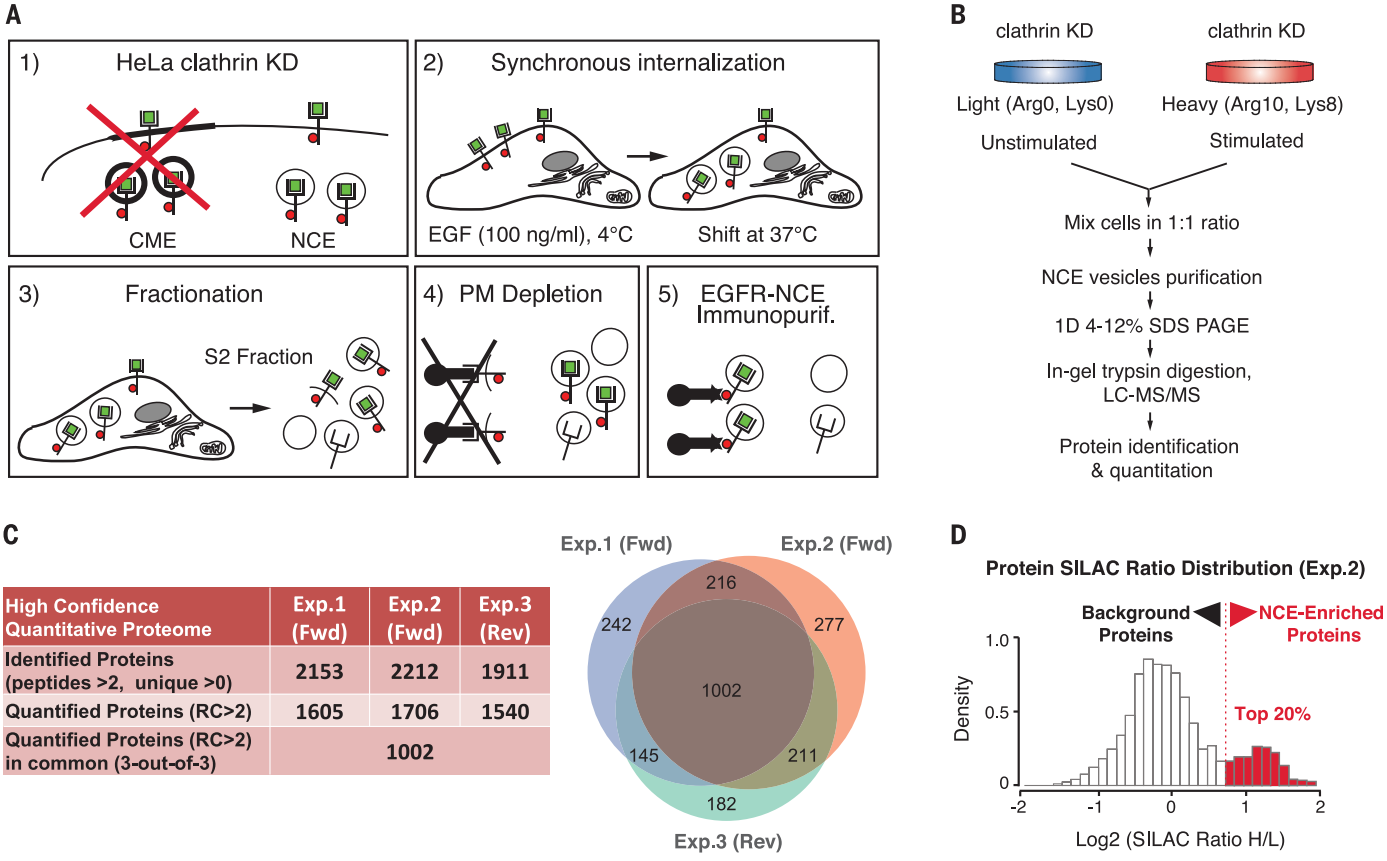

High Confidence Quantitative Proteome	Exp.1 (Fwd)	Exp.2 (Fwd)	Exp.3 (Rev)
Identified Proteins (peptides >2, unique >0)	2153	2212	1911
Quantified Proteins (RC>2)	1605	1706	1540
Quantified Proteins (RC>2) in common (3-out-of-3)	1002		

Fig. 1. Molecular components of EGFR-NCE. (**A**) Purification of NCE vesicles. Clathrin KD HeLa cells (1) were subjected to a synchronous wave of EGFR internalization (2), and then to subcellular fractionation (3), to obtain the S2 fraction. The S2 fraction was subjected to a PM depletion step with antibody against the extracellular domain of EGFR (anti-EGFR) (4), and to immunopurification with anti–phospho-EGFR (5). (**B**) SILAC-MS analysis; EGF stimulation and vesicle purification were as in (A). SDS-PAGE, SDS–polyacrylamide gel electrophoresis; LC, liquid chromatography; MS/MS, tandem mass spectrometry. (**C**) Numbers of quantified proteins in three SILAC experiments (two forward, Fwd; one reverse, Rev). Venn diagram: overlap among the identified proteins. (**D**) SILAC H/L ratios, distribution of all proteins confidently quantified (RC > 2) in Exp. 2 (other experiments are in table S3, spreadsheet 2). The enriched proteins (top 20%) are in red.

ER proteins (RTN4, STIM1, and E-Syt1) gave a positive FRET signal within 5 min of EGF stimulation (Fig. 4B and fig. S4C), whereas proteins not enriched in peripheral ER did not (Fig. 4B and fig. S4C). When we restricted FRET analysis to the PM regions where EGFR is active (by applying a PM EGF-based mask, excluding endosomes) and followed the FRET signal kinetically in the initial phases of EGF stimulation (first 3 min), RTN3 was the sole marker that gave a significant FRET signal (Fig. 4C). In agreement, the KD of E-Syt and STIM proteins—as in the case of RTN4—did not affect EGFR endocytosis (Fig. 2B and fig. S4D).

RTN3 is required for ER-PM contact sites where EGFR-NCE occurs

The above results are compatible with the formation of RTN3-dependent EGF-induced contact sites between peripheral ER and NCE-TIs. We transfected cells with horseradish peroxidase (HRP)–labeled KDEL peptide sequence (*17*, *19*) to visualize the ER and detected areas of ER-PM proximity, in regions that either contained or did not contain the EGFR (fig. S5A). Initially, we explored the effect of RTN3 KD on general ER morphology, in parallel with RTN4 KD, which was previously shown to affect ER architecture by skewing ER peripheral tubules toward cisternae (*20*). We confirmed the RTN4 KD phenotype in our cell system by three-dimensional (3D) ER reconstruction, as evidenced by an increase in long ER profiles (>1000 nm) with a concomitant decrease in shorter profiles (fig. S5B). Conversely, in RTN3 KD cells, we did not observe major rearrangements in the distribution of ER profiles, and this confirms previously reported results obtained in RTN3 knockout mouse embryonic fibroblasts (fig. S5B) (*21*).

However, automated ER segmentation analysis on high-resolution images revealed that both RTN3 and RTN4 KD reduced the number of small tubular ER profiles, whereas only RTN4 KD increased large ER sheets (fig. S5C). EGF stimulation caused an increase in tubular ER profiles within 20 nm of the PM, consistent with the formation of EGF-induced ER-PM contact sites. Although RTN3 and RTN4 KD had a similar impact on the tubulation of peripheral bulk ER (fig. S5C), only RTN3 KD reduced the number of EGF-induced ER-PM contact sites (Fig. 4D).

Finally, we investigated the existence of specific RTN3-dependent contacts between ER and EGFR-NCE structures by performing serial sections and quantification of contacts between the ER (HRP-KDEL) and gold-EGFR–positive PM invaginations (NCE-TIs or CCPs). Serial sectioning allowed us to detect contact sites even when gold-labeled EGFR and ER were not visible in the same section (Fig. 4E and fig. S5D). We considered as "contacts" those instances in which ER proximity (≤20 nm) to gold-EGFR–positive PM invaginations was present in at least one out of three sections (Fig. 4E). About 20% of the EGFR-containing PM-TIs were in contact with tubular ER, whereas there were no contacts between ER and CCPs. In RTN3 KD cells, the remaining TIs

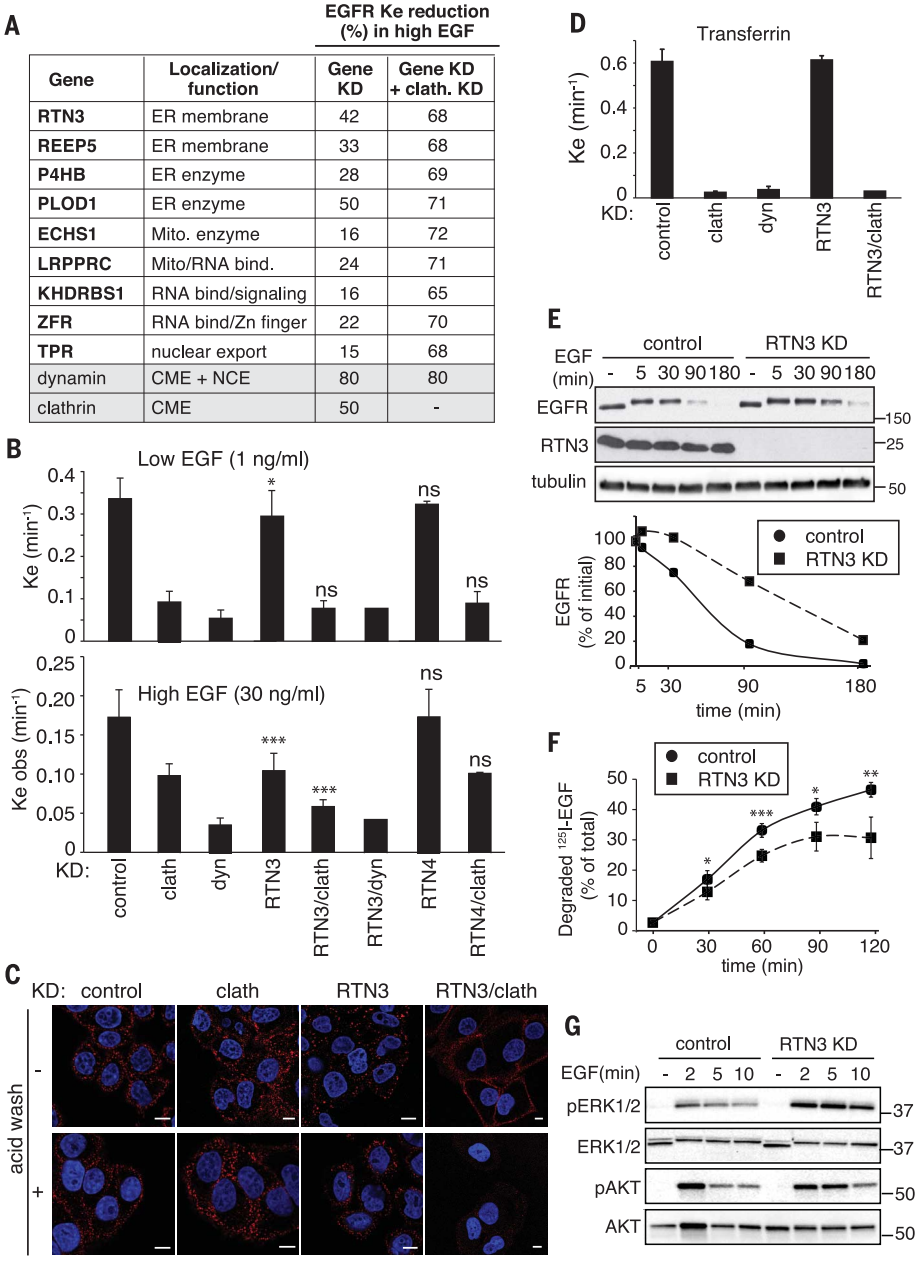

Fig. 2. RTN3 and EGFR-NCE. (**A**) EGFR-NCE regulators are shown. EGFR internalization is expressed as the reduction in the endocytic rate constant (K_e) versus control (measured at high EGF, by ^{125}I-labeled EGF internalization assays). Clathrin and dynamin, controls. (**B**) Internalization constants at low- and high-EGF doses upon the indicated KDs. Clath, clathrin; dyn, dynamin. Here and in the other panels, data are means ± SD and *P* values were calculated using each-pair Student's *t* test. *P* values are for RTN3 or RTN4 versus control; RTN3/clathrin or RTN4/clathrin versus clathrin; ***$P < 0.001$; *$P < 0.05$; ns, nonsignificant. (**C**) Internalization of Alexa555-EGF (red) 8 min after stimulation, in the indicated conditions. Scale bar, 10 μm. DAPI, 4′,6-diamidino-2-phenylindole (blue). (**D**) K_e of ^{125}I-labeled Tf internalization in the indicated conditions. Data are means ± SD. (**E**) (Top) EGFR degradation (EGF, 100 ng/ml). (Bottom) Densitometric quantification, expressed as the percentage of EGFR levels relative to the initial amount. (**F**) Quantitative ^{125}I-labeled EGF degradation assay. Data are expressed as the percentage of degraded EGF. *$P < 0.05$, **$P < 0.01$, ***$P < 0.001$ (versus control). (**G**) Analysis of EGF-dependent signaling in the indicated conditions (EGF, 100 ng/ml). ERK, extracellular signal–regulated kinase; pERK, phosphorylated extracellular signal–regulated kinase; pAkt, phosphorylated Akt.

were not in contact with ER (Fig. 4E and fig. S5D for distance-dependent analysis). Serial sectioning is prone to underestimate the phenomenon, because we inevitably lose some of the contacts between two consecutive sections (thickness of ~60 nm). Indeed, by performing tomograms (*z*-axis resolution of ~3 to 6 nm) of 11 randomly selected CD147-positive TIs, we found that 8 out of the 11 TIs were in contact with an ER tubule (~70%) (see fig. S6, for extracts from four representative tomograms, and movie S1).

CD147, a cargo internalizing through NCE

In the initial candidate list, there were many PM-resident proteins whose ablation did not alter EGFR-NCE. These proteins might represent cargoes of this pathway. As proof of principle of this concept, we focused on cluster of differentiation 147 (CD147), also known as basigin (BSG).

CD147 colocalized with internalized EGF in clathrin KD cells (fig. S7A), which suggests that it cotraffics with the EGFR through NCE. Thus, we followed CD147 endocytosis with an antibody that recognizes its extracellular domain without interfering with endocytosis (*22*). Upon EGF stimulation, CD147 was internalized and colocalized with EGF via a clathrin-independent process that was sensitive to RTN3 KD (Fig. 5, A and B, and fig. S7B for controls). Note that CD147-EGFR internalization in RTN3 KD cells was restored by the reintroduction of RTN3A, which is the most-expressed RTN3 isoform in HeLa cells (Fig. 5C and fig. S8, A to C).

Thus, upon EGF stimulation, CD147 enters the cell almost exclusively through NCE and can be used as a specific marker of this pathway. We exploited CD147 internalization as an independent tool for the validation of the functional role of candidate NCE regulators. Silencing of the nine regulators affected CD147 internalization upon EGF stimulation, corroborating their role in NCE and providing a cross-validation of both functional regulators and cargo (fig. S9A).

We then used CD147 for EM analysis. By double PM RuR-CD147 (immunogold) staining, we found that after 5 min of EGF stimulation, CD147 was either at the PM or in TIs indistinguishable from those observed for the EGFR-NCE (Fig. 5D and fig. S9B), but not in CCPs. RTN3 KD reduced the formation of CD147-positive TIs (Fig. 5D), which indicates that TIs are indeed endocytic intermediates of CD147. Quantification of gold particles in PM-connected versus internalized structures revealed that ~75% of CD147 was at the PM or in PM-connected TIs, with ~25% of gold particles internalized at 5 min (fig. S9C). Ablation of RTN3 almost completely blocked CD147 at the PM at all time points analyzed, whereas clathrin KD had no effect (fig. S9C). A time-resolved EM analysis showed a progressive reduction of CD147 at the PM, concomitant with its recruitment to TIs, followed by its accumulation in early endosomes (EEs) and, later, in multivesicular bodies (MVBs) (Fig. 5E), arguing for CD147 endocytic progression. RTN3 KD strongly affected CD147 accumulation in the different compartments, while leaving unaltered its PM localization (Fig. 5E).

Finally, we analyzed the proximity between CD147-containing NCE structures and the ER. We observed a significant increase in ER-PM contacts upon 2 and 5 min of EGF stimulation at CD147-internalizing sites (Fig. 5F and fig. S9D), as also shown by 3D reconstruction of a CD147-positive TI (Fig. 5G, fig. S9E, and movie S1). This phenotype was abolished by RTN3 KD (Fig. 5F) but not by RTN4 KD (fig. S9F), which had no effect on CD147 internalization (fig. S9G). Three other human epithelial cell lines, HaCaT (skin keratinocytes), BT20 (breast cancer), and A431 (skin squamous carcinoma),

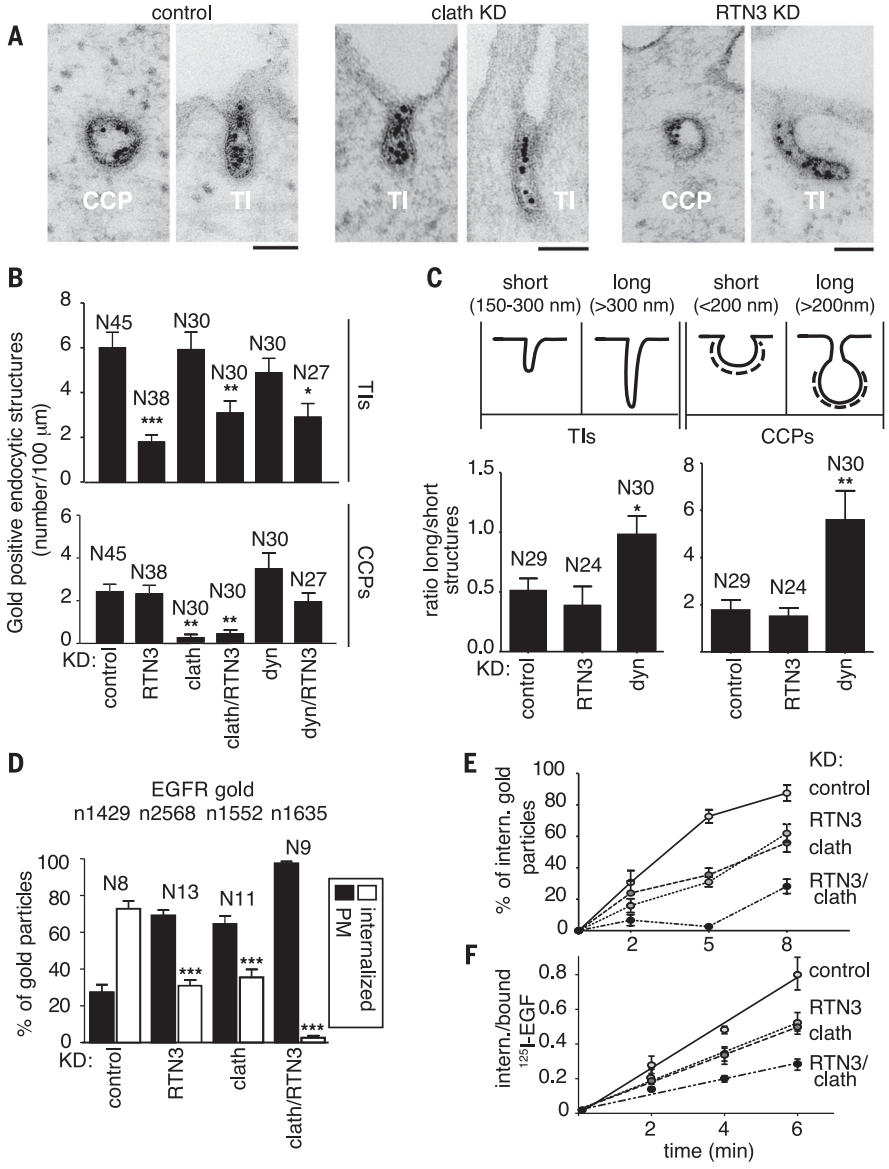

Fig. 3. Characterization of EGFR-NCE by EM. (**A**) Representative EGFR endocytic structures, upon high-dose EGF. Scale bar, 100 nm. (**B**) Quantification of gold-labeled EGFR-positive TIs and CCPs (5 min of high EGF). Only RuR-stained structures were counted. *N*, cell profiles analyzed. Data are expressed as the number of gold-positive structures, normalized to PM profiles of 100-µm length, ± SEM. Here and in the other panels, *P* values were calculated using one-way analysis of variance (ANOVA). **P* < 0.05, ***P* < 0.01, ****P* < 0.001 (versus control). (**C**) Morphometric analysis of the length of EGFR gold-positive TIs and CCPs (top). (Bottom) Data are expressed as the ratio between the number of long or short structures normalized to PM profiles of 100-µm length ± SEM. *N*, cell profiles analyzed. **P* < 0.05, ***P* < 0.01 (versus control). (**D**) Quantification of PM versus internalized EGFR (gold-labeled) upon high-dose EGF (5 min). Data are the means ± SEM. *N* and *n*, cell profiles and gold particles, respectively. ****P* < 0.001, RTN3 KD or clathrin KD versus control, RTN3+clathrin KD versus clathrin KD (or RTN3 KD). (**E**) Percentage of internalized gold particles as a function of time of EGF stimulation. (**F**) ^{125}I-labeled EGF internalization kinetics at high-dose EGF.

activated the EGFR/CD147-NCE pathway at high EGF doses in a RTN3-dependent manner (table S2).

ER contact sites are involved in local Ca^{2+} release required for NCE progression

ER contact sites have a fundamental role in localized Ca^{2+} release (*23*), which might be relevant to EGFR-NCE. To investigate this, we exploited the Ca^{2+} sensor aequorin, either in a cytoplasmic version (cyto-Aeq) or targeted to the inner leaflet of the PM (PM-Aeq) (fig. S10A); both forms display the same affinity for Ca^{2+} (*24*). We found that (i) PM-Aeq detected a peak of Ca^{2+} release induced by high, but not low, EGF doses (Fig. 6A and fig. S10B); (ii) the Ca^{2+} peak was higher when detected with PM-Aeq versus cyto-Aeq (Fig. 6A), which suggests that it mainly occurs in proximity to the PM; (iii) the calcium (Ca^{2+}) flux did not come from the extracellular space, which was shown by using the Ca^{2+}-chelator EGTA, which did not affect peak intensity (fig. S10C); and (iv) RTN3, but not RTN4, KD strongly impaired the EGF-induced Ca^{2+} response (Fig. 6B and fig. S10D).

These results are compatible with the possibility that Ca^{2+} is released at the PM from the ER, through the formation of EGF-induced RTN3-dependent contact sites. This might occur through the activation of the inositol triphosphate (IP_3) receptor (IP3R), which is the main pathway promoting Ca^{2+} release from the ER in HeLa cells (*25*). Indeed, IP3R inhibition by xestospongin C strongly affected EGF-induced Ca^{2+} flux at the PM, comparable to RTN3 KD (Fig. 6C), without impairing ER-PM contact site formation at areas of NCE, which indicates that Ca^{2+} release is downstream of RTN3-dependent contact site formation (Fig. 6D). IP3R inhibition did not affect NCE-TI formation (Fig. 6E), but it prevented progression of NCE internalization (Fig. 6, F and G, and fig. S10E) by blocking the fission of TIs (xestospongin C treatment phenocopies dynamin KD, causing TI elongation) (Figs. 6H and 3C), whereas it has limited impact on CME of EGFR and TfR (fig. S10, E and F).

Discussion

We report here the molecular characterization of EGFR-NCE. We found that proteins previously not suspected to participate in endocytosis are required, among which is the ER-resident protein RTN3. We show that at least another cargo, CD147, is trafficked through the same route.

The pathway relies on the establishment of specific RTN3-dependent ER-PM contact sites. A relevant question concerns the mechanistic role of RTN3 in EGFR-NCE. One possibility is that RTN3 might act as a tethering factor between the ER and PM, in regions where EGFR signaling occurs. In favor of this, we showed close proximity between RTN3 and activated EGFR, as well as specific FRET between the RTN3-EGFR pair at the PM. RTN3-dependent contacts involved in EGFR-NCE do not show physical or functional overlap with STIM1- or E-Syt1–dependent

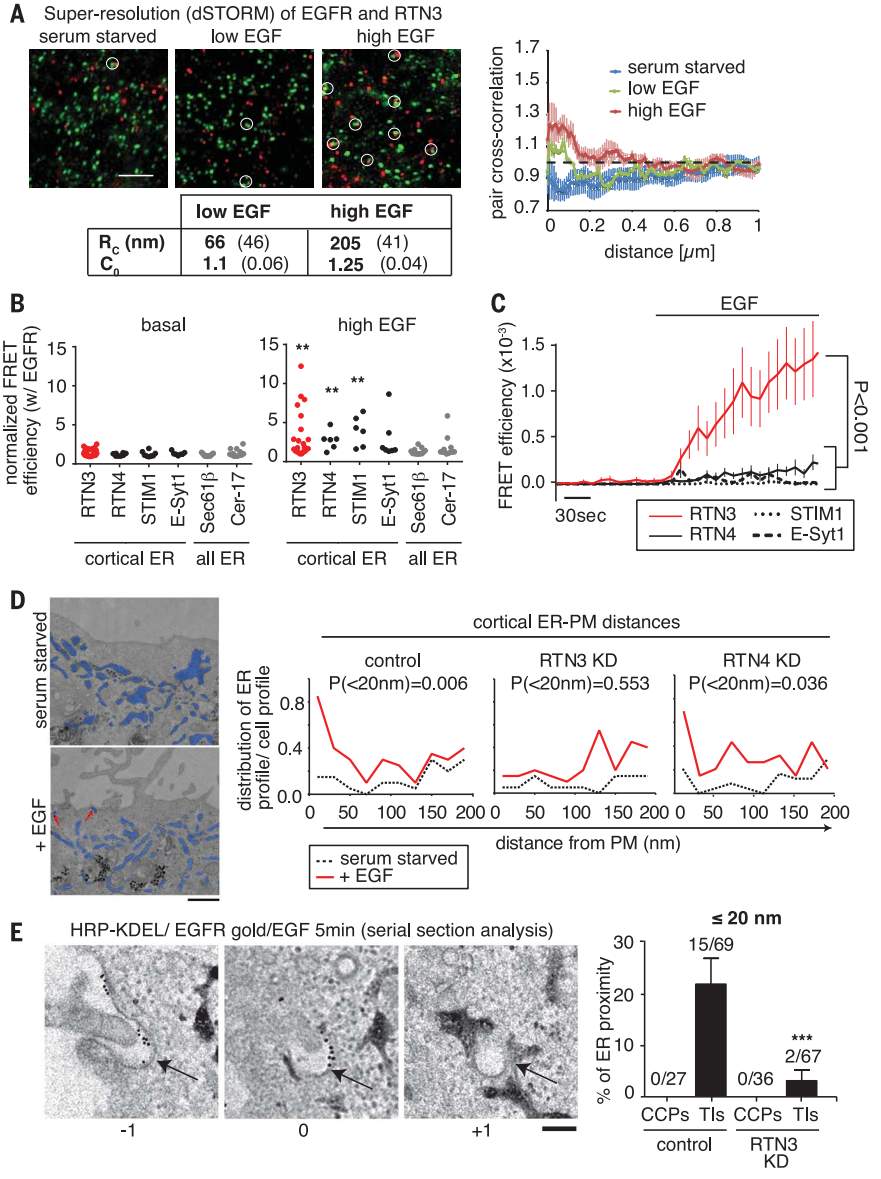

Fig. 4. RTN3-mediated contacts at site of EGFR-NCE. (**A**) Direct stochastic optical reconstruction microscopy (dSTORM) of RTN3 (green) and EGFR (red). (Left) Images of cells in the indicated conditions. Scale bar, 0.7 μm. (Right) Cross-correlation between the two channels as a function of distance (*29*). (Bottom left) C_0, amplitude of the correlation, proportional to the fraction of coclustered RTN3 or EGFR signals, and R_c, spatial extent of the cross-correlation curve, which is an estimate of cocluster size. The 95% confidence intervals (CIs) are in parentheses. (**B**) Sensitized emission FRET analysis (SE-FRET). The normalized SE-FRET efficiencies of EGFR-EYFP with the indicated ECFP-tagged constructs or cerulean-17 (Cer-17) before (basal on left) and after 5-min stimulation with a high dose of Alexa555-EGF (high EGF on right). RTN3 (red), cortical ER-enriched proteins ("cortical ER," black), non–cortical-enriched ER proteins ("all ER," gray). *P* values were calculated by two-tailed Student's *t* test. $^{**}P < 0.01$ (EGF-stimulated versus basal condition). (**C**) Proximity measurement at the PM. SE-FRET as in (B) was restricted to PM regions where EGFR is activated and to 3 min of EGF stimulation. *P* values were calculated by one-way ANOVA. (**D**) (Left) Representative EM images showing distribution of juxta-PM ER profiles. Blue, general ER profiles; arrows indicate ER profiles <20 nm from the PM. Scale bar, 1 μm. (Right) Number of ER profiles at various distances from the PM in 20 random images per condition with or without EGF stimulation. *P* value for EGF-stimulated versus unstimulated cells (Mann-Whitney test). (**E**) (Left) Representative serial sections showing contacts (≤20 nm) between ER and gold-EGFR–positive structures. Arrows indicate the same structure across sections. Scale bar, 100 nm. (Right) Mean frequency of ER proximity with gold EGFR–labeled CCPs or TIs at 5 min of EGF stimulation, expressed as percentage ± SEM. The number of counted structures in contact with the ER is indicated (distance ≤ 20 nm). *P* values were calculated by two-tailed Student's *t* test. $^{***}P < 0.001$ (versus control TIs).

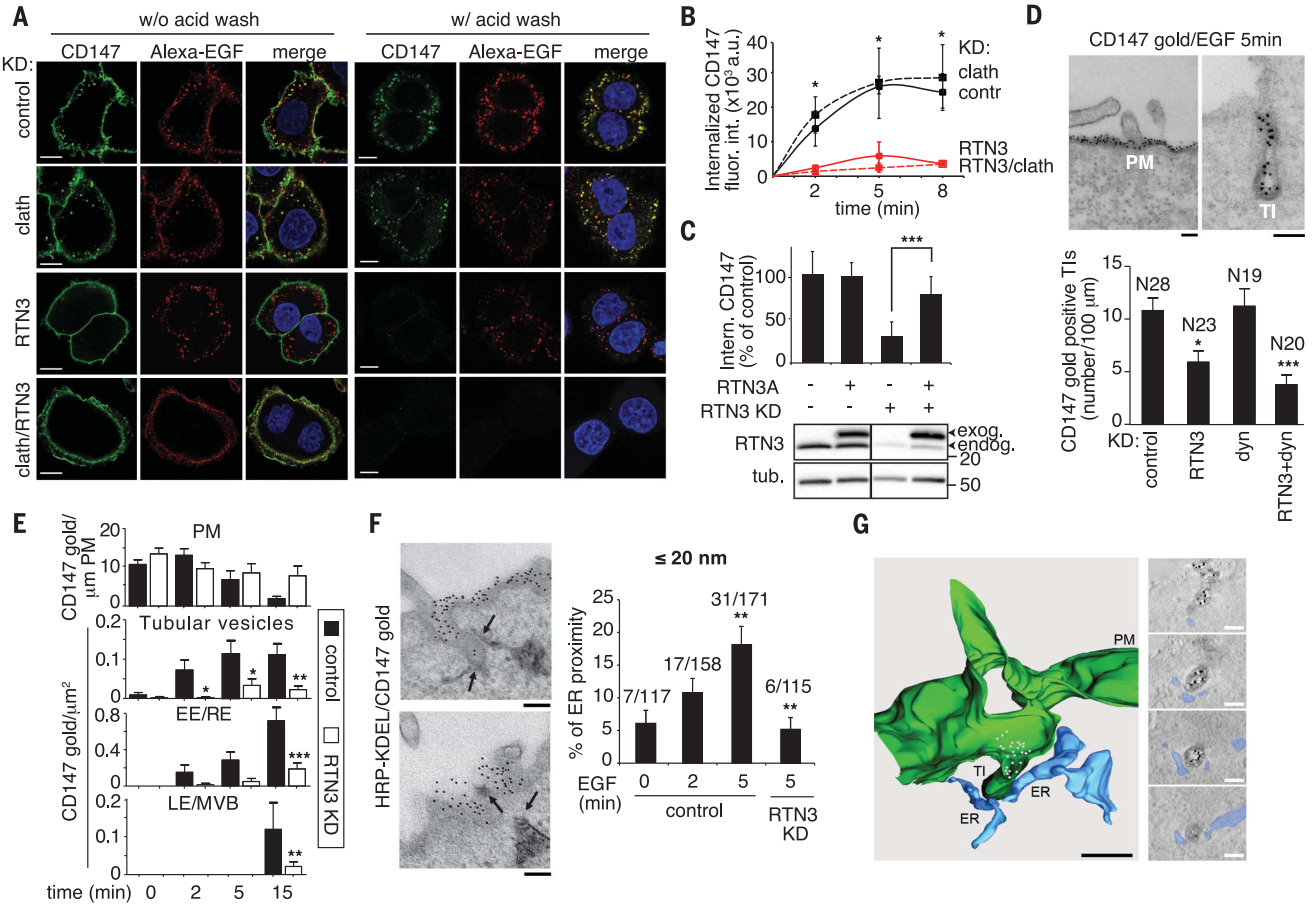

Fig. 5. RTN3-dependent CD147 internalization. (**A**) CD147 (green) internalization at 8 min of Alexa555-EGF. Before fixation, cells were acid-washed (to eliminate PM-EGF/CD147) or untreated. Scale bars, 10 µm. Blue, DAPI. (**B**) Time course of CD147 internalization after EGF addition. Mean integrated fluorescence intensity ± SD is reported (a.u., arbitrary units). *P* values were calculated for each pair by Student's *t* test. **P* < 0.05 (RTN3 versus control). (**C**) Rescue of CD147 internalization in RTN3 KD cells upon expression of RNA interference–resistant RTN3-isoform A (fig. S8, A and B). (Top) Quantification as in panel (B). Integrated fluorescence intensity was reported as percent of each control line ± SD. *P* values were calculated by two-tailed Student's *t* test. ****P* < 0.001. (Bottom) RTN3 endogenous and exogenous levels (arrows) were analyzed by IB. This panel was assembled from samples run on the same gel by splicing out the irrelevant lanes. (**D**) (Top) EM representative images of CD147-positive structures in high-EGF–stimulated cells (5 min). Scale bars, 100 nm. (Bottom) Quantification of RuR-stained gold-CD147–positive TIs. *N*, cell profiles analyzed. Data are expressed as the number of gold-positive structures per PM profiles of 100-µm length ± SEM. *P* values were calculated by two-tailed Student's *t* test. **P* < 0.05; ****P* < 0.001 (versus control). (**E**) Quantification of gold-CD147 ± SEM in control and RTN3 KD cells. *P* values were calculated by one-way ANOVA. **P* < 0.05; ***P* < 0.01; ****P* < 0.001 (RTN3 KD versus control). (**F**) (Left) Representative contact sites between ER and gold-CD147–labeled structures. Scale bar, 100 nm. (Right) Mean frequency of the proximity between ER and CD147-positive structures upon high-EGF dose. Data are expressed as percentages ± SEM. ***P* < 0.01 (one-way ANOVA, control 2 min or 5 min versus control 0 min; two-tailed Student's *t* test, RTN3 versus control at 5 min). (**G**) 3D reconstruction of a CD147-positive (white dots) TI at the PM (green) in contact with the ER (light blue). Scale bar, 200 nm. Slices of the tomogram are provided on the right (ER pseudocolored in blue). Scale bars, 100 nm.

contact sites, in agreement with the current idea of contact site specificity (*17*).

Another possibility is that RTN3 acts in NCE through its "canonical" ER tubulation function. The strongest evidence in this direction is that RTN3 is required for the formation of cortical ER tubules induced by EGF. If this were the case, our data suggest that there must be specificity embedded in the system, because RTN4 KD did not phenocopy the RTN3 KD. In such a scenario, EGFR-emanating signals—whose nature remains to be determined—might exist that induce ER tubulation at specific sites and by dedicated factors.

RTN3-dependent ER-PM contacts are critical for TI formation. In this context, ER-PM contact sites may serve as an anchor to provide the pulling force required for TI elongation. In addition, these contacts might be involved in one of the emerging functions of ER-biomembrane contacts, which include phosphoinositide and Ca^{2+} signaling, lipid or protein translocation, or in trans regulation of protein function (*23*). We characterized one such function by establishing that RTN3-mediated ER contacts are involved in EGF-induced local Ca^{2+} release from the ER (IP3R-mediated) to the PM, which occurs only at high EGF dose and is in turn required to finalize the last step of EGFR-NCE, i.e., the fission of TIs. Thus, there is stepwise requirement of RTN3-dependent contact sites in EGFR-NCE (Fig. 6I): (i) TI formation and/or maturation; (ii) Ca^{2+} release at the ER-PM interface, which is in turn required for (iii) the fission of TIs and the completion of the internalization step. Our data provide evidence for a positive-feedback loop between EGFR-NCE and Ca^{2+} signaling: NCE regulates local Ca^{2+} release at ER-PM contact sites, and, in turn, Ca^{2+} flux is required to finalize EGFR-NCE. It is noteworthy that ER-endosome contact sites have been shown to regulate EGFR signaling and trafficking also

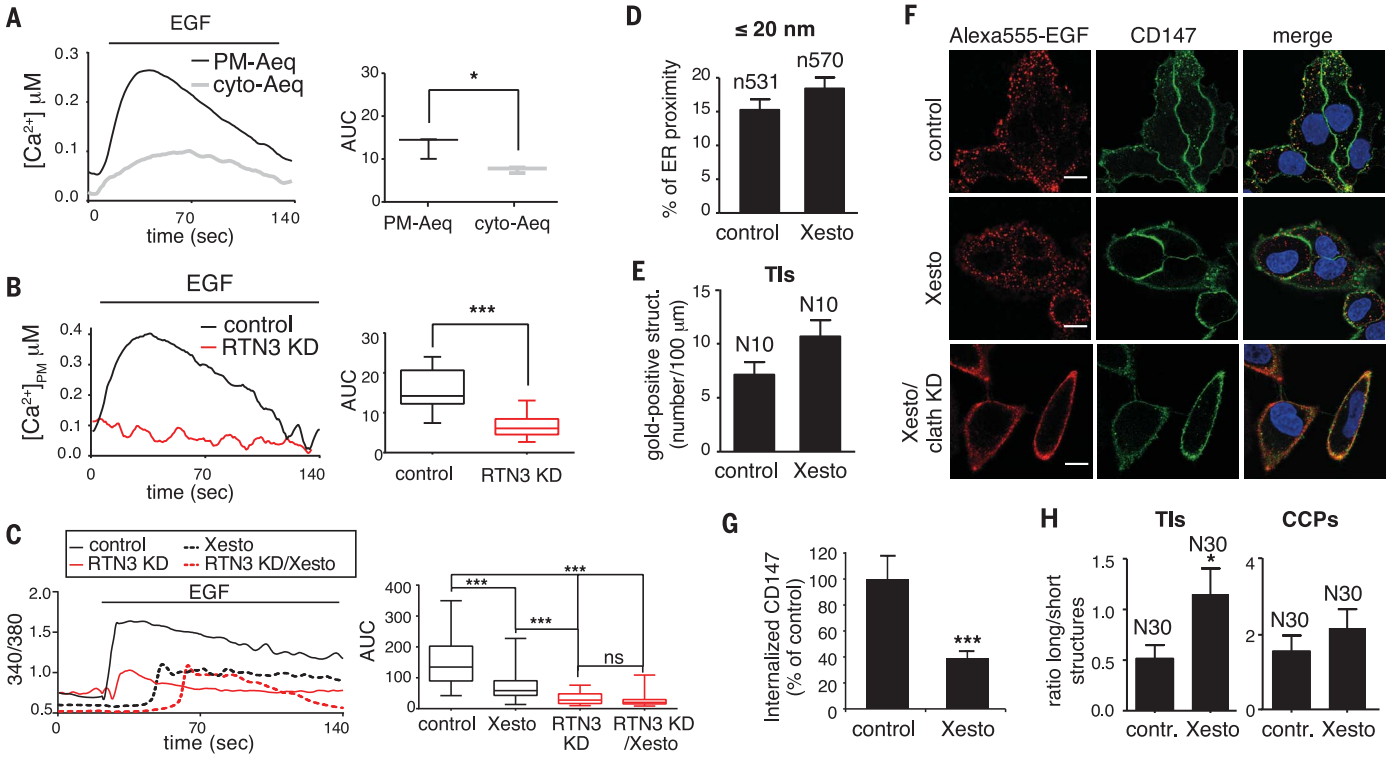

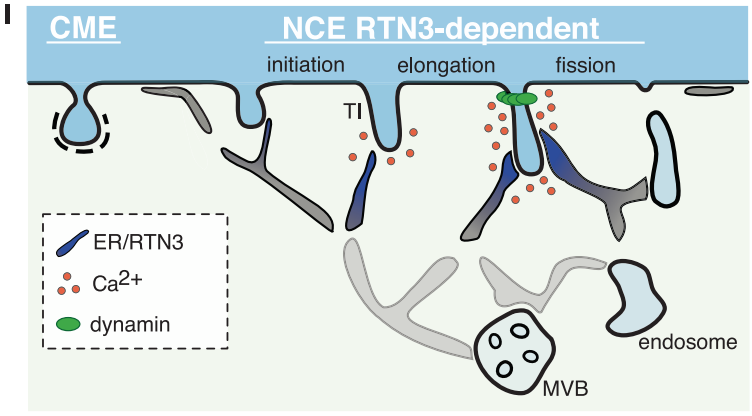

Fig. 6. RTN3 is required for EGF-induced Ca^{2+} release at ER-PM contact sites. (**A**) (Left) Measurements of [Ca^{2+}] upon high-dose EGF (100 ng/ml), with cytosolic aequorin (cyto-Aeq, gray) or PM-targeted aequorin (PM-Aeq, black). (Right) Area under the curve (AUC). Here and in (B), *P* values were calculated by two-tailed Student's *t* test. **P* < 0.05. (**B**) (Left) Measurements of PM [Ca^{2+}] with PM-aeq upon high-dose EGF (100 ng/ml). (Right) AUC. ****P* < 0.001. (**C**) (Left) Representative cytosolic Ca^{2+} response upon high-dose EGF in control and RTN3 KD cells, treated or not with xestospongin C (Xesto) and loaded with Fura-2–acetoxymethyl ester (Fura-2, AM). Ratio of fluorescence at 340/380 nm is reported. (Right) AUC. *P* values were calculated by one-way ANOVA. ****P* < 0.001. (**D**) Mean frequency of proximity between ER and CD147-positive structures upon high-dose EGF for 5 min. *n*, number of CD147-positive structures analyzed. Percentage ± SEM is reported. Here and in (E), (G), and (H), *P* values were calculated by two-tailed Student's *t* test. (**E**) Quantification of gold-CD147–positive TIs after 5 min high-dose EGF. Only RuR-stained structures were counted. *N*, number of cell profiles analyzed. Data are expressed as the number of gold-positive structures per PM profiles of 100-µm length ± SEM. (**F**) CD147 (green) internalization after 8 min of Alexa555-EGF (red). Scale bars, 10 µm. Blue, DAPI. (**G**) Quantification of CD147 internalization as in Fig. 5B. Integrated fluorescence intensity ± SD. ****P* < 0.001. (**H**) Morphometric analysis of gold-labeled EGFR–positive TIs (left) and CCPs (right). Data are expressed as the ratio between the number of long or short structures (defined as in Fig. 3C, top) normalized to PM profiles of 100-µm length. *N*, number of cell profiles analyzed. **P* < 0.05. (**I**) Model for EGFR endocytosis. At high EGF, EGFR is internalized through CME and NCE. NCE is mediated by PM invaginations that require the formation of RTN3-dependent ER contact sites to progress. Once TIs are formed, contacts sites are needed for local Ca^{2+} release, which is in turn required for the fission of NCE-TI.

at a later step, in late endosomes and/or MVBs, and to be modulated by calcium signaling, albeit through a different mechanism (*26*–*28*).

In conclusion, we have uncovered a modality of internalization that probably integrates numerous cellular functions toward its execution. NCE has a major role in the regulation of EGFR fate by determining its long-term attenuation. Possible alterations of NCE players can be envisioned to occur in pathological conditions involving aberrant EGFR signaling—first and foremost, cancer.

REFERENCES AND NOTES

1. T. Kirchhausen, D. Owen, S. C. Harrison, *Cold Spring Harb. Perspect. Biol.* **6**, a016725 (2014).
2. L. Johannes, R. G. Parton, P. Bassereau, S. Mayor, *Nat. Rev. Mol. Cell Biol.* **16**, 311–321 (2015).
3. E. Boucrot *et al.*, *Nature* **517**, 460–465 (2015).
4. S. Sigismund *et al.*, *Proc. Natl. Acad. Sci. U.S.A.* **102**, 2760–2765 (2005).
5. K. A. Lund, L. K. Opresko, C. Starbuck, B. J. Walsh, H. S. Wiley, *J. Biol. Chem.* **265**, 15713–15723 (1990).
6. J. D. Orth, E. W. Krueger, S. G. Weller, M. A. McNiven, *Cancer Res.* **66**, 3603–3610 (2006).
7. S. Sigismund *et al.*, *Dev. Cell* **15**, 209–219 (2008).
8. S. Sigismund *et al.*, *EMBO J.* **32**, 2140–2157 (2013).
9. G. Pines, W. J. Köstler, Y. Yarden, *FEBS Lett.* **584**, 2699–2706 (2010).
10. S. E. Ong *et al.*, *Mol. Cell. Proteomics* **1**, 376–386 (2002).

11. G. K. Voeltz, W. A. Prinz, Y. Shibata, J. M. Rist, T. A. Rapoport, *Cell* **124**, 573–586 (2006).
12. Y. Shibata *et al.*, *J. Biol. Chem.* **283**, 18892–18904 (2008).
13. M. Kirkham *et al.*, *J. Cell Biol.* **168**, 465–476 (2005).
14. S. Sabharanjak, P. Sharma, R. G. Parton, S. Mayor, *Dev. Cell* **2**, 411–423 (2002).
15. R. Lundmark *et al.*, *Curr. Biol.* **18**, 1802–1808 (2008).
16. S. M. Ferguson *et al.*, *Dev. Cell* **17**, 811–822 (2009).
17. F. Giordano *et al.*, *Cell* **153**, 1494–1509 (2013).
18. S. Carrasco, T. Meyer, *Annu. Rev. Biochem.* **80**, 973–1000 (2011).
19. T. Schikorski, S. M. Young Jr., Y. Hu, *J. Neurosci. Methods* **165**, 210–215 (2007).
20. L. Jozsef *et al.*, *J. Biol. Chem.* **289**, 9380–9395 (2014).
21. Q. Shi *et al.*, *J. Neurosci.* **34**, 13954–13962 (2014).
22. C. A. Eyster *et al.*, *Traffic* **10**, 590–599 (2009).
23. M. J. Phillips, G. K. Voeltz, *Nat. Rev. Mol. Cell Biol.* **17**, 69–82 (2016).
24. R. Marsault, M. Murgia, T. Pozzan, R. Rizzuto, *EMBO J.* **16**, 1575–1581 (1997).
25. D. L. Bennett *et al.*, *J. Biol. Chem.* **271**, 6356–6362 (1996).
26. E. R. Eden, I. J. White, A. Tsapara, C. E. Futter, *Nat. Cell Biol.* **12**, 267–272 (2010).
27. F. G. Haj, P. J. Verveer, A. Squire, B. G. Neel, P. I. Bastiaens, *Science* **295**, 1708–1711 (2002).
28. B. S. Kilpatrick *et al.*, *Cell Reports* **18**, 1636–1645 (2017).
29. P. Sengupta *et al.*, *Nat. Methods* **8**, 969–975 (2011).

ACKNOWLEDGMENTS

We thank P. De Camilli for suggestions and reagents (cDNA of HRP-KDEL and E-Syt1-GFP), G. Scita for suggestions, T. Kirchhausen for TfR cDNA, N. Borgese for cerulean-17, M. Tagaya for initially providing an anti-RTN3 antibody, R. Lundmark for anti-GRAF1 antibody, D. Cairns for initial statistical analysis of SILAC, the imaging facility at IFOM, and the ALEMBIC facility at San Raffaele Institute. We thank R. Gunby and W. Maruwge for critically reading the manuscript. This work was supported by grants from the Associazione Italiana per la Ricerca sul Cancro to T.B. (IG15741), P.P. (IG 1442), S.P. (IG 15637) and P.P.D.F. (IG 10349 and 14404 and MCO 10.000); the Italian Ministry of University and Scientific Research (MIUR), the Italian Ministry of Health, and the Monzino Foundation to P.P.D.F.; and Worldwide Cancer Research to S.S. (16-1245). A.Co. is supported by a fellowship from the Fondazione Italiana Ricerca sul Cancro. P.P.D.F. is on the Scientific Advisory Board of the Microsoft Research—University of Trento Centre for Computational and Systems Biology (COSBI) (Rovereto, Italy). The authors declare no competing financial interests. All data described in the paper are available in the main text and supplementary materials.

SUPPLEMENTARY MATERIALS

www.sciencemag.org/content/356/6338/617/suppl/DC1
Materials and Methods
Figs. S1 to S10
Tables S1 to S4
Movie S1
References (*30*–*60*)

21 July 2016; resubmitted 21 February 2017
Accepted 24 March 2017
10.1126/science.aah6152

Editor's Summary

ER-PM contacts in nonclathrin endocytosis

The epidermal growth factor receptor (EGFR) is internalized through both clathrin-mediated endocytosis and nonclathrin endocytosis (NCE). The two pathways act in concert to sustain EGFR signaling or its long-term attenuation. The mechanistic underpinnings of EGFR-NCE are unclear. Caldieri *et al*. used a variety of cell and molecular biology approaches to identify nine regulators of EGFR-NCE (see the Perspective by Tan and Anderson). They also identified an additional cargo of the pathway (CD147). One of the regulators of the pathway was the endoplasmic reticulum (ER)-resident protein reticulon 3 (RTN3). Unexpectedly, EGFR-NCE required the formation of specific contacts between the plasma membrane (PM) and the cortical ER, mediated by RTN3. ER-PM contact sites were required in the very early steps of the internalization process for the maturation of NCE tubular intermediates.

Science, this issue p. 617; see also p. 584

www.sciencemag.org/content/356/6338/617/suppl/DC1

Supplementary Materials for

Reticulon 3–dependent ER-PM contact sites control EGFR nonclathrin endocytosis

Giusi Caldieri,* Elisa Barbieri,* Gilda Nappo,* Andrea Raimondi,* Massimo Bonora, Alexia Conte, Lisette G.G.C. Verhoef,* Stefano Confalonieri, Maria Grazia Malabarba, Fabrizio Bianchi,† Alessandro Cuomo, Tiziana Bonaldi, Emanuele Martini, Davide Mazza, Paolo Pinton, Carlo Tacchetti, Simona Polo, Pier Paolo Di Fiore,†‡ Sara Sigismund†‡

*These authors contributed equally to this work.
†These authors contributed equally to this work.

‡Corresponding author. Email: sara.sigismund@ifom.eu (S.S.); pierpaolo.difiore@ifom.eu (P.P.D.F.)

Published 12 May 2017, *Science* **356**, 617 (2017)
DOI: 10.1126/science.aah6152

This PDF file includes

Other Supplementary Material for this manuscript includes the following:
(available at www.sciencemag.org/content/356/6338/617/suppl/DC1)

Materials and Methods

EGF concentrations, reagents and antibodies

Throughout the manuscript, low and high EGF means 1 and 30 ng/ml, respectively, unless otherwise indicated. Alexa-labeled EGF was used at a concentration (400 ng/ml of the conjugated specie) corresponding to an actual EGF concentration of ~40 ng/ml.

EGF was from PeproTech; Alexa-EGF and Alexa-Tf were from Molecular Probes; ^{125}I-EGF and ^{125}I-Tf from PerkinElmer. Protein-A Gold 10 nm was from Utrecht University; EM grade glutaraldehyde and paraformaldehyde employed for EM were from Electron Microscopy Sciences; ruthenium red and secondary rabbit anti-mouse were from Sigma. Fluorescent secondary antibodies were from Molecular Probes. Cage 550 secondary antibody for Super-resolution microscopy was from Aberrior. Primary antibodies were: rabbit polyclonal anti-EGFR (in-house), directed against amino acids 1172-1186 of human EGFR, used in IB; mouse anti-human EGFR (m108), directed against the extracellular domain, used in the PM-immunodepletion step of NCE vesicle purification (*30*); mouse anti-EGFR 13A9 (Genentech) used to follow endocytosis in vivo in IF and EM analyses; mouse anti-CD147 (BD); rabbit anti-RTN3 (in-house), directed against amino acids 1-47, common to all isoforms; mouse anti-pY1068 EGFR; anti-NaK-ATPase and anti-MTCO1 (Abcam); anti-dynamin-1, anti-dynamin-2, anti-EEA1, anti-eps15, anti-caveolin-1, anti-lamin B, anti-Cbl, anti-galectin 3 and anti-endophilin II (Santa Cruz); anti-TfR (Zymed); anti-AP2μ and anti-clathrin heavy chain used for WB (BD); anti-HA (BABCO); anti-tubulin (Sigma); anti-clathrin heavy chain used for IF (ABR); anti-Alexa Fluor 488 (Thermofisher). Fura-2 AM was from ThermoFisher. Ionomycin, calcium chloride, Pluronic F-68, sulfinpyrazone were from Sigma. Xestospongin C was from Abcam.

Constructs

Human RTN3A cDNA (NM_006054) was purchased from Origene (pCMV6-AC-GFP vector) and cloned by PCR in the pECFP-N1 vector (Clontech) or in the pBABE-puro vector (*4*) fused to HA-tag. For rescue experiments, we generated a cDNA of RTN3A resistant to RNAi oligo RTN3-2 by introducing 8 silent mutations by site-directed mutagenesis (oligo seq: GTTGATCATCCGCTTGTT) into the pBABE-HA-RTN3A construct. HeLa cells were infected with pBABE-HA-RTN3A RNAi resistant form, and a clone expressing the transgene at endogenous levels was selected and used in reconstitution experiments.

Human EGFR was subcloned from pBABE-EGFR (*4, 8*) in pEYFP-N1 vector (Clontech). TfR cDNA was a kind gift from Kirchhausen's Lab (Harvard Medical School) and was cloned by PCR in pEYFP-C1 vector (Clontech). E-Syt1-GFP was a kind gift from Pietro De Camilli (Yale School of Medicine). Cerulean-17 (Cer-17) was a kind gift from Nica Borgese (CNR, Milan). Cerulean empty vector was a gift from Dave Piston (Addgene plasmid #15214). RTN4a-GFP was a kind gift from Gia Voeltz (Addgene plasmid #61807), pAc-GFPC1-Sec61β was a gift from Tom Rapoport (Addgene plasmid #15108), STIM1-CFP was a gift from Anjana Rao (Addgene plasmid #19755). RTN4a, STIM1 and E-Syt1 were subcloned by PCR in pECFP-N1 vector (Clontech). Sec61β was subcloned by PCR in pCDNA3-ECFP vector (Addgene),

generating ECFP-Sec61β. All clones were sequence-verified; details are available upon request.

HeLa inducible clathrin KD clone

A silencing oligo for the clathrin heavy chain (shRNA-clat): 5'-AGCGACGCCTTGCAGAGTTAGAAGAATAGTGAAGCCACAGATGTATTCTT CTAACTCTGCAAGGCGG-3' was cloned in the pEN_TmiR vector and recombined in the pSLIKneo lentiviral vector (*31*), using the Gateway System (Invitrogen). HeLa cells were then infected with the pSLIKneo-shRNA-clat vector and selected in a medium containing 400 μg/ml neomycin for seven days. Several clonal populations were isolated. The HeLa-clone, used in the study, represents the clone for which the best silencing of clathrin heavy chain was observed upon doxycycline treatment (0.5 μg/ml doxycycline for six days, Fig. 1A-C).

Unless otherwise indicated, experiments were performed in the HeLa-clone. When we used the nomenclature "control" we mean HeLa-clone in the absence of doxycycline, when we used the nomenclature "clathrin KD' we mean HeLa-clone treated with doxycycline (see Fig. 1A-C).

Cell culture and transfection

HeLa and BT20 cells were cultured in GlutaMAX™-Minimum Essential Medium (MEM, Gibco Invitrogen), supplemented with 10% FBS, sodium pyruvate 1 mM (Euroclone), 0.1 mM non-essential amino acids (Euroclone). HeLa cells at 50 – 60% confluence were transfected using FuGene (Roche Diagnostics, Indianapolis, IN) according to Manufacturer's instruction. Experiments were performed 24 h after transfection. A431 and HaCaT cells were cultured in DMEM medium (Lonza), supplemented with 10% FBS and 2mM glutamine.

All human cell lines were authenticated at each batch freezing by STR profiling (StemElite ID System, Promega). All cell lines were tested for mycoplasma at each batch freezing by PCR (*32*) and biochemical assay (MycoAlert, Lonza).

The inducible clathrin KD HeLa clone was grown in the same medium of HeLa cells, but supplemented with 10% TET-System Approved FBS (PAA) instead of standard FBS. For SILAC experiments, cells were grown in DMEM medium without Arg and Lys (PAA), supplemented with 10% fetal bovine dialyzed serum (Gibco Invitrogen), sodium pyruvate 1 mM (Euroclone), non-essential amino acids (Euroclone), and 2 mM glutamine. The medium was supplemented with either 21 mg/l of unlabeled Arg and 48 mg/l of unlabeled Lys ("light" medium) or with 21 mg/l of Arg10 and 48 mg/l of Lys8 ("heavy" medium). Cells were grown in heavy and light media for at least 5 passages to allow the incorporation of the heavy and light isotopes and then induced with 0.5 μg/ml of Doxycycline (Dox) for six days.

EGFR-containing NCE vesicle purification

Biochemical fractionation

'Light' and 'heavy' inducible clathrin KD cells were plated in 15-cm dishes at the same concentration (2.5 x 106 cells/plate, 13 plates/each). Cells were then serum starved for 16 h and either stimulated with 100 ng/ml EGF for 1 h at 4°C (pre-binding) and shifted for 8 min at 37°C (12 plates, heavy), or left unstimulated for 1 h at 4°C (12 plates,

light). At the time of collection, cells were put on ice, washed twice with cold PBS and scraped in 3 ml of cold PBS. The thirteenth plate (1 heavy and 1 light) was used to count the number of cells/plate. Light- and heavy-labeled cells were mixed in 1:1 ratio. Cells were washed once with PBS and resuspended in 5.5 ml of homogenization buffer [(25 mM Hepes, 25 mM KCl, 2.5 mM $Mg(OAc)_2$, 0.25 M Sucrose, (*33*)]. Cells were left on ice for 30 min in the presence of 50 µg/ml RNAse A and then mechanically homogenized with 2 cycles of 2 min with a manual potter (Potter-Elvehjem style tissue grinder with PTFE pestle) and syringed through a 21G needle (10 passes). The resulting homogenate was diluted with 18 ml of homogenization buffer and centrifuged for 10 min at 800g to obtain a post-nuclear supernatant (PNS), devoid of nuclei, large patches of membranes and cytoskeleton. The PNS was further centrifuged at 12,000g to remove PM and large organelles, such as the Golgi, mitochondria and lysosomes. The resulting supernatant (S2) was used as a source of vesicles for the subsequent steps. An aliquot of each fraction was collected and analyzed by WB.

Crosslinking of magnetic beads

Pan mouse Dynabeads (Invitrogen) were washed once with sodium phosphate 0.1 M pH 8.2 and then resuspended in sodium phosphate 0.1 M pH 8.2 plus the primary antibody (mAb108 or pY1068-EGFR; 1µg/100µl beads) to coat them with the antibody. The reaction was allowed to proceed for 16 h at 4°C under rotation. The magnetic beads were then washed twice with sodium phosphate pH 8.2 and twice with triethanolamine 0.2 M (TEA) pH 8.2 and finally resuspended in TEA. To crosslink the primary antibody to the magnetic beads, we used DMP (ThermoScientific). A solution of DMP 2X (20 mM in TEA) was prepared and added to the beads to reach the final concentration of 10 mM DMP. Beads were incubated at room temperature for 30 min under rotation. Then, the DMP was removed and the reaction was quenched with Tris-HCl 50 mM pH 7.5 for 15 min at room temperature under rotation. Beads were washed once with PBS, and then three times with glycine 0.1 M pH 2.7 (5 min each wash). Cross-linked beads were briefly washed in sodium phosphate 0.1 M pH 8.2, resuspended in sodium phosphate 0.1 M pH 7 and stored at 4°C (up to a few days) before use.

Immunodepletion and immunopurification

Anti-EGFR m108-crosslinked beads were incubated with the S2 fraction in the presence of 0.01 mg/ml BSA (50-70 µl beads per ml of S2) for 1 h at 4°C, under rotation. Three cycles of depletion were performed; in a number of standardization experiments, we observed that at least three cycles were needed to deplete the S2 fraction of all EGFR whose extracellular domain was accessible to the m108 Ab (unpublished data). The supernatant, after the depletion, was subjected to one cycle of immunopurification with pY1068-coated beads in order to obtain phosphoEGFR-containing vesicles (one cycle was sufficient to IP all the pY-1068 EGFR present the in S2 fraction, see Fig. S1E). As control, incubation with magnetic beads coated only with anti-mouse secondary antibody (Pan mouse Dynabeads without primary antibody) was performed. Beads were then washed 3 times with homogenization buffer containing 0.01 mg/ml BSA, and 3 times with the same buffer without BSA. Proteins were eluted in SDS sample buffer (62.5 mM Tris-HCl pH 6.8, 2% SDS, 1% glycerol), 100 µl per ml of beads, at 95°C for 5 min.

SDS-PAGE analysis, in-gel digestion, and LCMSMS analysis

Immunopurified EGFR-containing vesicles eluted in SDS sample buffer were acetone precipitated. Protein pellets were resuspended in 30 µl of Laemmli buffer (62.5 mM Tris-HCl pH 6.8, 2% SDS, 10% glycerol, 0.1% bromophenol blue, 5% v/v β-mercaptoethanol). Samples were run on NuPAGE® Novex 4-12% gradient SDS-PAGE gels. The gel was fixed in 50% methanol + 10% acetic acid and stained overnight with blue Coomassie. Bands were excised and trypsin digested according to the standard protocol: reduction in 10 mM DTT for 1 h at 56ºC, alkylation with 55 mM iodoacetamide for 45 min at room temperature in the dark and digestion with 12.5 ng/µl trypsin overnight at 37ºC. Peptides were extracted with 3% trifluoroacetic acid and 30% acetonitrile, spun onto STAGE Tips (*34*), and eluted in 20 µl buffer B (80% acetonitrile, 0.5% acetic acid). The acetonitrile was evaporated using a speed vac (Concentrator 5301, Eppendorf AG, Hamburg Germany) and the volume of the eluates was adjusted to 5 µl with 2% trifluoroacetic acid of which 2.5 µl were injected for LC-MS/MS analysis. The analytical platform was composed of a LTQ-FT mass spectrometer (ThermoElectron, Bremen, Germany) and an Agilent 1100 binary nanopump (Palo Alto, CA). C18 material (ReproSil-Pur C18-AQ 3 µm; Dr. Maisch GmbH, Ammerbuch-Entringen, Germany) was packed into a spray emitter (75 µm ID, 8 µm opening, 70 mm length; New Objectives, USA) using an air pressure pump (Proxeon Biosystems, Odense, Denmark) to prepare an analytical column with a self-assembled particle frit. Mobile phase A consisted of water, 5% acetonitrile and 0.5% acetic acid, and mobile phase B of acetonitrile and 0.5% acetic acid. The samples were loaded from an Agilent 1100 autosampler onto the column at 500 nl/min flow rate. Slices were analyzed on 120 min gradients. The 120 min gradients with a 250 nl/min flow rate went for buffer B from 2% to 40% in 100 min and then to 80% in 20 min. An additional 10 min were used in each run for equilibration, loading and washing. The mass acquisition method used was one FT-MS followed by 5 subsequent MS2 events in the ion trap. The spectrometer acquired a Full MS at resolution 100,000 at 400 m/z in the FT-ICR cell.

Protein identification and quantification

MaxQuant, version 1.1.1.36, produced peak lists from the MS/MS spectra that were subjected to database search (*35*), and quantitation of SILAC pairs and filtering. The software was supported by Mascot as the database search engine for peptide identifications (Version 2.2, Matrix Science) (*36*). MS/MS spectra were searched against the human International Protein Index (IPI) database (versions 3.38). False discovery rates (FDRs) were controlled by searching in a concatenated database consisting of the original protein sequences plus their reversed versions, where all K and R were exchanged with each other. Protein sequences of common contaminants, e.g. human keratins and proteases used, were added to the database. False positive rates for peptides were calculated as described in (*37, 38*). Peptides and proteins with an FDR of <1%, estimated based on the number of accepted reverse hits, were accepted. The initial mass tolerance in MS mode was set to 7 ppm and MS/MS mass tolerance was 0.5 Da. For the Mascot search, cysteine carbamidomethylation was searched as a fixed modification, whereas N-acetyl (Protein), Oxidation (M) and GlyGly (K) were searched as variable modifications. Labeled arginine ($^{13}C_6$, $^{15}N_4$) and lysine ($^{13}C_6$, $^{15}N_2$) were specified as fixed or variable modifications, depending on the prior knowledge about the parent ion

for the Mascot searches. Full tryptic specificity with up to 2 missed cleavages was required and only peptides of at least 6 amino acids were considered. By default, it was required that each protein group was identified with at least one peptide that was unique to the group. SILAC peptide and protein quantification were performed automatically with MaxQuant taking into account all isotope patterns and all scans of the heavy and light versions of the peptides eluted in. The accuracy of a protein ratio was assessed by calculating the coefficient of variability over all redundant quantifiable peptides. Ratios for proteins were determined as the median over all measured peptide ratios for a given protein, minimizing the effect of outliers. Furthermore, MaxQuant calculates a normalized version of the protein ratios that corrects for unequal protein amount. Outputs from MQ were manually filtered as follows: proteins identified were accepted only if they contained two peptides, at least one of them unique (peptide>1, unique>0). Proteins quantified were considered for further analysis only if they had ratio count (lower number of quantified SILAC pairs) > 2 (File S1). Protein normalized ratios were transformed in log2 and plotted as a histogram by Perseus software (http://141.61.102.17/perseus_doku/doku.php?id=start). The calculated histogram fits with a bimodal distribution and upregulated protein ratios were defined within the top 20% of total protein ratio distributions.

RNA interference

Silencing was performed by transient transfection of siRNA oligos using Lipofectamine RNAiMAX (Invitrogen), following the manufacturer's instructions. Cells were subjected to a double transfection cycle (on day 1 in suspension, and on day 2 in adhesion). Experiments were performed 72 h after the second transfection later. For dynamin 1/2 KD (referred as dyn KD throughout the manuscript) a single transfection in suspension was performed, the experiment was performed 48 h later.

For the RNAi screening of the 101 candidates, we employed a pool of four RNAi oligos for each gene (ON-TARGET plus, Dharmacon Smart Pool library). We also performed deconvolution of the four oligos in the pool (File S2, spread-sheet 9), in the described cases. Oligo sequences and experimental details are available upon request. As negative controls, we used the All Stars oligo from Qiagen (#1027281) and/or mock treated cells.

Other silencing oligo sequences were:

clathrin heavy chain (Riboxx): 5'-UAAAUUUCCGGGCAAAGAGCCCCC-3'
dynamin 1 (Riboxx): 5'-UUUCACAAUGGUCUCAAAGCCCCC-3'
dynamin 2 (Riboxx): 5'-UGAACUGCAGGAUCAUGUCCCCC-3'

For the RTN3 KD, in the initial RNAi screening, we used the Dharmacon Smart Pool of four oligos. Results were confirmed with three different oligos from Invitrogen (Stealth). All three oligos had a comparable effect on EGF internalization, without altering EGFR levels. RTN3-1 and RTN3-2 target all RTN3 isoforms, while RTN3-3 targets all except isoform G. We selected oligo RTN3-2 because it gave the most efficient KD (>90%) for all the subsequent experiments. With this oligo we have performed rescue experiments (Fig. 5C and Fig. S8C). The sequences of the RTN3-silencing oligos were:

RTN3-1: 5'-UCAGUGUCAUCAGUGUGGUUUCUUA-3'
RTN3-2: 5'-CCCUGAAACUCAUUAUUCGUCUCUU-3'
RTN3-3: 5'-GGUAGAAGAUCUGGUUGACUCCUUG-3'

Also for REEP5, we confirmed the results obtained with the Dharmacon Smart Pool library using three separate oligos from Invitrogen (Stealth):

REEP5-1: 5'-GAAUGGAGAUUGGCCUGGUUGUUUC-3'

REEP5-2: 5'-CAGGAUAGCUUUAUAAAGCAGUUAG-3'

REEP5-3: 5'-CAGCCUACAUCUCAAUUAAAGCUAU-3'

Given the variability of REEP5 KD level, we validated some of the critical data with an additional oligo from Riboxx that gave a better KD level.

REEP5-4: 5'-UUAAUUGAGAUGUAGGCUGCCCCC-3'

For RTN4 KD, we used two silencing oligos targeting all described isoforms (Stealth, Invitrogen):

RTN4-1: 5'-CCAGCCUAUUCCUGCUGCUUUCAUU-3'

RTN4-2: 5'-CCUAUUCCUGCUGCUUUCAUUGACA-3'

For Endophilin A1 and A2 KD, we used a single silencing oligo and a pool of four oligos (Riboxx), respectively:

Endophilin A1: 5'-AUUAUUUCCAUCACAGCCCCC-3'

Endophilin A2-pool: 5'-UUUGAAGUCAUCAUCCAGCCCCC-3'
5'-UCUUCUUGUAGUCAAAGUCCCCC-3'
5'-ACUGGAACCUUUGUGCUUGCCCCC-3'
5'-UCGAUCCCAUCCUGUUAAGCCCCC-3'

For E-Syt1, E-Syt2, E-Syt3 and STIM1 KD we used a pool of four oligos (Riboxx), respectively:

E-Syt1-pool: 5'-UAAUGUAAGAUCCAGUGGCCCCC-3'
5'-UCAAACUAUUCACCUGCAGCCCCC-3'
5'-AGACAACUAAGAUGGCAGCCCCC-3'
5'-UGAAGAACAUUGACACAGCCCCC-3'

E-Syt2-pool: 5'-UUAAUUGUGUCUACUCUGCCCCC-3'
5'-UUUACAGACACACACAGCCCCC-3'
5'-AUAAAGCACAGACACAUCCCCC-3'
5'-UUUACAGUCUUAUUUAGCCCCC-3'

E-Syt3-pool: 5'-UCAAACACUUCGUUCCAGGCCCCC-3'
5'-UGGAUAAUUUAGUAGGCACCCCC-3'
5'-UUCUUUACUUCUUCUUCCAUGGCCCCC-3'
5'-ACGAAUUUCACCAUGCAUCCCCC-3'

STIM1-pool: 5'- GGGGGCUAAGGAAGAUGGUAUA-3'
5'- GGGGGCUGGUGGUGUCUAUCGUUA-3'
5'- GGGGGAGCACAUGAAGAAGAUGA-3'
5'- GGGGGUCAUCAGAAGUAUACAAU-3'

Quantitative real-time PCR analysis

Total RNA was extracted from HeLa cells (control and KDs, as indicated) using the RNeasy kit from Qiagen, according to the manufacturer's protocol. Single stranded cDNA synthesis was performed using the QuantiTect Reverse Transcription Kit (Qiagen) following manufacturer's instructions.

For the analysis of RTN3 isoform expression in HeLa cells, the QuantiFast SYBR Green PCR Kit (Qiagen) was used, according to manufacturer's instructions. Light cycler 480 instrument for qPCR was from Roche.

Below is the sequence of the oligos used:

RTN3(A+D+G)-for	5'-CTGTGCGGTGCACGATCT-3'
RTN3(A+D+G)-rev	5'-ACAGCTTGGATGACGGACTT-3'
RTN3B-for	5'-CTGTGCGGAGGGATTGAG-3'
RTN3B-rev	5'-GCTCCCTAACACATGGCTTT-3'
RTN3C-for	5'-ACCTCACAAGTGCACGATCT-3'
RTN3C-rev	5'-TGACAGAGAGAAGAGCCAGGA-3'
RTN3D-for	5'-TGAGAAGTACAAGGATCCAAGC-3'
RTN3D-rev	5'-AATGGTGTTTTAGTAACTGTTGCATT-3'
RTN3E-for	5'-CCTCACAAGAGGGATTGAGC-3'
RTN3E-rev	5'-TAGGCTGGCTCCCTAACACA-3'
RTN3F-for	5'-CTGTGCGGCCAGTTTCCC-3'
RTN3F-rev	5'-CTCAGTAGGTGGTTTCTGGGCTG-3'
RTN3G-for	5'-CCATTCAAACCCAGATTGATC-3'
RTN3E-rev*	5'-AATGGTGTTTTAGTAACTGTTGCATT-3'
(*same as RTN3D-rev)	
RTN3all(-G)-for	5'-ACAGCCAGCTTCAAGGAGTC-3'
RTN3all(-G)-rev	5'-TGGAAAGCTTCTGAGGACAG-3'

For the analysis of KD levels by RT-qPCR, the Taqman chemistry (Thermo Fisher Scientific) was used. qPCR instrument was from Applied Biosystems. For the different genes, inventoried Taqman assays (Applied Biosystems) were employed.

Cell lysis and immunoblot (IB)

Cell lysis was performed to control KD levels and to follow EGFR degradation by IB, cells were lysed in RIPA buffer (50 mM Tris–HCl, 150 mM NaCl, 1 mM EDTA, 1% Triton X-100, 1% sodium deoxycholate, 0.1% SDS), plus protease inhibitor cocktail (CALBIOCHEM) and phosphatase inhibitors (20 mM sodium pyrophosphate pH 7.5, 50 mM NaF, 2 mM PMSF, 10 mM Na_3VO_4 pH 7.5).

For EGFR degradation, HeLa cells were plated on five 10-cm dishes at 50% confluence. The day after, cells were serum starved for 16 h and then stimulated at the indicated time points with 100 ng/ml EGF. For anti-EGFR IB, 10 µg of total cell lysate was loaded onto an 8% SDS polyacrylamide gel; IB was performed as described (*39*).

^{125}I-EGF and ^{125}I-Tf -based assays

Internalization of ^{125}I-EGF and ^{125}I-Tf was performed at low EGF (1 ng/ml), high EGF (30 ng/ml) or Tf (1 µg/ml). All these experiments were performed at 37 °C without temperature shift.

In detail, HeLa cells were plated in 24-well plates (100,000/well) in at least duplicate for each time point, plus one well to assess non-specific binding. The day after, cells were serum-starved for at least 2 h in binding buffer (serum-free medium supplemented with 0.1% BSA, 20 mM Hepes) and then incubated at 37°C in the presence of 1 ng/ml ^{125}I-EGF, or 30 ng/ml EGF (1 ng/ml ^{125}I-EGF + 29 ng/ml cold EGF) or 1 µg/ml of ^{125}I-Tf, in 300 µl of binding buffer. At different time points (2, 4, 6 min), cells were put on ice, washed twice in cold PBS, and then incubated for 5 min at 4°C in 300 µl of acid wash solution pH 2.5 (0.2 M acetic acid, 0.5 M NaCl). The radioactivity recovered in the acid wash represents the amount of ^{125}I-EGF or ^{125}I-Tf bound to the receptor on the cell surface. Cells were then lysed with 300 µl of 1N NaOH, which represents the amount of internalized ^{125}I-EGF or ^{125}I-Tf. Non-specific binding was measured at each time point in the presence of an excess of non-radioactive EGF (300 times) or Tf (500 times). After being corrected for non-specific binding, data were plotted as the ratio between internalized and surface-bound radioactivity over time. Endocytic rate constants [Ke and Ke obs, (*8*)] were calculated from the slope of the trend-line. Results are expressed as the internalization rate constant (Ke or Ke obs) or as a % of Ke in control cells, as indicated, and are the mean ±SD, calculated on duplicate points of at least two independent experiments. Statistical analysis was performed using Each Pair Student's t test with JMP 10.0 statistical software (SAS Institute, Inc) or Two-tailed Student's t test with Excel, as indicated.

Note that, in case of ^{125}I-EGF internalization, ~20-25% of the internalization events are insensitive to dynamin1/2 KD both at low and high EGF doses. This is operationally defined as background, but might be due to the existence of third internalization pathway that is dynamin-independent and kinase-independent (EGFR constitutive pathway) (*8*).

Surface EGFRs were measured by ^{125}I-EGF saturation binding as described (*8*). Degradation of ^{125}I-EGF was measured as described previously (*7*). Standard deviations and P-values (Each Pair Student's t test with JMP 10) were calculated on triplicate points of two independent experiments.

IF-based EGF internalization assays and colocalization analysis

HeLa cells, plated on glass coverslips, were incubated at 37°C for the indicated times with high dose Alexa-conjugated EGF (see section "EGF concentrations"). Samples were then fixed in 4% paraformaldehyde. When indicated, acid wash treatment was performed before fixation, by incubating cells for 10 min at 4°C in an acidic buffer (acetic acid 0.2 M, NaCl 0.5 M) pH 2.5, followed by washes with Hepes-supplemented medium to restore pH before fixation. Cells were then permeabilized with 0.1% TritonX-100 in PBS supplemented with 1% (w/v) BSA, and labeled with primary antibodies against the protein of interest in PBS/BSA, followed by visualization by incubation with specific secondary antibodies. Images were obtained using a Leica TCS SP2 or TCS SP2 AOBS confocal microscope equipped with a 63X oil objective and processed using ImageJ.

To quantify internalized EGF (Table S2), HeLa cells were stimulated with high dose Alexa-conjugated EGF (see section "EGF concentration") at 37 °C. Before fixation samples were subjected to acid wash treatment in order to visualize only internalized ligand. Images were analyzed using ImageJ. EGF signal was highlighted applying an

intensity based threshold (Default method), and then fluorescence intensity per field was calculated using the "Measure" command, limiting measurement to threshold. This value was then divided for the number of nuclei in the field, counted using the DAPI signal, in order to calculate the EGF fluorescence intensity per cell.

In vivo internalization assays of EGFR or CD147 using antibodies

For antibody internalization assays, serum-starved cells were incubated with anti-EGFR 13A9 or CD147 antibody for 30 min at 4 °C or for 5 min at 37 °C (to avoid temperature shift), with comparable results. Cells were then stimulated with high dose Alexa-conjugated EGF (see above, section "EGF concentration") at 37 °C for the indicated times. As control, we also incubated CD147 in the absence of EGF and we observed no detectable CD147 internalization within 30 min of incubation. After internalization, cells were either not treated or acid wash-treated (see section "IF-based EGF internalization assays and colocalization analysis") as indicated. Cells were then fixed and processed for IF. For CD147 internalization assays (*22*), non-permeabilized cells were incubated with an excess of Alexa-647 secondary antibody in PBS/BSA 1% (to saturate PM-localized CD147 antibody), followed by permeabilization and incubation with an Alexa-488 secondary antibody to label the internalized CD147 antibody (note that also residual PM-localized CD147, not-saturated by the Alexa-647 secondary antibody, is stained, see Fig. 7B).

Quantitative imaging analysis of CD147 internalization

To quantify internalized CD147 (Fig. 5B, C, Fig. 6G and Table S2), HeLa cells were incubated in vivo with anti-CD147 antibody (as described in "In vivo internalization assays of EGFR or CD147 using antibodies") and stimulated with high dose Alexa-conjugated EGF (see section "EGF concentration") at 37 °C. Before fixation samples were subjected to acid wash treatment (see section "IF-based EGF internalization assays and colocalization analysis") in order to visualize only internalized CD147/EGF (see Fig. 5A). Images were acquired with a Leica TCS SP2 confocal microscope equipped with a 63x oil immersion objective (Leica HCX PL APO CS, 1.4NA) using a 1024x1024 scan format and a 2,3x optical zoom (100nm pixel size). A homemade Fiji plugin (*40, 41*) was developed to calculate CD147 integrated fluorescence intensity per cell (expressed as arbitrary units). We used the Alexa555-EGF signal to identify EGFR-positive vesicles. In order to enhance the signal vs. background and identify the vesicles, the image was filtered with a Laplacian of Gaussian filter [using the FeatureJ-Laplacian plugin (*42*) with a smoothing scale parameter of 2], then histogram based threshold was applied. The threshold ($Thr_{vesicle}$) is calculated with this formula:

$$Thr_{vesicles} = I_{max} - 0.05 * (I_{max}-I_{mode})$$

with I_{max} maximum intensity and I_{mode} the mode intensity of the histogram.

Only those pixels that deviate from the maximum intensity less than 5% of the difference between the maximum intensity and the mode intensity are considered to belong to a vesicle. We then measured the CD147 integrated fluorescence intensity within the recognized vesicles for each field. This value was then divided for the number of nuclei in the field, in order to calculate the CD147 integrated fluorescence intensity per

cell. The nuclei were identified using the DAPI signal and their boundaries were outlined by applying a histogram normalization and then an intensity based threshold (Li method). Data are the mean ±SD, calculated on ~5-10 different fields of at least two independent experiments. P-values were calculated using Each Pair Student's t test with JMP 10 or Two-tailed Student's t test with Excel, as indicated.

Super-resolution microscopy

HeLa cells were labeled in vivo for EGFR as described above and stimulated with 100 ng/ml EGF for 2 min at 37°C, or left unstimulated. Additionally, HeLa cells stimulated with 1 ng/ml EGF for 2 min at 37°C were used to analyze cross-correlation in conditions where only CME is active. Samples were fixed in 4% paraformaldehyde, permeabilized and then labeled with anti-RTN3 rabbit polyclonal antibody, followed by incubation with anti-mouse Cage-550 and anti-rabbit Alexa 647 secondary antibodies.

Super-resolution localization imaging was obtained by direct stochastic optical reconstruction microscopy (dStorm) (*43*). Briefly, the fluorescent molecules are induced to blink on and off by reducing agents included in the imaging medium. If few molecules are fluorescent at each time, so that the diffraction limited spots corresponding to individual fluorophores are well separated, the position of each molecule can be quantified with higher accuracy than the resolution limit (*44*). By acquiring multiple images of the same field (tens to hundreds of thousands), and storing the position of the localized molecules at each frame it is therefore possible to obtain an image of the sample with resolution higher than the diffraction limit.

dStorm was performed on a Leica SR GSD-3D (Leica Microsystems Srl, Milan, Italy) super-resolution microscope equipped with a 150x 1.45NA objective, an Andor iXon Ultra-897 EM-CCD sensor and three solid state lasers (405 nm 100 mW, 488 nm 300 mW, and 647 nm 500 mW). The sample was mounted on the stage and the medium was substituted prior to acquisition with a mix of glucose oxidase (560 µg/ml), catalase (400 µg/ml) and cysteamine HCl (100 mM) in TN buffer with 10% glucose (w/v) pH 8.0, to induce blinking of the fluorophores (*45*). Alexa 647 and Cage 500 were imaged sequentially (starting from the red channels). 30,000 images were collected for each channel with 5 to 20 ms exposure times and an increasing ramp of 405 nm laser intensity with powers between 0 and 0.8 mW was used to reactivate the molecules in long-lived dark states. Only localization events occurring at the periphery of the cell were considered (within 2 µm from the PM). Furthermore, localization events with less than 20 photons/pixel for the Alexa 647 dye and 40 photons/pixels for the Cage 500 dye were discarded. The list of the detected molecules in the two channels was used to compute the cross-correlation of the two images as described in (*29*): the cross-correlation curve was then fit by an exponential decay to quantify the degree of colocalization between EGFR-Cage500 and RTN3-Alexa647 and the size of the co-clusters, respectively provided by the cross-correlation amplitude C_0 and the correlation length R_c. For visualization purposes, the super-resolution images were reconstructed by rendering each of the detected molecules as a Gaussian distribution, with width equal to the localization precision of each event. Note that no significant cross-correlation signal was observed between EGFR and RTN3 in serum-starved conditions, indicating negligible co-clustering of the two proteins.

FRET

Cells were acquired with a Zeiss LSM 510 confocal microscope through a Plan-Apochromat 63x/1.4 Oil objective with a pixel size 0.139 μm, time acquisition between interval was 6,5 sec. ECFP and EYFP were excited through an Argon laser at 458 and 514 nm respectively, while EGF-555 was excited with a HeNe laser at 546 nm. Emissions were selected with the following band pass filters: BP 470-500 for ECFP, BP 530-600 for FRET and EYFP, BP 560-615 for EGF-555.

Sensitized emission FRET (SE-FRET) were calculated by a custom macro written for the open source FIJI software according to (*46*). For sensitized emission calculations, single fluorescent protein images for each channel were acquired.

In Fig. 4B, SE-FRET from the whole cell was collected. Statistical analysis was performed using GraphPad Prism. Two-tailed Student's t test was used to calculate statistical significance between different samples.

In Fig. 4C, SE-FRET extent was collected only in the plasma membrane regions exposed to EGF-555 by obtaining a binary mask on the EGF-555 images. Binarized EGF-555 masks were filtered by structures smaller than 0.2 μM^2 to exclude endosomal EGF-555.

Statistical analysis was performed using GraphPad Prism. One-way ANOVA was used to calculate statistical significance between different samples.

Duolink proximity ligation assay

For proximity ligation assay, "Duolink In Situ Detection Reagents Orange" (Olink Bioscience) was employed according to manufacturer's instruction. As primary antibody, a rabbit anti-RTN3 and a mouse anti-pY1068 EGFR were used.

Electron microscopy

Pre-embedding immunolabeling. Serum-starved cells were incubated with anti-EGFR 13A9 or with anti-CD147 antibody, followed by incubation with rabbit anti-mouse, and, finally, with Protein-A Gold 10 nm (30 min incubation on ice/each step). Cells were then incubated at 37°C for 2, 5 or 8 min with 30 ng/ml EGF, as indicated. A control sample left at 37°C for 5 or 8 min without EGF was included in the experiment to control that no internalization was induced by the antibody in the absence of ligand (our unpublished results). Cells were then washed in PBS and fixed for 1 h at room temperature in 1.2% glutaraldehyde in 66 mM sodium cacodylate buffer pH 7.2 containing 0.5 mg/ml of ruthenium red. After quick washes with 150 mM sodium cacodylate buffer, the samples were post-fixed in 1.3% osmium tetroxide in a 66 mM sodium cacodylate buffer (pH 7.2) containing 0.5 mg/ml ruthenium red for 2 h at room temperature. Cells were then rinsed with 150 mM NaCacodylate, washed with distilled water and enbloc stained with 0.5% uranyl acetate in dH_20 overnight at 4°C in the dark. Finally, samples were rinsed in dH_2O, dehydrated with increasing concentrations of ethanol, embedded in Epon and cured in an oven at 60°C for 48 h.

As an independent procedure to visualize EGFR internalizing structures, clathrin-coated pits (CCPs) and tubular invaginations (TIs), we performed cryosection experiments (Fig. S3B). Briefly, cells were stimulated with Alexa-488 EGF (see paragraph "IF-based EGF internalization assays and colocalization analysis"), fixed for 1 h at room temperature (0.2% glutaraldehyde/ 2% paraformaldehyde in PHEM Buffer 0.1

M) and processed as described previously (*47*). Briefly, samples were embedded in 12% gelatin, infiltrated in 2.3 M sucrose and frozen in liquid nitrogen. Cryosections were obtained using a Leica EM FC7 ultramicrotome (Leica microsystem, Vienna, Austria) and collected on 150 mesh formvar carbon-coated copper grids. The labeling procedure was carried out using a rabbit anti-Alexa Fluor 488 antibody (5 µg/ml) in 1% BSA in PBS that was afterwards visualized with proteinA conjugated to 10 nm colloidal gold particles (Utrecht University). Grids were contrasted in a solution of uranyl acetate and methyl-cellulose, air dried and observed in a Leo 912AB transmission electron microscope (Carl Zeiss, Oberkochen, Germany).

KDEL-HRP/DAB visualization of ER. Cells were fixed in 1% glutaraldehyde in 0.1 M sodium cacodylate buffer (pH 7.4) for 30 min at room temperature, followed by incubation with 0.3 mg/ml 3,3'-diaminobenzidine tetrahydrochloride (DAB) and 0.03% hydrogen peroxide in 0.1 M sodium cacodylate buffer pH 7.4 for 20 min at room temperature. Samples were rinsed in sodium cacodylate buffer and post-fixed with 1.5% potassium ferrocyanide, 1% osmium tetroxide in 0.1M sodium cacodylate buffer (pH 7.4) for 1 h on ice. After enbloc staining with 0.5% uranyl acetate in dH_20 overnight at 4°C in the dark, samples were dehydrated with increasing concentrations of ethanol, embedded in Epon and cured in an oven at 60°C for 48 h. Ultrathin sections (70 – 90 nm) were obtained using an ultramicrotome (UC7, Leica microsystem, Vienna, Austria), collected, stained with uranyl acetate and Sato's lead solutions, and observed in a Transmission Electron Microscope (Leo 912AB, Carl Zeiss, Oberkochen, Germany). Digital micrographs were taken with a 2Kx2K bottom mounted slow-scan camera (ProScan, Lagerlechfeld, Germany) controlled by the EsivisionPro 3.2 software (Soft Imaging System, Münster, Germany).

HA-RTN3 pre-embedding immunolabeling (Fig. S3H). HeLa cells stably expressing HA-RTN3 Isoform A were fixed with 4% formaldehyde in 0.1M Phosphate buffer pH 7.4 for 1 hour at room temperature. Cells were washed in PBS and treated with 50mM glycine for 10 minutes. Subsequently, cells were permeabilized with 0.25% saponin, 0.1% BSA and blocked in blocking buffer (0.2% BSA, 5% goat serum, 50 mM NH_4Cl, 0.1% saponin, 20 mM PO_4 buffer, 150 mM NaCl) for 30 minutes. Cells were incubated sequentially with anti HA primary antibodies and Goat anti Mouse nanogold-conjugated secondary antibodies (Nanoprobes, NY, USA) diluted in blocking buffer. After washes in PBS, cells were re-fixed in 1% glutaraldehyde and nanogold was enlarged with gold enhancement solution (Nanoprobes, NY, USA) according to manufacturer instructions. Cells were post-fixed with osmium tetroxide, embedded in epon and processed into ultrathin slices. After contrasting with uranyl acetate and lead citrate, sections were analyzed with a Zeiss LEO 512 electron microscope. Images were acquired by a 2k x 2k bottom-mounted slow-scan Proscan camera controlled by the EsivisionPro 3.2 software. To visualize the ER cells transfected with HRP-KDEL were fixed with 4% formaldehyde in 0.1M Phosphate buffer pH 7.4 and incubated with 0.3 mg/ml 3,3'-diaminobenzidine tetrahydrochloride (DAB) and 0.03% hydrogen peroxide in PBS, Samples were then processed for RTN3-HA pre-embedding labeling as formerly described. For the quantification of RTN3 labeling density, gold particles present within 20 nm of plasma membrane or ER membranes profiles were counted and expressed as density (number of gold particles/μm^2).

EM Morphometry and automated ER segmentation analysis. ER-PM contact site analysis. For ER labeling, cells were transfected with HRP-KDEL (*19*); 24 hours after transfection, cells were subjected to pre-embedding immunolabeling with anti-EGFR 13A9 or anti-CD147 antibodies as described above. Cells were then fixed and processed for EM analysis. To quantify the percentage of EGFR endocytic invaginations associated with ER tubules (Fig. 4E), the PM of HRP-stained cells was scanned and when an EGFR-positive endocytic structure (clearly connected to the PM) was encountered (CCP or TI), EM micrographs of this region and of the same area on the previous and next serial sections were acquired. The three serial sections images were aligned in IMOD (3dmod Ver 4.7.9) and imported in ImageJ, where selection lines at ≤ 20 nm from the membrane of the endocytic structure were overlaid on the three images. An endocytic structure was considered associated with an ER tubule if at least in one section an ER tubule was present inside the delimited area (see Fig. S5D for a graphical reference).

To quantify the proximity of ER and CD147 (Fig. 5F), since more gold-CD147 decorates NCE tubules compared to gold-EGFR (thus facilitating the recognition of CD147-positive internalizing structures), we avoided the use of serial sectioning; instead, random images of CD147 positive structure were acquired at a nominal magnification of 10K. CD147 positive structures were considered associated or in proximity when at least an ER tubule was present at ≤ 20 nm.

EGFR and CD147 internalization. For the quantification of the percentage of internalized gold-labeled EGFR or CD147 (Fig. 3D, Fig. S3D and Fig. S9C), several cellular profiles were randomly selected, and the number of gold particles present in PM-connected (ruthenium red-positive) or internalized (ruthenium red-negative) structures was quantified and expressed as the percentage of the total number of gold particles counted for the entire cellular profile.

For the quantification of the number of CCPs or TIs upon different KDs (Fig. 3B and Fig. 5D), gold particle clusters present on the PM of randomly selected cells were acquired at a nominal microscope magnification of 8000x (pixel size 1.4 nm). Gold clusters were assign to one of the two categories and the distance between PM and the tip of the invagination was measured using ImageJ. The number of ruthenium red-positive endocytic structures identified was divided by the PM length measured with ImageJ on acquired low magnification micrographs (nominal microscope magnification of 1840x). Not that structures that cannot be unequivocally ascribed to one or the other category were excluded from the analysis (~ 2-3% of cases maximum).

CD147 time course internalization analysis (Fig. 5E). Cells labeled with anti-CD147 antibodies were stimulated with EGF and fixed with 1.2% glutaraldehyde in 66 mM sodium cacodylate buffer pH 7.2 containing 0.5 mg/ml of ruthenium red as described above. Ultrathin sections were analyzed with a Leo 912AB\transmission electron microscope, and for each experimental condition 20 randomly selected cellular profiles were acquired using EsivisionPro 3.2 software Montage Image Acquisition mode (MIA) (nominal magnification 8,000K, final montage size 12,9x12,9µm). Montages were opened and analyzed with ImageJ software. The different endocytic structures containing gold particles were classified as: vesicular-tubular, small endocytic structures close to the PM containing few gold particles; Early/Recycling endosomes (EE/RE) larger organelles round or pleiomorphic with an electrolucent vacuole, sometimes with one or multiple tubules extending from them and/or with a cytoplasmic coated associated with the

membranes; Late endosomes/multivesicular bodies (LE/MVB) larger round structures containing degraded material or numerous intraluminal vesicles (ILVs). The amount of CD147 labeling in the different compartments has been calculated dividing the total amount of gold particles for the length of the PM or the cytosolic area of the cellular profile.

ER morphometry. Surface area, major and minor axis of ER profiles were calculated by semi-automatic segmentation of HRP-positive ER structures in digital micrographs using the Frangi Filter of Microscope Image Browser ver.1.10, as in Belevich et al., 2016.

For the analysis of ER morphology (Fig. S5B) from micrographs of randomly selected cellular profiles acquired at 1840x magnification, HRP-positive ER profiles were automatically segmented with MIB software. The major axis of the segmented ER profiles was used to calculate the frequency distribution of the length of the ER profiles.

For the classification and the distribution of peripheral ER profiles (Fig. S5C) the peripheral ER of 20 random selected cellular profiles was acquired at a nominal magnification of 4000x. HRP-KDEL–labeled ER was automatically segmented by MIB software, and where present, ER nuclear envelope or vesicle in proximity of the trans-Golgi network (TGN) were manually excluded. ER profiles were classified as large (L), medium (M) and small (S) profiles according to their major and minor axes (L: major axis >1000 nm; M: major axis 500 – 1000 nm and minor axis >110 nm; S major axis <500 nm and minor axis <110 nm) corresponding respectively to ER tubules, an intermediate ER compartment and ER sheets (*20, 48*). The density of the ER profiles was calculated dividing the number of segmented profiles for the cytosolic surface of each cellular profile (measured with ImageJ).

For quantification of the distribution of juxta-plasma membrane ER upon EGF stimulation (Fig. 4D), 20 randomly selected cellular profiles per condition were acquired at a magnification of 4000x. HRP-KDEL–labeled ER and PM were segmented as described above. The minimum distances between the PM and all the ER profiles present in each cellular profile were automatically measured by means of mtk program of IMOD software package as described by McDonald et al., 1992, and plotted as the number of segmented profiles in relation to the distance from the PM (bin size 20 nm).

All statistical analyses were performed using GraphPad Prism. Two-tailed Student's t test or One-way ANOVA, as indicated, were used to calculate statistical significance among different samples. In the case of One-way ANOVA, Dunnett's Multiple Comparison post-hoc test was applied when multiple samples were compared; Bonferroni's Multiple Comparison Test post-hoc test was applied when different conditions of two samples were compared.

Serial Sections and Transmission Electron Tomography. For serial sections, ultrathin sections (70 – 90 nm) were obtained with the UC7 ultramicrotome (Leica microsystem, Vienna, Austria), collected on formvar-coated slot grid, stained with uranyl acetate and Sato's lead solutions, and observed using a Transmission Electron Microscope (Leo 912AB, Carl Zeiss, Oberkochen, Germany). Digital micrographs were taken with a 2Kx2K bottom mounted slow-scan camera (ProScan, Lagerlechfeld, Germany) controlled by the EsivisionPro 3.2 software (Soft Imaging System, Münster, Germany). Serial section images were aligned with IMOD software package, the ER profiles of HRP-KDEL transfected cells were semi-automatically segmented with the Frangi Filter of Microscope Image Browser ver.1.10 and visualized in IMOD software.

For electron tomography, 200 – 250 nm thick sections were collected on formvar-coated copper slot grids using a Leica EM UC7 ultramicrotome (Leica Mikrosysteme GmbH Vienna, Austria). Colloidal gold particles (10 nm) were applied as fiducials on both surfaces of the grids and the samples were imaged on a 200 kV Tecnai G2 20 electron microscope (FEI, Eindhoven) at a magnification of 25000x, resulting in pixel sizes of 0.92 nm. Single tilted image series (± 65° according to a Saxton scheme with the initial tilt step of 2°) were acquired using Xplorer 3D (FEI, Eindhoven) with an Eagle 2,048 × 2,048 CCD camera (FEI, Eindhoven). Tilted series alignment, tomographic reconstructions, image segmentation and visualization were performed with the IMOD software package as described in Kremer et al., 1996.

Measurements of intracellular Ca^{2+} concentration

Aequorin measurements. Cells grown on 13-mm-round glass coverslips at 50% confluence were transfected with the appropriate cytosolic (cyto)- or PM-targeted aequorin chimeras. Aequorin constructs and protocols were previously described (49). All aequorin measurements were performed in KRB buffer (135 mM NaCl, 5 mM KCl, 0.4 mM KH_2PO_4, 1 mM $MgSO_4$, 20 mM HEPES and 5.5 mM glucose, pH 7.4), supplemented with 1 mM Ca^{2+}. When EGTA treatment was performed, aequorin measurements were recorded in KRB buffer plus 100 μM EGTA. Stimulation with EGF was performed as specified in the figure legends. The experiments were terminated by lysing the cells with 0.01% Triton in a hypotonic Ca^{2+}-rich solution (10 mM $CaCl_2$ in H_2O), thus discharging the remaining aequorin pool. The light signal was collected and calibrated into [Ca^{2+}] values, as previously described (*49*). Extents of Ca^{2+} waves were expressed as area under the curve (AUC) and maximal value of peak in box plot graphs (whiskers min to max). Statistical analysis was performed using GraphPad Prism. Two tailed Student's t test was used to calculate statistical significance among different samples.

Fura-2, AM, Measurements. The cytosolic Ca^{2+} response upon xestospongin C treatment was evaluated on a single cell basis using the fluorescent ratiometric Ca^{2+} indicator Fura-2 AM, as the response displayed significant intercellular heterogeneity. Note also that results achieved using aequorin were all confirmed with Fura-2, AM, (high vs. low doses of EGF; EGTA treatment; RTN3 KD vs. RTN4 KD effect). Cells were grown on 24-mm coverslips and incubated at 37°C for 30 min in 1 mM Ca^{2+}/KRB supplemented with 2.5 mM Fura-2 AM, 0.02% Pluronic F-68, and 0.1 mM sulfinpyrazone. The cells were then washed and supplemented with 1 mM Ca^{2+}/KRB. To determine the cytosolic Ca^{2+} response, cells were placed in an open Leyden chamber on a 37°C thermostat-controlled stage and exposed to 340/380 nm wavelength light using the Olympus xcellence multiple-wavelength high-resolution fluorescence microscopy system equipped with an ORCA ER CCD camera (Hamamatsu Photonics) and an Uplan FLN 40X oil objective (Olympus). After registration of baseline ratio, cells were stimulated with Alexa555-EGF. Fluorescence data collected were expressed as emission ratios. The extent of Ca^{2+} waves was expressed as AUC in box plot graphs (whiskers min to max). Statistical analysis was performed using GraphPad Prism. One-way ANOVA was used to calculate statistical significance between different samples.

Xestospongin C treatment

Cells were treated with 2 μM xestospongin C for 16 h or 10 μM for 1 h. The drug was kept for the duration of the different experimental procedures (Fura-2 AM measurements, or CD147 internalization followed by EM/IF analysis).

Calcium depletion with ionomycin

Calcium depletion was obtained by administration of 100 μM EGTA in a calcium free KRB supplemented with 1 μM ionomycin at 4°C. Forty-five minutes of depletion procedure was sufficient to induce complete depletion of Ca^{2+}, as previously described (*50*).

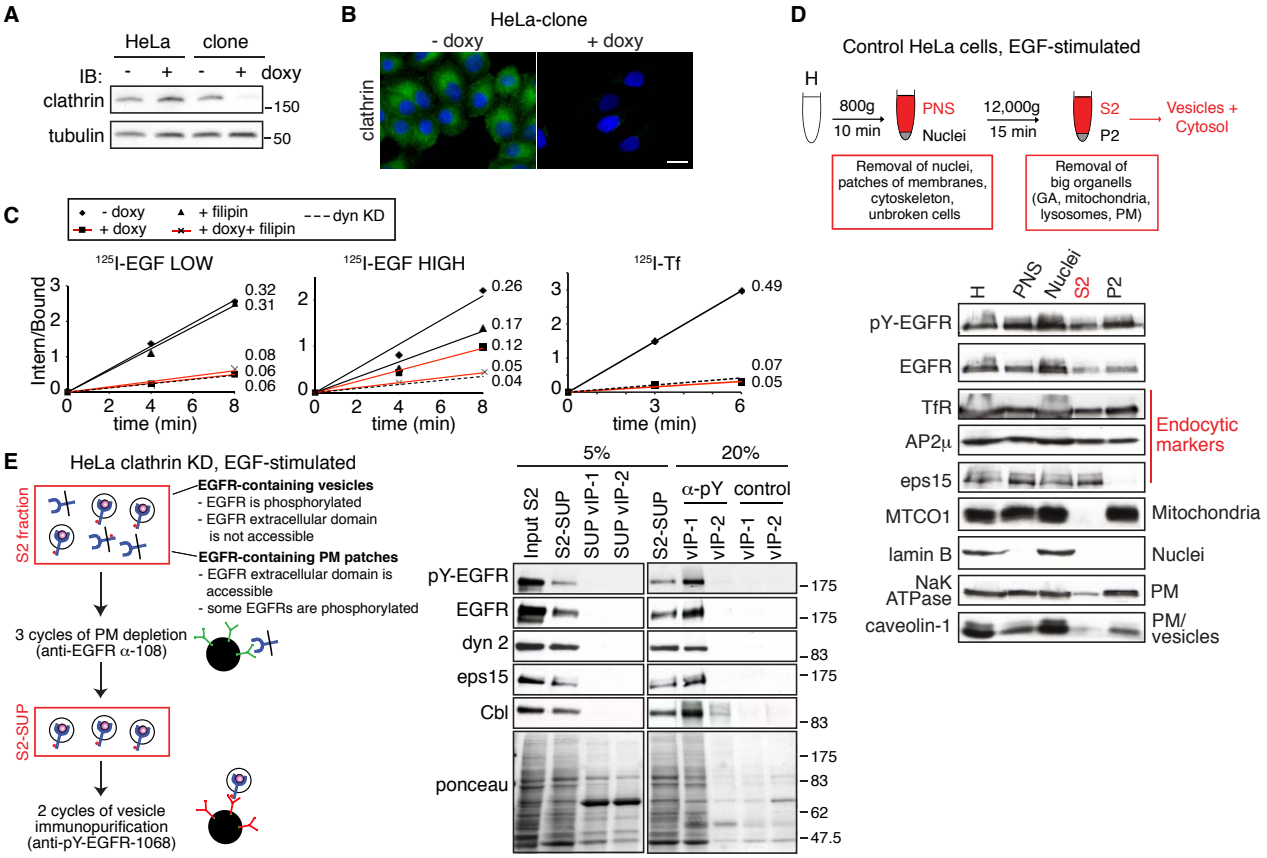

Figure S1

Fig. S1. Setting up of the vesicle immunopurification procedure.
(**A**) HeLa cells were infected with a lentivirus harboring an inducible silencing oligo for the clathrin heavy chain. The efficiency of clathrin knockdown (KD) upon doxycycline (doxy) treatment was assessed by immunoblotting (IB) in the inducible clone that was selected for all subsequent experiments. HeLa cells were used as control. Tubulin, loading control. Molecular size markers are on the right. (**B**) Clathrin KD was assessed also by IF in the HeLa clone. Bar, 10 μm. Green, clathrin. Blue, DAPI. (**C**) Representative kinetics of ^{125}I-EGF internalization in the HeLa clone at low (1 ng/ml) and high (30 ng/ml) doses of EGF, upon induction of clathrin KD with doxy, in the absence or presence of filipin, a cholesterol-interfering drug that blocks NCE (*4*). At low EGF (left panel), ligand internalization was almost completely blocked by doxy treatment, confirming that only CME is active at this dose. At a high EGF (middle panel), doxy treatment alone inhibited ligand internalization by approximately 55%, while filipin treatment alone inhibited internalization by 35%. When cells were treated with doxy and filipin together, the residual internalization was reduced to 'background' levels, i.e. the same level observed upon dynamin KD (dyn KD). These results are in agreement with previously published data (*8*) and further support the notion that both CME and NCE are active at high EGF concentrations in the HeLa clone. The internalization of ^{125}I-Tf (entering only through CME, right panel) was reduced upon doxy treatment to levels indistinguishable from those obtained in the presence of dyn KD. The internalization

constants (Ke) are reported on the right of each curve. (**D**) Top, schematic representation of the sequential subcellular fractionation. Shown is a representative fractionation experiment performed with HeLa control cells (not knocked-down for clathrin). Cells were stimulated with EGF (100 ng/ml) and then manually homogenized in an isotonic reducing buffer. The homogenate (H) was first diluted to reduce the formation of aggregates, and then centrifuged at low speed (800g) to obtain a Post Nuclear Supernatant (PNS) devoid of nuclei, large patches of membranes and cytoskeleton. The PNS was then centrifuged at medium speed (12,000g) to remove PM and large organelles, such as Golgi and mitochondria, and to achieve an enriched vesicular fraction (S2). Bottom, an equal volume of each fraction (corresponding to equal amount of cells) was loaded on triplicate gels and analyzed by IB for different markers. Endocytic markers (TfR, AP2μ, eps15), caveolin-1, as well as EGFR and phosphorylated-EGFR (pY1068) were detected in the S2 fraction. Loss of the nuclear marker lamin B and of the mitochondrial marker MTCO1 in S2 suggests that most cellular contaminants were removed. However, the presence of traces of NaK ATPase indicates the presence of residual PM contamination in the vesicular fraction. For this reason, the S2 fraction (input S2) was further subjected to a PM depletion step (see Fig. 1A and panel E of this figure). (**E**) Left, the procedure described in (D) was repeated in HeLa clathrin KD stimulated for 8 min with high EGF dose and the S2 fraction was subjected to three cycles of immunodepletion with magnetic beads (Pan mouse Dynabeads) cross-linked with mAb108 that recognizes the EGFR extracellular domain. In an initial experiment, after the third depletion step (S2-SUP), the supernatant was subjected to two further cycles of immunopurification with magnetic beads (Pan mouse Dynabeads), this time cross-linked with mAb-pY1068-EGFR that recognizes activated receptor. Right, IB analysis of the different steps depicted in the left panel. Samples were loaded on duplicate gels that were subjected to IB with different markers. This panel was assembled from samples run on the same gel by splicing out the irrelevant lanes. From left to right: the comparison between the input S2 fraction and the S2-SUP fraction obtained after the three immunodepletion steps (5% of the total material was loaded) shows that around 50% of the initial EGFR and pY1068-EGFR is depleted. This is probably due, as expected, to the residual presence in the S2 fraction of patches of PM harboring EGFR whose extracellular domain is available for interaction with the mAb108. Moreover, some depletion also occurred for endocytic markers (eps15, Cbl and dyn 2) between "input-S2" and "S2-SUP", although to a reduced extent, as would be expected for proteins putatively present both at the PM and in endocytic vesicles. Upon additional rounds of immunopurification with the anti-pY-EGFR-1068 Ab, we observed an almost complete depletion of all proteins involved in EGFR endocytosis already in the first cycle of immunopurification, as evident from the IB of the supernatants of the two rounds of vesicle immunopurification (vIP), SUP vIP-1 and SUP-vIP-2. This depletion was confirmed by IB analysis of recovered material (lanes vIP-1 and vIP-2, 20% of the sample loaded) that showed that most of the proteins of interest were immunopurified in the first cycle. Based on these results, we performed a single cycle of vIP prior to mass spec analysis. Molecular weight markers are shown on the right. As control, incubation with magnetic beads coated only with anti-mouse secondary antibody (Pan mouse Dynabeads without primary antibody) was performed.

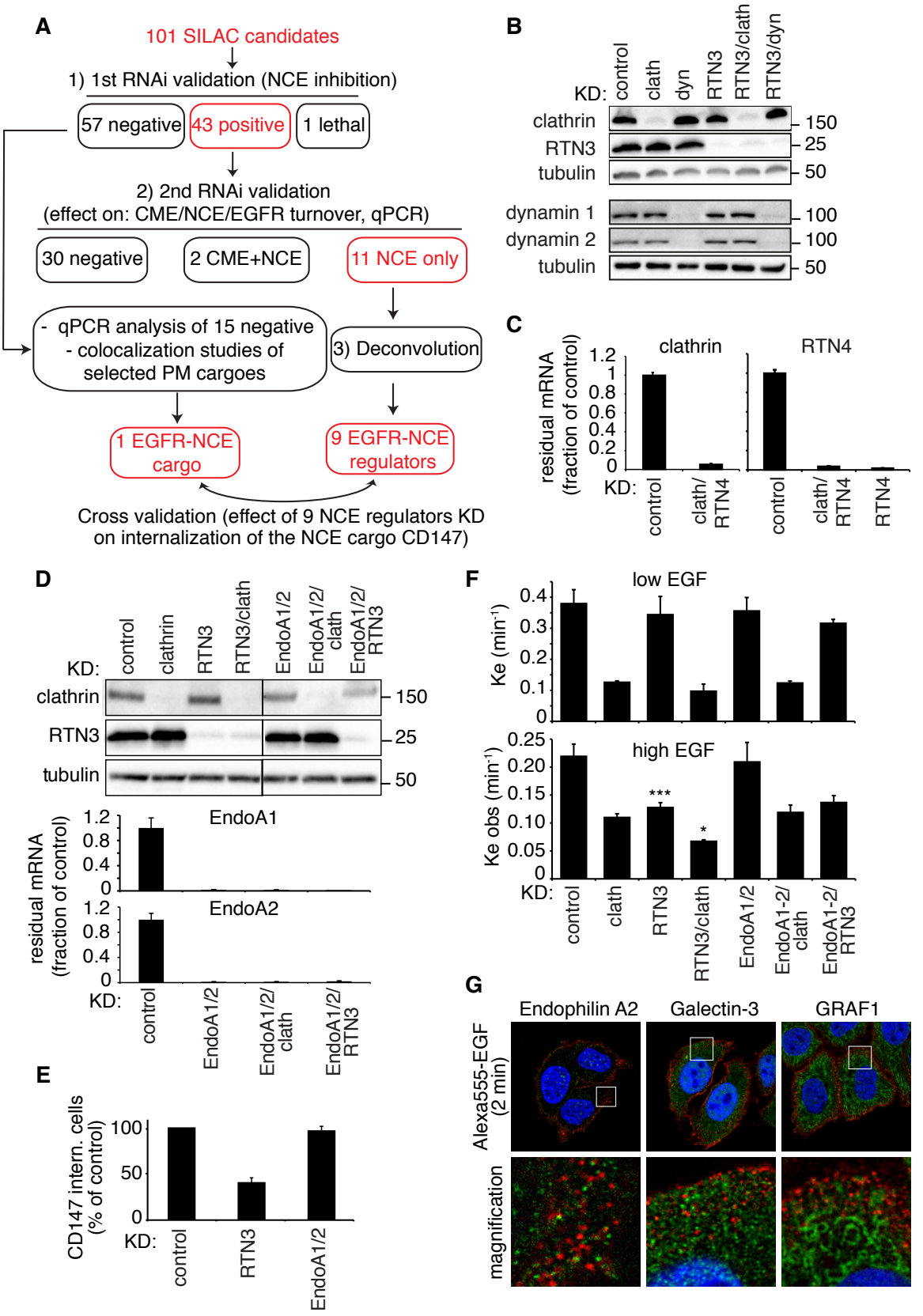
A
101 SILAC candidates
1) 1st RNAi validation (NCE inhibition)
57 negative
43 positive
1 lethal
2) 2nd RNAi validation
(effect on: CME/NCE/EGFR turnover, qPCR)
30 negative
2 CME+NCE
11 NCE only
- qPCR analysis of 15 negative
- colocalization studies of
selected PM cargoes
3) Deconvolution
1 EGFR-NCE cargo
9 EGFR-NCE regulators
Cross validation (effect of 9 NCE regulators KD
on internalization of the NCE cargo CD147)
B
KD: control clath dyn RTN3 RTN3/clath RTN3/dyn
clathrin
RTN3
tubulin
dynamin 1
dynamin 2
tubulin
150
25
50
100
100
50
C
clathrin
RTN4
residual mRNA (fraction of control)
KD: control clath/ RTN4 RTN4
D
KD: control clathrin RTN3 RTN3/clath EndoA1/2 EndoA1/2/ clath EndoA1/2/ RTN3
clathrin
RTN3
tubulin
EndoA1
EndoA2
residual mRNA (fraction of control)
E
CD147 intern. cells (% of control)
KD: control RTN3 EndoA1/2
F
low EGF
high EGF
Ke (min-1)
Ke obs (min-1)
KD: control clath RTN3 RTN3/clath EndoA1/2 EndoA1-2/ clath EndoA1-2/ RTN3
G
Endophilin A2
Galectin-3
GRAF1
Alexa555-EGF (2 min)
magnification

Figure S2

Fig. S2. Additional information and controls of the RNAi validation screening.

(**A**) Flowchart of the screening validation procedure. The 101 'high-confidence' NCE candidates were selected from the SILAC list by adopting stringent criteria: they are in the Top 20% list, present in 3 out of 3 replicas, quantified with high confidence (RC>2) and ranked by decreasing ratio H/L expressed as the median value among the three experiments (see Materials and Methods). These proteins were ablated using a pool of 4 oligos in combination with clathrin KD (using the HeLa clone). The effect of their KD was tested in ^{125}I-EGF internalization assays at high dose of ligand for the ability to reduce or increase by at least 1.5-fold the internalization rate compared to clathrin KD [1), 1st RNAi validation, see also File S2, spread-sheet 1-2]. 43 genes passed this initial test ("positive"), while 57 genes were "negative" and 1 was "lethal".

The 43 positives were subjected to a multilayered second round of validation, described in detail in the main text [2) 2nd RNAi validation, see also File S2, spread-sheet 3-8]. In addition, we performed qPCR analysis of all 43 candidates, which showed that efficient KD levels were achieved in all cases (File S2, spread-sheet 4 and unpublished data). At the end of the second round of validation, 11 genes were found to be specifically involved in EGFR-NCE. Of these, 9 survived a deconvolution analysis (3) (File S2, spread-sheet 9), yielding the final list of the 9 NCE regulators (see Fig. 2A).

The 57 genes that scored "negative" in the initial round of validation were also further analyzed. As shown (and to further control our procedure), we performed a qPCR analysis of 15 randomly selected genes, to ensure that the negative result was not due to inefficient KD. We confirmed, in the tested cases, efficient KD. In addition, some of the "negatives" showed sequence characteristics of PM-resident proteins. A number of these proteins were characterized by localization studies and co-localization studies with internalized EGF (our unpublished results). This led to the identification of a specific NCE cargo, CD147, which was used for the cross-validation of NCE regulators. The impact of NCE regulator KD on CD147 internalization is reported in Fig. 2A. (**B**) Efficiency of RTN3 KD alone or in combination with the indicated genes, as assessed by IB. Molecular weight markers are shown on the right. Tubulin, loading control. Samples were loaded on two parallel gels (top and bottom). Dynamin 1 was blotted on the same membrane of dynamin 2 after stripping and re-blotting. (**C**) Efficiency of RTN4 KD assessed by qPCR. Residual mRNA expression in the KD samples was normalized using a housekeeping gene (GusB) and expressed as a fraction of control. (**D**) Top, efficiency of RTN3 and clath KD, alone or in combination with Endophilin A1 and A2, was assessed by IB. This panel was assembled from samples run on the same gel by splicing out the irrelevant lanes. Bottom, efficiency of Endophilin A1 and A2 KD in the indicated samples was assessed by qPCR. Residual mRNA expression in the KD samples was normalized using a housekeeping gene (GusB) and expressed as a fraction of control. Note that Endophilin A3 was not detected. (**E**) CD147 internalization was followed upon RTN3 and EndoA1/A2 KD (see Materials and Methods). Results are expressed as the percentage of CD147 internalizing cells in different fields ± SD. (**F**) Internalization constants were measured by ^{125}I-EGF internalization at low (top) and high (bottom) doses of ligand upon KD of the indicated proteins. Data are the mean ± SD and P-values were calculated using Each Pair Student's t test. P-values are for RTN3 and EndoA1/2 *vs.* control; RTN3/clath, EndoA1/A2/clath *vs.* clath; Endo1/A2/RTN3 *vs.* RTN3. *, $P < 0.05$, ***, $P < 0.001$. Note that EndoA1/A2 KD alone or in combination displayed no

significant effect on EGFR internalization. (**G**) Colocalization studies of EGFR-NCE with markers of previously described clathrin-independent pathways. Immunofluorescence analysis of Alexa555-EGF (red) at 2 min of stimulation in clathrin KD cells stained (in green) for Endophilin A2 (*51*), galectin-3 (*52*) or GRAF1 (*15*). None of the markers showed colocalization with EGFR-NCE structures, confirming the functional data summarized in Table S1.

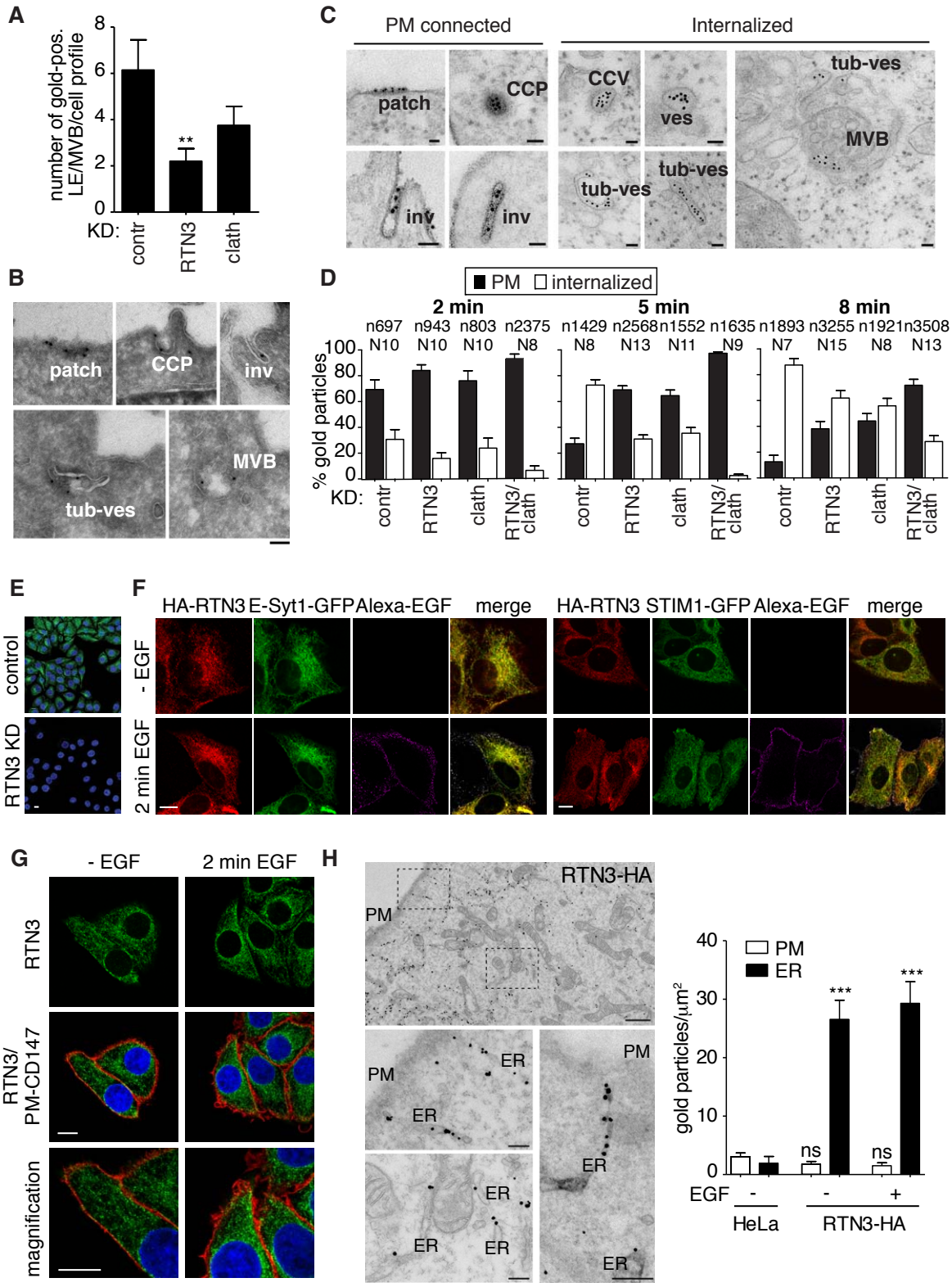
A
number of gold-pos. LE/MVB/cell profile
8
6
4
2
0
**
KD:
contr
RTN3
clath
B
patch
CCP
inv
MVB
tub-ves
C
PM connected
Internalized
patch
CCP
CCV
ves
tub-ves
MVB
inv
inv
tub-ves
tub-ves
D
PM
internalized
2 min
5 min
8 min
n697 N10
n943 N10
n803 N10
n2375 N8
n1429 N8
n2568 N13
n1552 N11
n1635 N9
n1893 N7
n3255 N15
n1921 N8
n3508 N13
% gold particles
100
80
60
40
20
0
KD:
contr
RTN3
clath
RTN3/ clath
E
control
RTN3 KD
F
HA-RTN3
E-Syt1-GFP
Alexa-EGF
merge
HA-RTN3
STIM1-GFP
Alexa-EGF
merge
- EGF
2 min EGF
G
- EGF
2 min EGF
RTN3
RTN3/ PM-CD147
magnification
H
RTN3-HA
PM
PM
ER
ER
PM
ER
ER
ER
ER
gold particles/μm²
40
30
20
10
0
PM
ER
***
***
ns
ns
EGF
-
-
+
HeLa
RTN3-HA

Figure S3

Fig. S3. **Additional electron microcopy experiments and colocalization studies.**
(**A**) Quantification of EGFR-gold labeled late endosome/multivesicular bodies (LEs/MVBs) ± SEM in the indicated conditions at 8 min of EGF stimulation. P-values were calculated with One-way ANOVA. **, P< 0,01. (B-D) Ultrastructural analysis of EGFR endocytic pathways. (**B**) Cryosection analysis of cells stimulated with high dose Alexa-488 EGF and stained with anti-Alexa antibody to visualize PM-connected structures internalizing EGF. Note that the same type of structures, as those observed with the pre-embedding immunolabeling technique (panel C), can be visualized: PM patches, clathrin-coated pits (CCP), invaginations (inv), tubular vesicles (tub-ves) and multi-vesicular bodies (MVBs). (**C**) Representative images of gold-EGFR positive structures. The left panels depict structures still connected to the PM (ruthenium red positive), including patches, clathrin-coated pits (CCP), and invaginations (inv). In the right panel, examples of gold-EGFR internalizing structures (ruthenium red negative) are shown, including clathrin-coated vesicles (CCV), vesicles (ves), tubular vesicles (tub-ves) and multi-vesicular bodies (MVBs). Bars, 50 nm. (**D**) Quantification of PM *vs*. internalized gold-labeled EGFR upon stimulation with high dose of EGF for 2, 5 and 8 min (the 5 min time point is the same reported in Fig. 3D), in the indicated KD conditions. Gold particles (EGFR) at the PM (black bars) were distinguished from internalized ones (white bars) by staining the cell surface with ruthenium red. N and n represent the number of cell profiles and the number of counted gold particles, respectively. Results are expressed as percentage ± SEM. (E-H) RTN3 localization analyses. (**E**) Characterization of the specificity of the anti-RTN3 antibody produced in-house (green, see Materials and Methods for further information), by IF analysis of HeLa control or RTN3 KD cells. The signal detected in control cells is specific since it disappeared in KD cells. Bars, 10 μm. Blue, DAPI. (**F**) Colocalization by IF analysis of HA-RTN3 (red) and the ER-resident proteins E-Syt1-GFP (green, left panels) or STIM1-GFP (green, right panels), co-transfected in HeLa cells stimulated or not with high dose Alexa647-EGF (magenta) for 2 min. In the merge panel, Alexa647-EGF is shown pseudocolored in grey. Bars, 10 μm. (**G**) Analysis of endogenous RTN3 localization with the antibody described in (E) in cells not stimulated or stimulated with high dose of EGF for 2 min. Cells were stained for CD147 (red) prior permeabilization, to stain only the PM, and for RTN3 (green) after permeabilization. Magnification is shown at the bottom. Bars, 10 μm. Blue, DAPI. (**H**) HeLa cells stably expressing HA-RTN3 Isoform A at endogenous levels (see Fig. 5C) were transfected with HRP-KDEL (visible as an electrondense precipitate) and stimulated or not with high dose of EGF. Cells were incubated with DAB/H_2O_2 to visualize the ER, and then subjected to pre-embedding immunolabeling with anti-HA antibody (see Materials and Methods). Left, a representative picture of the distribution of RTN3 is shown and two selected areas are magnified in the bottom panels. In the bottom left panel, a detail of an HRP-KDEL transfected cell shows an ER tubular profile highly labeled for RTN3. Bars, 1μm upper panel, 250nm lower panels. Right, quantitation of gold-labeled RTN3 localized in proximity (≤ 20 nm) of the ER or of the PM (in absence of ER proximity) ± SEM in the indicated samples. P-values were calculated with One-way ANOVA. ***, P< 0,001; ns, not significant.

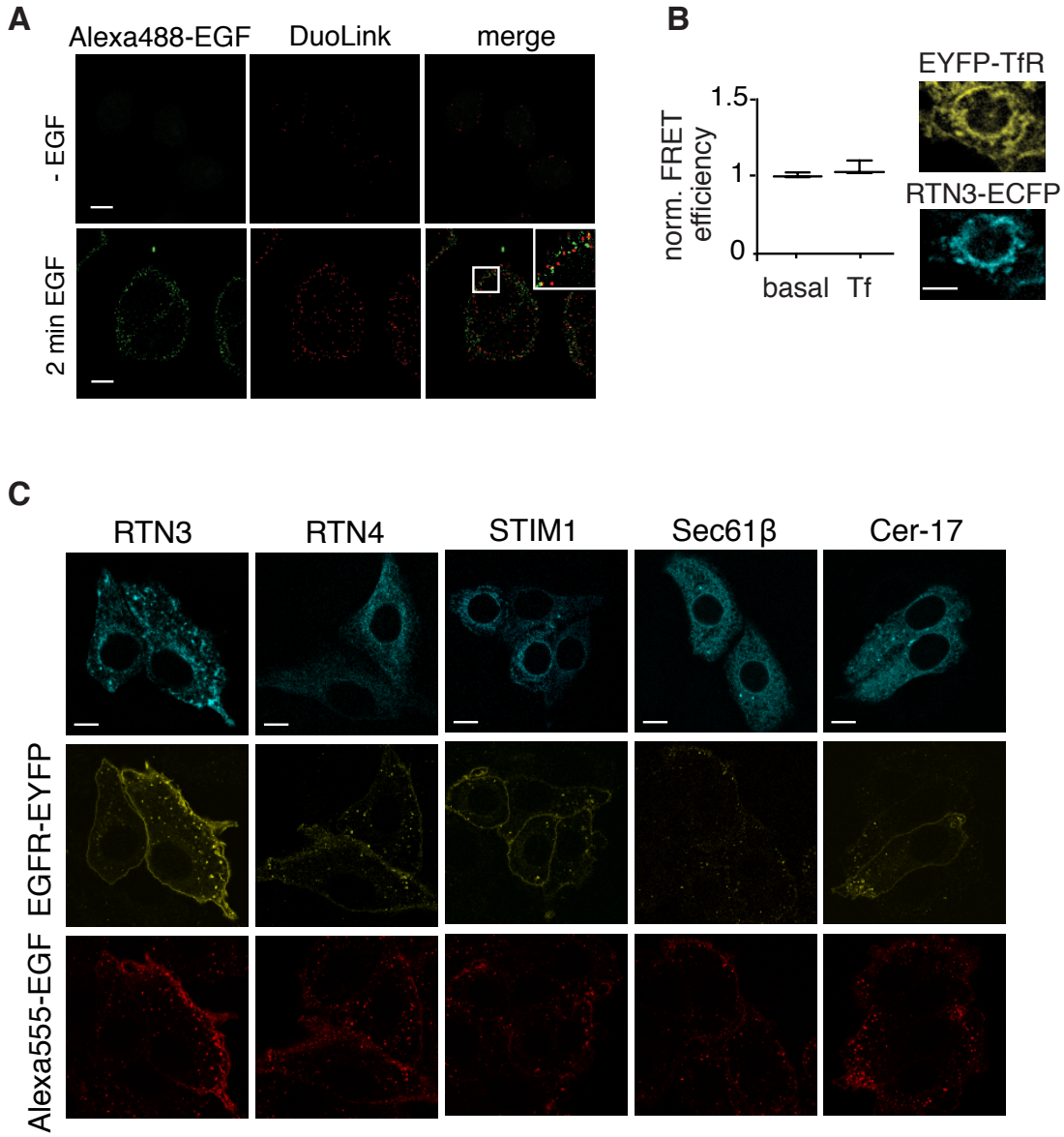
A
Alexa488-EGF
DuoLink
merge
- EGF
2 min EGF
B
EYFP-TfR
RTN3-ECFP
norm. FRET efficiency
1.5
1
0
basal
Tf
C
RTN3
RTN4
STIM1
Sec61β
Cer-17
EGFR-EYFP
Alexa555-EGF
D
High EGF
High EGF
Ke (% of contr)
100
80
60
40
20
0
KD:
contr
clath
dyn
E-Syt1/2/3
E-Syt1/2/3 /clath
STIM1/2
STIM1/2 /clath

Figure S4

Figure S4. Additional experiments and controls of RTN3-EGFR proximity.
(**A**) Orange Duolink proximity ligation assay using anti-RTN3 and anti-pY1068-EGFR antibodies as probes, in the indicated samples. A strong Duolink signal (red dots) was observed in cells stimulated with high dose of Alexa488-EGF (green), suggesting that activated EGFR and RTN3 are in close proximity (distance ≤ 30 nm) upon EGF stimulation. Insets show points of juxtaposition between Duolink signal and Alexa488-EGF at the cell periphery. Bars, 10 μm. (**B**) Sensitized Emission FRET analysis. Shown are the normalized EYFP-TfR/RTN3-ECFP FRET efficiencies in the control sample, before (basal) and after treatment with Alexa555-Tf. Representative images are shown. Bar, 10 μm. (**C**) Localization of the indicated CFP-tagged constructs, or cerulean, and EGFR-YFP upon stimulation with Alexa555-EGF for 5 min. Bars, 10 μm. (**D**) Internalization constants were measured by ^{125}I-EGF internalization at high doses of ligand upon KD of the indicated proteins. Data are expressed as % of control ± SD. Level of KD in the different samples was controlled by qPCR and reached at least 90% of control sample.

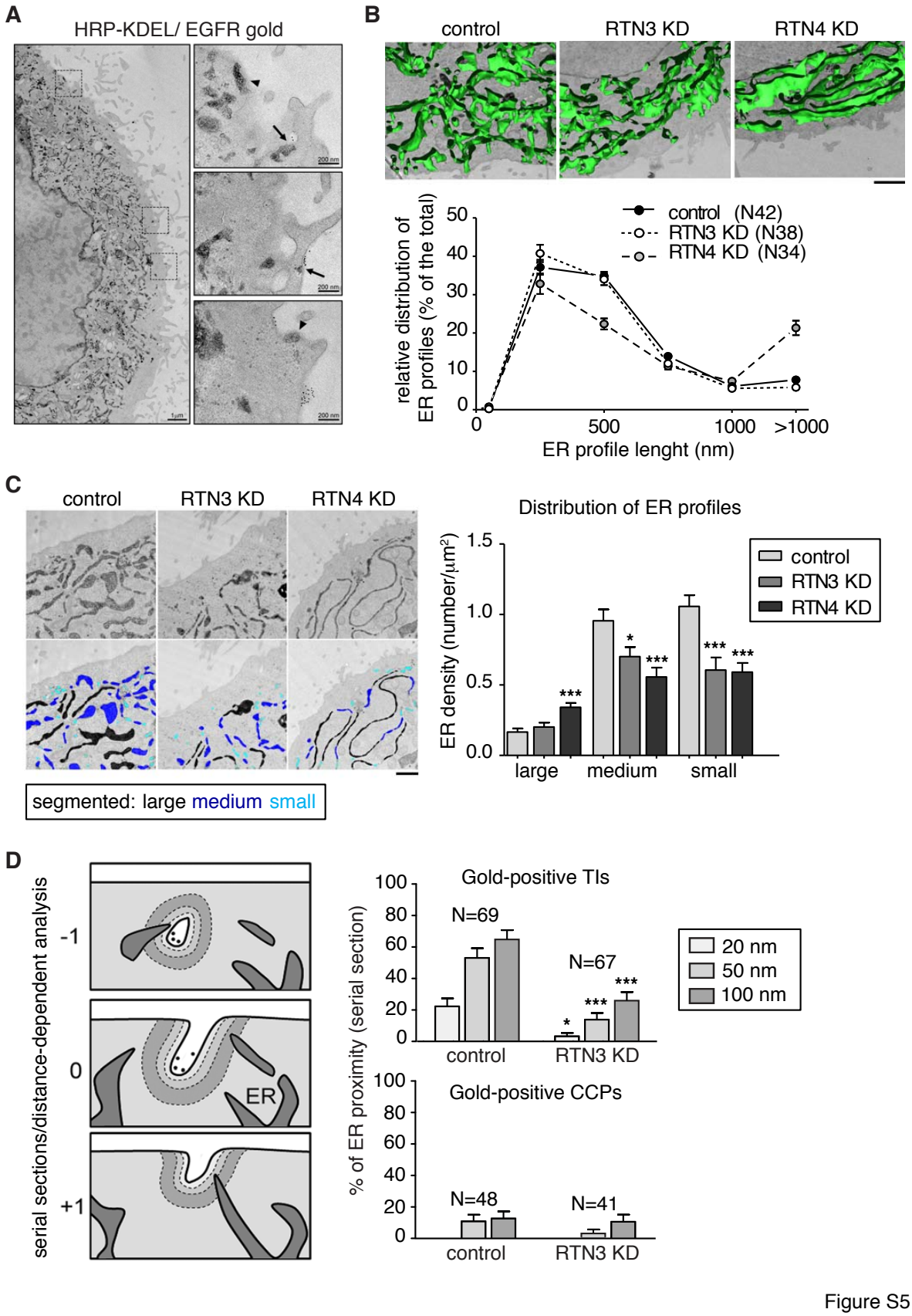
A
HRP-KDEL/ EGFR gold
B
control
RTN3 KD
RTN4 KD
relative distribution of ER profiles (% of the total)
control (N42)
RTN3 KD (N38)
RTN4 KD (N34)
ER profile lenght (nm)
C
control
RTN3 KD
RTN4 KD
segmented: large medium small
Distribution of ER profiles
ER density (number/µm²)
large
medium
small
D
serial sections/distance-dependent analysis
-1
0
+1
ER
Gold-positive TIs
N=69
N=67
Gold-positive CCPs
N=48
N=41
% of ER proximity (serial section)
20 nm
50 nm
100 nm

Figure S5

Figure S5. ER morphology and ER-PM contact sites upon depletion of RTN3 or RTN4.

(**A**) Cells were transfected with HRP-KDEL (visible as an electrondense precipitate) and stimulated with high dose of EGF (EGFR labeled with gold). Insets show the ER in contact with the PM and with gold-labeled PM domains. Bars: left 1 μm, right 200 nm. (**B**) Top, 3D visualization of the ER in HRP-KDEL transfected control, RTN3 KD and RTN4 KD cells through electron microscopy of serial sections. In control HeLa cells, the complex ER network is composed of interconnected tubules and cisternae; upon RTN4 KD the ER morphology is strongly affected and mostly of the ER profiles correspond to parallel cisternae. Removal of RTN3 gives rise to a subtler phenotype with a minor decrease of tubular structures. Bar, 1μm. Bottom, frequency distribution of the length of the ER profiles ± SEM in control, RTN3 KD and RTN4 KD cells. The lengths of the major axis of ER profiles were grouped into 250 nm bins and plotted as percentage of total number of ER profiles (see Materials and Methods for explanation of image segmentation analysis). Note the higher percentage of long ER profiles corresponding to cisternae in RTN4 KD cells. (**C**) Classification and distribution of peripheral ER profiles. Peripheral ER profiles from HRP-KDEL transfected cells were segmented and classified as small, medium and large structures based on their size as described in the Materials and Methods. On the left, representative original EM images in the upper row and color-coded segmented images in the lower row. Bar, 1 μm. On the right, a graph showing the distribution of the three categories of the ER profiles in control, RTN3 KD and RTN4 KD cells expressed as the number of ER profiles per cellular profile area ± SEM. P-values were calculated with One-way ANOVA. *, $P < 0.05$, ***, $P < 0.001$ (*vs.* control). (**D**) Left, cartoon illustrating serial sectioning. Right, distance-dependent analysis (20 nm, 50 nm, 100 nm) of contact sites between EGFR-containing structures (gold labeled) and the ER (HRP-KDEL) in HeLa cells stimulated with high dose of EGF for 5 minutes. Mean frequency of ER proximity with gold EGFR-labeled TIs (top) or CCPs (bottom) at the indicated distances, expressed as percentage ± SEM. Note that the contacts between TIs and ER increase as a function of the cut-off distance (top panel). Of note, association of ER with CCPs is a rare event (bottom panel). P-values were calculated with One-way ANOVA. *, $P < 0.05$, ***, $P < 0.001$ (*vs.* control).

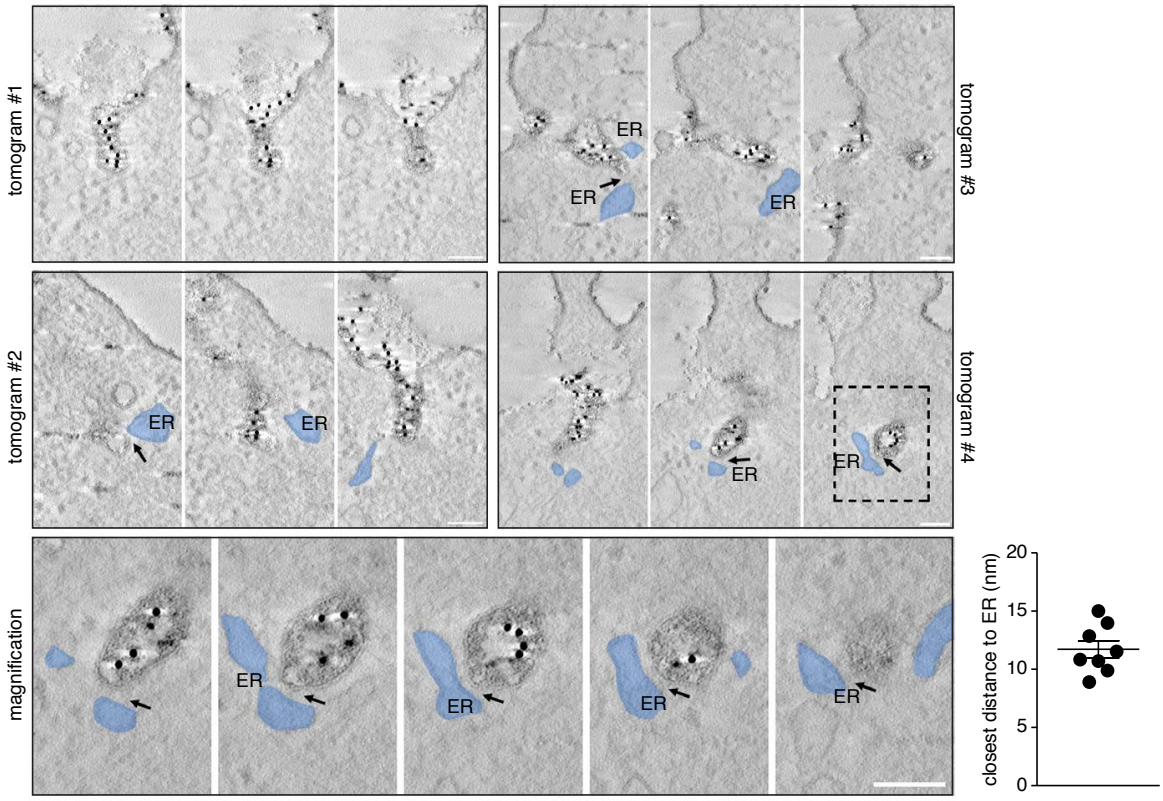

Figure S6

Figure S6. Electron Tomographic 3D reconstruction of CD147-positive TIs.
Cells were surface labeled with anti-CD147 antibody, stimulated with high dose of EGF for 5 min and fixed as for standard EM procedure (see Materials and Methods). We randomly selected 11 CD147-positive TIs. 200-250 nm thick sections were collected and processed for electron tomography. We found that 8 out of 11 structures showed a contact with the ER (distance between the two heterologous membranes $\leq$ 20 nm). Single electron tomographic z-slices extracted from 4 different tomograms are here reported to show the tubular nature of the CD147 positive structures. In tomograms #2-4, the close association with the ER (pseudocolored in blue) is highlighted by black arrows. In the lower panel, z-slices from tomogram #4 (shown also in the main text in Fig. 5G) shows the extent of association between ER and the tip of a CD147-positive endocytic structure. Scale bars 100 nm. The graph at the bottom right indicates the closest distance observed between the CD147-positive TI and the ER in the 8 tomograms where a contact is observed.

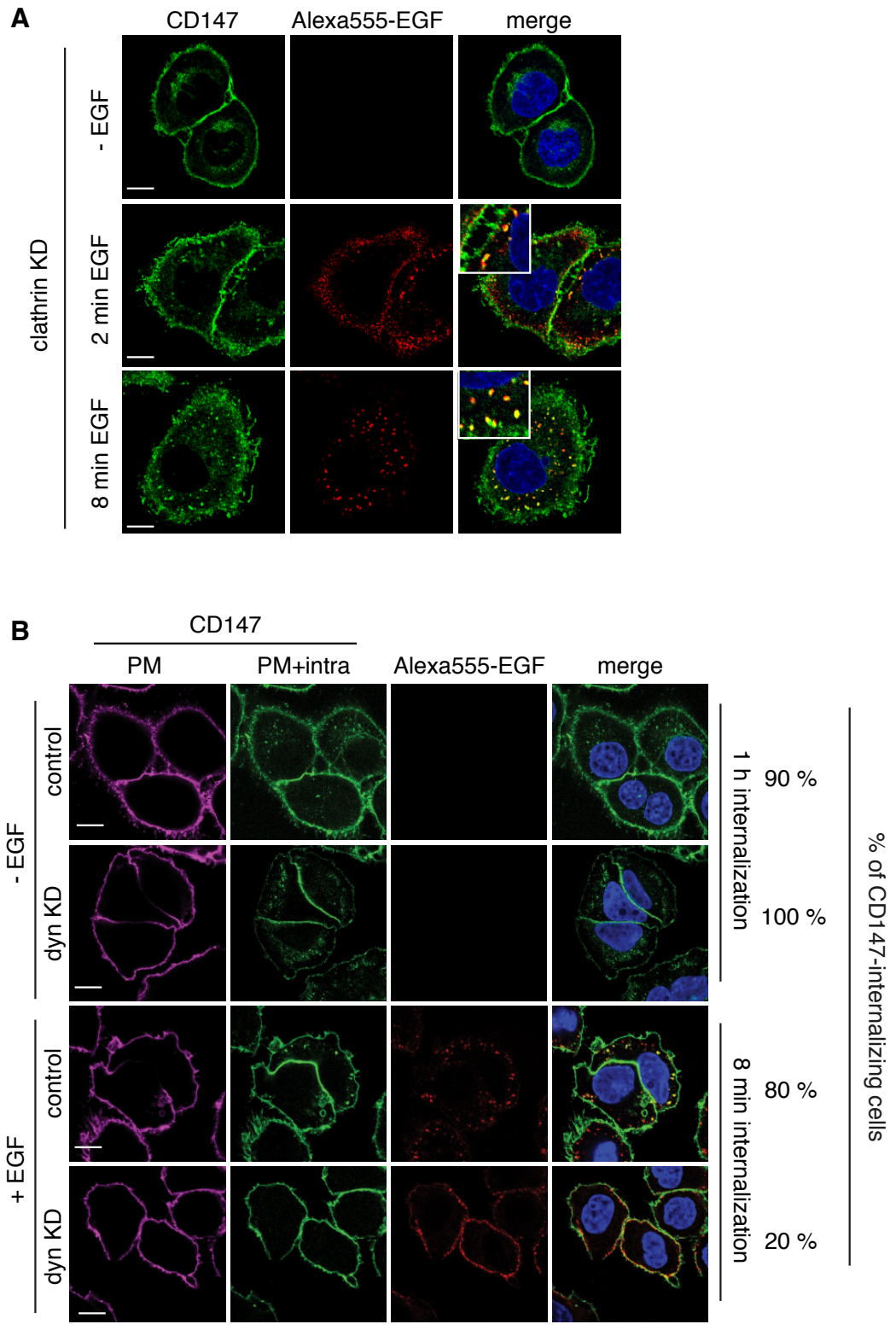
A
CD147
Alexa555-EGF
merge
clathrin KD
- EGF
2 min EGF
8 min EGF
B
CD147
PM
PM+intra
Alexa555-EGF
merge
- EGF
+ EGF
control
dyn KD
control
dyn KD
1 h internalization
90 %
100 %
8 min internalization
80 %
20 %
% of CD147-internalizing cells

Figure S7

Figure S7. CD147 is internalized through RTN3-dependent NCE.
(**A**) CD147 (green) localization in unstimulated cells or cells stimulated with Alexa555-EGF (red) for 8 minutes in clathrin KD cells. Insets from merged images highlight colocalization (yellow) between EGF and CD147. Bars, 10 μm. (**B**) EGF-induced CD147 internalization is dynamin-dependent. CD147 was previously shown to enter cells via a clathrin- and dynamin-independent pathway (*22*), while the EGFR-NCE pathway is dynamin-dependent (*8*). To resolve this apparent discrepancy, we followed the endocytosis of CD147, in the absence or in the presence of EGF stimulation, in control or in dynamin KD cells. Our results showed that CD147 is internalized slowly in absence of EGF, and intracellular dots of CD147 are detectable only after 1 h of antibody internalization (upper panels). The administration of EGF accelerated CD147 entry, and substantial endocytosis was visible already after 8 min of treatment (lower panels). Importantly, while basal endocytosis (in absence of EGF) is not inhibited by dynamin KD, EGF-induced internalization was severely impaired. These results show that EGF activates the entry of CD147 through the EGFR-NCE pathway, while, under basal conditions, CD147 enters through a slower clathrin- and dynamin-independent pathway, as previously shown (*22*). Bars 10 μm. Percentage of CD147-internalizing cells is shown on the right.

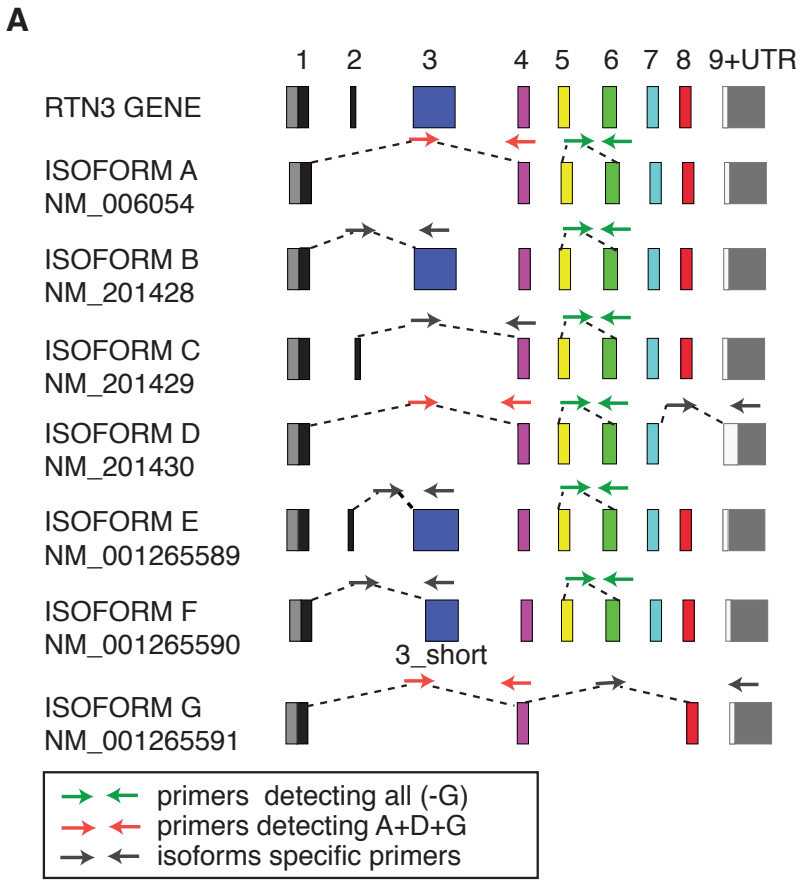
A
1 2 3 4 5 6 7 8 9+UTR
RTN3 GENE
ISOFORM A
NM_006054
ISOFORM B
NM_201428
ISOFORM C
NM_201429
ISOFORM D
NM_201430
ISOFORM E
NM_001265589
ISOFORM F
NM_001265590
3_short
ISOFORM G
NM_001265591
primers detecting all (-G)
primers detecting A+D+G
isoforms specific primers

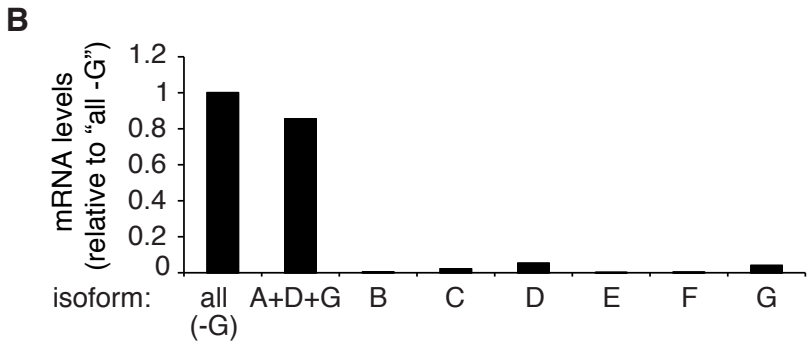
B
mRNA levels
(relative to "all -G")
1.2
1
0.8
0.6
0.4
0.2
0
isoform:
all (-G)
A+D+G
B
C
D
E
F
G

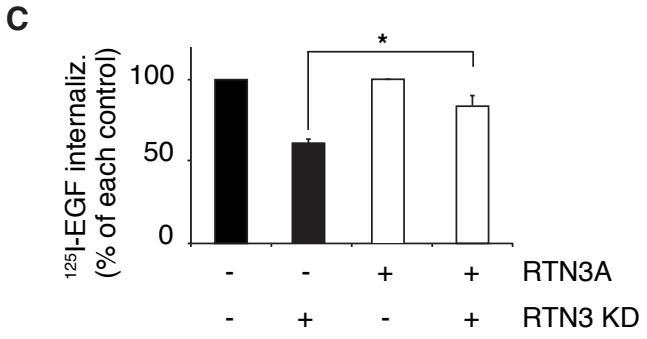
C
125I-EGF internaliz.
(% of each control)
100
50
0
*
- - + + RTN3A
- + - + RTN3 KD

Figure S8

Figure S8. Rescue of RTN3 phenotype.
(**A**) Scheme representing the *RTN3* gene and its 7 isoforms. On the left, isoform name and accession number are shown. The different exons are labeled with different colors and the corresponding number is indicated on the top. Oligos used to perform the qPCR shown in panel B are indicated with arrows in different colors, as explained in the legend at the bottom: green arrows indicate primers recognizing all isoforms except for isoform G; gray arrows indicate isoform-specific primers; red arrows indicate primers recognizing isoforms A, D and G. (**B**) Relative mRNA expression levels of the indicated isoforms were assessed by qPCR, normalized using a housekeeping gene (GAPDH) and expressed relative to levels detected with primers recognizing all isoforms (except isoform G). (**C**) RNAi resistant RTN3 isoform A was expressed in HeLa cells at endogenous levels (see Fig. 5C, bottom). Internalization constants were measured by ^{125}I-EGF internalization at high dose of ligand upon RTN3 KD or in control samples. Data are the mean ± SD and are normalized to each control clone. P-value was calculated by Two Tailed Student's t test. *, $P < 0.05$.

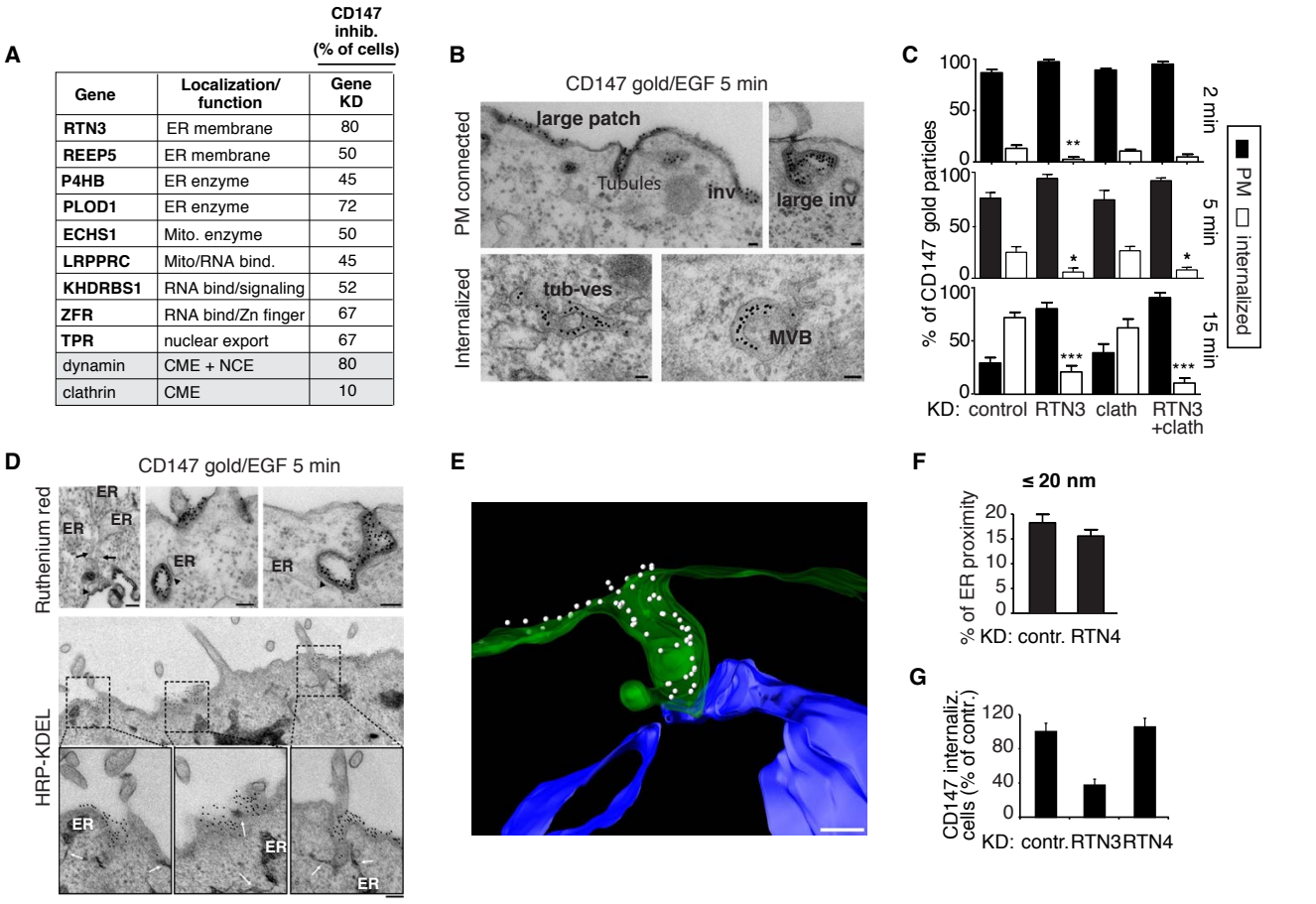

Figure S9

Figure S9. CD147 ultrastructural analysis. (**A**) The functional ablation of the 9 regulators of EGFR-NCE described in Fig. 2A was analyzed for its effect on CD147 internalization. The percentage of cells in which CD147 internalization was inhibited was calculated over at least 100 cells. Clathrin and dynamin are reported as controls. (**B**) Representative images of gold-CD147 positive internalizing structures after stimulation with high dose EGF for 5 min (see Materials and Methods for gold-CD147 labeling *in vivo*). PM was marked with ruthenium red (RuR) to discriminate invaginations still connected to the PM from internalized structures (see Materials and Methods). Upper panels depict structures still connected to the PM (RuR-positive), including patches and invaginations (inv). In lower panels, examples of gold-CD147 internalized structures (RuR-negative) are shown, including tubular vesicles (tub-ves) and multi-vesicular bodies (MVBs). Bars, 50 nm. (**C**) Quantitation of PM (RuR-positive) *vs.* internalized (RuR-negative) gold-labeled CD147 upon stimulation with high dose EGF for the indicated time points in the indicated conditions. Data are expressed as % ± SEM. P-values were calculated with One-way ANOVA. *, P <0.05; **, P <0.01; ***, P <0.001 (*vs.* control). (**D**) ER contacts with CD147-positive internalizing structures (5 min stimulation with high dose EGF). Top panels, examples of gold-CD147 positive structures (arrowheads) in close proximity to recognizable ER profiles (arrows). PM was marked with RuR as in (B). Bars, 100 nm. Middle panel, examples of ER contacts with CD147-positive internalizing structures after stimulation with high dose EGF for 5 min in HRP-KDEL transfected cells (see Materials and Methods). Bottom panels,

magnifications from the middle panel showing CD147-positive membrane domains close to ER profiles (white arrows). Only structures clearly connected to the PM were considered. Bottom images are also displayed in Fig. 5F. Bars, 100 nm. (**E**) 3D reconstruction of a CD147-positive (white dots) TI at the PM (green) in contact with the ER (blue). The 3D image represents the segmentation of the tomogram provided as Movie S1. Bar, 200 nm. (**F**) Mean frequency of the proximity between ER and CD147-positive structures, in control and RTN4 KD cells, stimulated with high dose EGF for 5 min. The number of CD147 clusters analyzed were: n=527 (control) and n=792 (RTN4 KD). Data are expressed as percentage ± SEM. (**G**) CD147 internalization was followed *in vivo* as in Fig. 5A in control and RTN4 KD cells (see also Materials and Methods). Quantification of the percentage of CD147 internalizing cells ± SD in different fields relative to control is indicated.

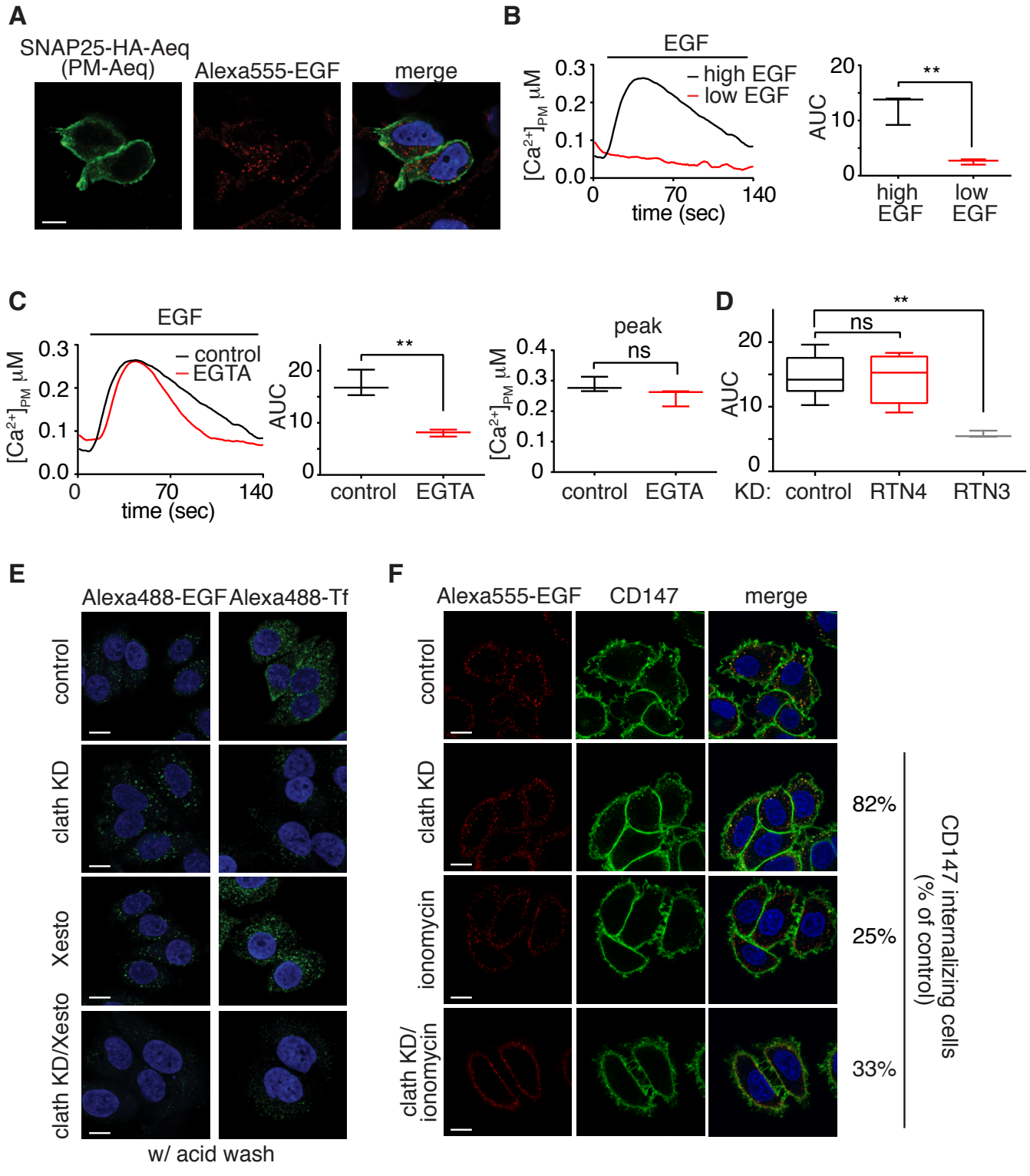
A
SNAP25-HA-Aeq
(PM-Aeq)
Alexa555-EGF
merge
B
EGF
– high EGF
– low EGF
[Ca2+]PM µM
time (sec)
AUC
high EGF
low EGF
C
EGF
– control
– EGTA
[Ca2+]PM µM
time (sec)
AUC
control
EGTA
peak
ns
D
ns
KD:
control
RTN4
RTN3
E
Alexa488-EGF
Alexa488-Tf
control
clath KD
Xesto
clath KD/Xesto
w/ acid wash
F
Alexa555-EGF
CD147
merge
control
clath KD
ionomycin
clath KD/
ionomycin
82%
25%
33%
CD147 internalizing cells
(% of control)

Figure S10

Figure S10. Additional calcium-based experiments. (**A**) HeLa cells were transfected with PM-aequorin construct (PM-Aeq, SNAP25 fusion protein with HA-tag; anti-HA in green, left panel) and stimulated with Alexa555-EGF (middle panel). Bar, 10 μm. Blue, DAPI. (**B**) Measurements of $[Ca^{2+}]_{PM}$ using PM-Aeq upon stimulation with high (100 ng/ml, black curve) or low (1 ng/ml, red curve) dose of EGF in control cells. The correspondent AUC in the two conditions is represented in the box plot on the right. P-values were calculated by Two Tailed Student's t test. **, $P < 0.01$. (**C**) Left, measurements of $[Ca^{2+}]_{PM}$ using PM-Aeq upon stimulation with high dose of EGF (100 ng/ml) in the presence or absence of extracellular calcium. Control cells where stimulated in saline buffer with calcium (black curve) or in saline buffer without calcium in presence of the extracellular calcium chelator EGTA (red curve). Note that the calcium peak is unaffected by the absence of extracellular Ca^{2+} (right panel), suggesting that EGTA is not altering EGF-induced calcium release. However, EGTA has an effect on the second phase of the curve (visible also AUC in the middle panel), which decays more abruptly. P-values were calculated by Two Tailed Student's t test. **, $P < 0.01$. For (B) and (C) representative curve for control is the same as Fig. 6A. (**D**) The area under the curve (AUC) of $[Ca^{2+}]_{PM}$ measurements determined using PM-Aeq upon stimulation with high dose of EGF (100 ng/ml) under the indicated conditions is shown in the box plots. P-values were calculated by One-way ANOVA. **, $P < 0.01$. ns, non-significant. (**E**) Control and clathrin KD cells, either untreated or treated with xestospongin C (Xesto) were stimulated with Alexa488-EGF (green, left panels) or Alexa488-Tf (green, right panels) for 8 min and subjected to acid wash before fixation. Note that xestospongin C treatment affects internalization in clathrin KD cells, where only NCE is active. Internalization of transferrin, taking place through CME, is unaffected by xestospongin C treatment. Bars, 10 μm. (**F**) CD147 (green) internalization was followed in control *vs.* clathrin KD cells, treated or not with ionomycin (see Materials and Methods) and stimulated with high dose of Alexa555-EGF for 8 min (red). CD147 internalization was affected by treatment with ionomycin, suggesting calcium requirement for NCE. Note that EGF internalization is inhibited in clathrin KD cells treated with ionomycin. Percentage of CD147-internalizing cells is shown on the right. Bars, 10 μm.

	Dyn1/2	Cav1	EndoA1/2	Rac1/2	Rho A	CDC42	GRAF1	Arf6	
EGFR-NCE	+	-	-	+	-	+	-	-	Our data
Ke (high EGF) of individual KDs in clathrin KD cells (Ke of clathrin KD alone = 0.09 ± 0.019)	**0.04**** ± 0.006	**0.07** ± 0.005	**0.12** ± 0.012	**0.04**** ± 0.014	**0.10** ± 0.034	**0.03***** ± 0.006	**0.07** ± 0.028	**0.07** ± 0.001	
Caveolar endocytosis	+	+							Literature's data
Macropinocytosis	-			+		+		+	
FEME/EndophilinA-dependent	+		+	+	+	+[#]			
CLIC/GEEK	-					+	+		
IL-2Rβ endocytosis	+			+	+				
Arf6-dependent	-							+	

+ = dependency - = independency

Table S1. Genetic requirements of EGFR-NCE compared to other clathrin-independent endocytic pathways.

The Table summarizes the dependency of clathrin-independent endocytic pathways on a number of endocytic proteins. In the boxes, "+" and "-" indicate dependency and independency, respectively; white boxes indicate "not tested".

Data for caveolar endocytosis [reviewed in (*53*)], macropinocytosis (*54-57*), FEME/EndoA2-dependent endocytosis (*3, 51*), CLIC/GEEK (*14, 15*), IL-2Rβ endocytosis (*58, 59*), and Arf6-dependent endocytosis (*22, 60*) were obtained from literature, as indicated.

Data for EGFR-NCE (*7, 8*) were obtained by *ad hoc* experiments performed in our laboratory. In particular, we performed functional ablation of the indicated endocytic proteins, in a clathrin KD background, followed by measurement of the internalization kinetics at high doses of EGF at different time points (2, 4 and 6 min). Data were plotted as the ratio between internalized and surface-bound radioactivity over time (see Materials and Methods). Endocytic rate constants (Ke) calculated from the slope of the trend-line are reported in the second line ± SD. Ke upon KD of the indicated proteins in condition of clathrin KD were compared to the Ke of clathrin KD alone (0.09 min^{-1}) to score for further reduction. From these calculations, it emerges that ablation of Dyn1/2, Rac1/2 and CDC42 affects EGFR-NCE to different extents. Note that Rac1/2 KD and CDC42 KD also decreased internalization at low EGF dose (our unpublished results) suggesting that they may have a general impact on EGFR endocytosis. [#]CDC42 has a role in FEME as a negative regulator of the pathway (*3*), while in EGFR-NCE and in the CLIC/GEEK acts as a positive regulator. P-values were calculated by Each Pair Student's t test. **, $P < 0.01$, ***, $P < 0.001$ (*vs.* clathrin KD).

From this analysis, it emerges that, at least under the experimental conditions employed here, EGFR-NCE does not resemble any of the other clathrin-independent pathways previously described.

	HeLa	HaCaT	BT20	A431
NCE activity	+	+	+	+
Surface EGFRs/cell	270,000	400,000	1,000,000	1,200,000
CD147 internalization (+ EGF)	+	+	+	+
CD147 intern. RTN3 KD (% of control)	15 ± 4.2***	38 ± 13***	18 ± 13***	39 ± 21***
EGF intern. clath KD or RTN3 KD (% of control)	58 ± 12*** 48 ± 15***	49 ± 24*** 44 ± 17***	65 ± 18*** 43 ± 21***	50 ± 23** 66 ± 41*
EGF intern. RTN3/clath KD (% of control)	8 ± 3***	13 ± 12***	20 ± 13***	24 ± 20**

Table S2. Relevance of EGFR/CD147-NCE in different cell lines.
Table summarizing the activation of EGFR/CD147-NCE in the indicated cell lines. CD147 and EGF internalization were followed by IF at the indicated time points, using a specific antibody for CD147 provided *in vivo* to the cells (see Materials and Methods), in the presence of Alexa-555 EGF for 8 min for HeLa and BT20 cells, 12 min for HaCaT and 20 min for A431 cells, taking in consideration the different internalization rate observed in the different lines. Quantitation of CD147 and EGF internalization was as in Fig. 5B and as described in Materials and Methods. Integrated fluorescence intensity was calculated on different fields of two independent experiments, and expressed as percentage of control ± SD. Reported P-values correspond to: RTN3 KD or clath KD *vs.* control; RTN3/clath KD *vs.* clath KD; P-values were calculated by Two Tailed Student's t test. *, $P < 0.05$, **, $P < 0.01$, ***, $P < 0.001$. Surface EGFR/cell were measured by ^{125}I-EGF saturation binding assay (see Materials and Methods). Level of clathrin KD and RTN3 KD was assessed by IB and was ≥ 80% in all the samples. In HeLa, HaCaT (immortalized human skin keratinocytes with no alteration of the EGFR locus), BT20 (breast tumor cells with *EGFR* amplification) and A431 (skin squamous carcinoma cells with *EGFR* amplification) cell lines, EGFR-NCE is active and dependent on RTN3 function, although to different extents. Furthermore, CD147 was internalized in an EGF- and RTN3-dependent manner.

Movie S1. ER tubules in contact with a CD147-positive TI. Single-tilted tomographic reconstruction (see Materials and Methods) of a TI—internalizing gold-labeled CD147—in contact with ER tubules. Note the contact of ER (pseudocolored in blue) profiles with the tip of the TI (the electron density on the PM is due to RuR staining). The 3D reconstruction, shown in Fig. S9E, was extracted from this movie.

Table S3. SILAC data.

Spreadsheet 1 (Unique>0; Peptides>1; RC>0). The MaxQuant software generates an output table named "proteingroup.txt" where all proteins identified and quantified, with corresponding SILAC protein ratios are listed. A summary of it is reported in ".excel" format with the following filter criteria: Proteins are reported if they contain at least 2 peptides (peptide>1), at least one of which unique (unique > 0), and if they have at least 1 ratio count (RC > 0). For each protein, the corresponding Gene Name, Uniprot Accession, Ratio H/L and Ratio H/L count are reported. EGFR protein is highlighted in blue.

Spreadsheet 2 (Protein Ratio Distribution). Histograms of log-transformed normalized H/L ratios for the three biological replicates. SILAC protein ratio distribution (PRD) for forward (Fwd) experiments 1 and 2 (H/L = stimulated cells/unstimulated cells) are displayed in the upper and middle panels, respectively, whereas PRD corresponding to reverse (Rev) experiment 3 (L/H = stimulated cells/unstimulated cells) is in the lower panel. Normalized ratios are transformed in $\log_2$ scale, with SILAC protein ratio reported as L/H in experiment 3. All PRDs are bimodal, with the Top 20% proteins highlighted in red. The dashed green line indicates the position of EGFR $\log_2$ protein ratio value in each experiment. The ratio count (RC) value for EGFR in each experiment is also reported.

Spreadsheet 3 (Top20%_RC>2_3 out of 3). 151 proteins corresponding to the Top 20% population are listed. These proteins were quantified in all three experiments (3 out of 3), have a minimum ratio count of 3 (RC > 2), and are ranked by decreasing ratio H/L expressed as the median value among the three experiments. The first 100 proteins (gene name labeled in red) were selected for further analysis. We included also one additional protein, namely, LRPPRC (at position 117), which appeared promising because it has an ENTH domain. Thus, a total of 101 proteins were tested in the RNAi-based functional validation screening.

Spreadsheet 4 (GOTERM-CC-FAT). Gene ontology analysis performed using the DAVID software (see Materials and Methods) on two unranked lists: the Top 20% gene list (as from spreadsheet 2) and the background (all proteins quantified RC > 2). From the analysis of the Cellular Components (CC), only the enriched GO terms with $*P < 0.01$ (1% FDR) are reported in the bottom graph, where P* is the adjusted *P* value using the Benjamini and Hochberg correction expressing the significance of enrichment of the Top 20% over the background.

Table S4. Validation screenings of NCE candidate genes.

Spreadsheet 1 (1st screening Summary). A summary of the first validation screening of SILAC candidates is reported. Details are in spreadsheet 2.

Spreadsheet 2 (1st screening Details). ^{125}I-labeled EGF internalization assays were performed upon KD of NCE candidate genes (101 SILAC genes) in HeLa-clone/clath-KD (described in Fig. S1, A to C). A custom library from Dharmacon, with SMART pools for every candidate gene was used (see Materials and Methods). Endocytic rates (K_e obs) expressed as percentage of K_e obs in control cells are reported (left, actual values; right graphical representation). In the graph, the black bars represent the controls used in the experiment. "Control": HeLa clone/clath-KD

cells not treated with doxy (i.e., still expressing clathrin); "dyn": HeLa clone/clath-KD cells not treated with doxy in which dynamin1/2 KD was performed; these two samples set the dynamic range of the experiment. Clathrin KD (-): HeLa clone/clath-KD cells treated with doxy (also shown by an arrow); this sample represents the reference value used to assign a "positive" or "negative" label to the candidates. "Positive" candidates (i.e., genes in which KD altered the internalization rates in doxy-treated cells, i.e., clathrin KD cells) correspond to genes whose ablation caused either a reduction of at least 1.5-fold (in red) or an increase of at least 1.5-fold (in blue). To avoid discarding potentially interesting borderline candidates, we also considered "mild decrease" candidates (in orange) that displayed a reduced internalization rate of 1.3- to 1.5-fold. All other candidates (in gray) were considered "negative" and discarded from further analyses.

Spreadsheet 3 (2nd screening Summary). A summary of the results from the second validation screening is reported. In this set of experiments (details are illustrated in spreadsheets 4 to 9), clathrin was transiently KD in HeLa cells (instead of using the HeLa clone), to avoid biases due to clonal differences. For each candidate gene, the SMART pool of 4 oligos was used, alone or in combination with clathrin KD. Dynamin KD was always used as control as it blocks both CME and NCE of EGFR and therefore sets the lowest threshold. The efficiency of KD was evaluated by real-time PCR (spreadsheet 4). The effect of the various KDs was tested on EGF internalization at low- and high-dose, on Tf internalization, and on surface EGFR levels (spreadsheets 5 to 8). Finally, deconvolution of the oligos in the pool was performed (spreadsheet 9). Also in this case, we applied the same cut-offs of the first validation screening (1.5-fold increase or decrease in the internalization rates, see spreadsheets 1 and 2). The summary table shows the effects of the KD of the indicated candidate genes on EGFR-NCE. The effect on EGFR-CME is also reported (middle column), as well as the results of the deconvolution experiment. Color code is as in spreadsheet 1 and refers to the original label given to each candidate in the first validation screening (used also in all subsequent spreadsheets). In the case of HSD17B10 and DDX39B, deconvolution was not performed (ND, not done), because these genes failed the specificity test for EGFRNCE because their KD also affected EGFR-CME. This does not imply that they have no role in EGFR-NCE but simply that their putative role is not specific for this form of endocytosis. Note also that PLOD1, the KD of which caused an increase in EGFR-NCE in the first screening, showed decreased internalization in this second validation. The reason for discrepancy between the second and the first screening is not clear, and might be due to technical problems or clonal variability. However, the results of the second screening, which were obtained in an exhaustive series of experiments, allowed us to include PLOD1 as a positive regulator of NCE.

Spreadsheet 4 (2nd screening_KD levels). The efficiency of different KDs, as assessed by qPCR, in the second screening are reported in the presence of concomitant transient clathrin KD; the level of clathrin KD in the different samples is also shown. Actual values are reported in the table on the left; graphical representations on the right. Data are normalized on GusB mRNA and expressed as a fraction of control.

Spreadsheet 5 (2nd screening_EGF low dose). Low-dose ^{125}I-labeled EGF internalization assays upon KD of the indicated candidates, alone or in combination with transient clathrin KD. Endocytic rate constants (K_e) were calculated from the slope of the trend-line at 2, 4, and 6 min after stimulation (Materials and Methods) and expressed as percentage of K_e in control cells. Actual values are reported in the table on the left; graphical representations are on the right.

Spreadsheet 6 (2nd screening_EGF high dose). High-dose ^{125}I-labeled EGF internalization assays upon KD of the indicated candidates, alone or in combination with transient clathrin KD. Endocytic rate constants (K_e obs) were calculated from the slope of the trend-line at 2, 4, and 6 min after stimulation and expressed as a percentage of K_e in control cells [Materials and Methods and (*8*)]. Actual values are reported in the table on the left; graphical representations are on the right.
Spreadsheet 7 (2nd screening_TfR). ^{125}I-labeled Tf internalization assays upon KD of the indicated candidates. K_e for each candidate is expressed as a percentage of K_e in control cells. Actual values are reported in the table on the left; graphical representations are on the right.
Spreadsheet 8 (2nd screening_EGFR surface). EGFR surface level measured by ^{125}I-labeled EGF saturation binding. Note that none of the KDs altered the number of EGFRs on the PM. Actual values are reported in the table on the left; graphical representations are on the right.
Spreadsheet 9 (2nd screening_Deconvolution). The 4 oligos contained in the original SMART pools were transfected singularly in combination with clathrin KD and their effect on EGFR-NCE pathway was assayed in ^{125}I-labeled EGF internalization assay at high EGF concentration. Data are expressed as K_e obs (% of control) as in spreadsheet 6. The efficiency of KD was assessed by qPCR and was expressed as in spreadsheet 4. From this analysis, we excluded two candidates, SNRPB and HNRNPU, which showed inconsistent results in the deconvolution experiment. Note that, in the case of RTN3 and REEP5, the validation was performed with an independent set of oligos, i.e., oligos not contained in the original SMART pool (see two panels below, and Materials and Methods).

REFERENCES

1. T. Kirchhausen, D. Owen, S. C. Harrison, Molecular structure, function, and dynamics of clathrin-mediated membrane traffic. *Cold Spring Harb. Perspect. Biol.* **6**, a016725 (2014). doi:10.1101/cshperspect.a016725 Medline

2. L. Johannes, R. G. Parton, P. Bassereau, S. Mayor, Building endocytic pits without clathrin. *Nat. Rev. Mol. Cell Biol.* **16**, 311–321 (2015). doi:10.1038/nrm3968 Medline

3. E. Boucrot, A. P. A. Ferreira, L. Almeida-Souza, S. Debard, Y. Vallis, G. Howard, L. Bertot, N. Sauvonnet, H. T. McMahon, Endophilin marks and controls a clathrin-independent endocytic pathway. *Nature* **517**, 460–465 (2015). doi:10.1038/nature14067 Medline

4. S. Sigismund, T. Woelk, C. Puri, E. Maspero, C. Tacchetti, P. Transidico, P. P. Di Fiore, S. Polo, Clathrin-independent endocytosis of ubiquitinated cargos. *Proc. Natl. Acad. Sci. U.S.A.* **102**, 2760–2765 (2005). doi:10.1073/pnas.0409817102 Medline

5. K. A. Lund, L. K. Opresko, C. Starbuck, B. J. Walsh, H. S. Wiley, Quantitative analysis of the endocytic system involved in hormone-induced receptor internalization. *J. Biol. Chem.* **265**, 15713–15723 (1990). Medline

6. J. D. Orth, E. W. Krueger, S. G. Weller, M. A. McNiven, A novel endocytic mechanism of epidermal growth factor receptor sequestration and internalization. *Cancer Res.* **66**, 3603–3610 (2006). doi:10.1158/0008-5472.CAN-05-2916 Medline

7. S. Sigismund, E. Argenzio, D. Tosoni, E. Cavallaro, S. Polo, P. P. Di Fiore, Clathrin-mediated internalization is essential for sustained EGFR signaling but dispensable for degradation. *Dev. Cell* **15**, 209–219 (2008). doi:10.1016/j.devcel.2008.06.012 Medline

8. S. Sigismund, V. Algisi, G. Nappo, A. Conte, R. Pascolutti, A. Cuomo, T. Bonaldi, E. Argenzio, L. G. G. C. Verhoef, E. Maspero, F. Bianchi, F. Capuani, A. Ciliberto, S. Polo, P. P. Di Fiore, Threshold-controlled ubiquitination of the EGFR directs receptor fate. *EMBO J.* **32**, 2140–2157 (2013). doi:10.1038/emboj.2013.149 Medline

9. G. Pines, W. J. Köstler, Y. Yarden, Oncogenic mutant forms of EGFR: Lessons in signal transduction and targets for cancer therapy. *FEBS Lett.* **584**, 2699–2706 (2010). doi:10.1016/j.febslet.2010.04.019 Medline

10. S. E. Ong, B. Blagoev, I. Kratchmarova, D. B. Kristensen, H. Steen, A. Pandey, M. Mann, Stable isotope labeling by amino acids in cell culture, SILAC, as a simple and accurate approach to expression proteomics. *Mol. Cell. Proteomics* **1**, 376–386 (2002). doi:10.1074/mcp.M200025-MCP200 Medline

11. G. K. Voeltz, W. A. Prinz, Y. Shibata, J. M. Rist, T. A. Rapoport, A class of membrane proteins shaping the tubular endoplasmic reticulum. *Cell* **124**, 573–586 (2006). doi:10.1016/j.cell.2005.11.047 Medline

12. Y. Shibata, C. Voss, J. M. Rist, J. Hu, T. A. Rapoport, W. A. Prinz, G. K. Voeltz, The reticulon and DP1/Yop1p proteins form immobile oligomers in the tubular endoplasmic reticulum. *J. Biol. Chem.* **283**, 18892–18904 (2008). doi:10.1074/jbc.M800986200 Medline

13. M. Kirkham, A. Fujita, R. Chadda, S. J. Nixon, T. V. Kurzchalia, D. K. Sharma, R. E. Pagano, J. F. Hancock, S. Mayor, R. G. Parton, Ultrastructural identification of uncoated

caveolin-independent early endocytic vehicles. *J. Cell Biol.* **168**, 465–476 (2005). doi:10.1083/jcb.200407078 Medline

14. S. Sabharanjak, P. Sharma, R. G. Parton, S. Mayor, GPI-anchored proteins are delivered to recycling endosomes via a distinct cdc42-regulated, clathrin-independent pinocytic pathway. *Dev. Cell* **2**, 411–423 (2002). doi:10.1016/S1534-5807(02)00145-4 Medline

15. R. Lundmark, G. J. Doherty, M. T. Howes, K. Cortese, Y. Vallis, R. G. Parton, H. T. McMahon, The GTPase-activating protein GRAF1 regulates the CLIC/GEEC endocytic pathway. *Curr. Biol.* **18**, 1802–1808 (2008). doi:10.1016/j.cub.2008.10.044 Medline

16. S. M. Ferguson, A. Raimondi, S. Paradise, H. Shen, K. Mesaki, A. Ferguson, O. Destaing, G. Ko, J. Takasaki, O. Cremona, E. O' Toole, P. De Camilli, Coordinated actions of actin and BAR proteins upstream of dynamin at endocytic clathrin-coated pits. *Dev. Cell* **17**, 811–822 (2009). doi:10.1016/j.devcel.2009.11.005 Medline

17. F. Giordano, Y. Saheki, O. Idevall-Hagren, S. F. Colombo, M. Pirruccello, I. Milosevic, E. O. Gracheva, S. N. Bagriantsev, N. Borgese, P. De Camilli, PI(4,5)P(2)-dependent and Ca(2+)-regulated ER-PM interactions mediated by the extended synaptotagmins. *Cell* **153**, 1494–1509 (2013). doi:10.1016/j.cell.2013.05.026 Medline

18. S. Carrasco, T. Meyer, STIM proteins and the endoplasmic reticulum-plasma membrane junctions. *Annu. Rev. Biochem.* **80**, 973–1000 (2011). doi:10.1146/annurev-biochem-061609-165311 Medline

19. T. Schikorski, S. M. Young Jr., Y. Hu, Horseradish peroxidase cDNA as a marker for electron microscopy in neurons. *J. Neurosci. Methods* **165**, 210–215 (2007). doi:10.1016/j.jneumeth.2007.06.004 Medline

20. L. Jozsef, K. Tashiro, A. Kuo, E. J. Park, A. Skoura, S. Albinsson, F. Rivera-Molina, K. D. Harrison, Y. Iwakiri, D. Toomre, W. C. Sessa, Reticulon 4 is necessary for endoplasmic reticulum tubulation, STIM1-Orai1 coupling, and store-operated calcium entry. *J. Biol. Chem.* **289**, 9380–9395 (2014). doi:10.1074/jbc.M114.548602 Medline

21. Q. Shi, Y. Ge, M. G. Sharoar, W. He, R. Xiang, Z. Zhang, X. Hu, R. Yan, Impact of RTN3 deficiency on expression of BACE1 and amyloid deposition. *J. Neurosci.* **34**, 13954–13962 (2014). doi:10.1523/JNEUROSCI.1588-14.2014 Medline

22. C. A. Eyster, J. D. Higginson, R. Huebner, N. Porat-Shliom, R. Weigert, W. W. Wu, R.-F. Shen, J. G. Donaldson, Discovery of new cargo proteins that enter cells through clathrin-independent endocytosis. *Traffic* **10**, 590–599 (2009). doi:10.1111/j.1600-0854.2009.00894.x Medline

23. M. J. Phillips, G. K. Voeltz, Structure and function of ER membrane contact sites with other organelles. *Nat. Rev. Mol. Cell Biol.* **17**, 69–82 (2016). doi:10.1038/nrm.2015.8 Medline

24. R. Marsault, M. Murgia, T. Pozzan, R. Rizzuto, Domains of high Ca2+ beneath the plasma membrane of living A7r5 cells. *EMBO J.* **16**, 1575–1581 (1997). doi:10.1093/emboj/16.7.1575 Medline

25. D. L. Bennett, T. R. Cheek, M. J. Berridge, H. De Smedt, J. B. Parys, L. Missiaen, M. D. Bootman, Expression and function of ryanodine receptors in nonexcitable cells. *J. Biol. Chem.* **271**, 6356–6362 (1996). doi:10.1074/jbc.271.11.6356 Medline

26. E. R. Eden, I. J. White, A. Tsapara, C. E. Futter, Membrane contacts between endosomes and ER provide sites for PTP1B-epidermal growth factor receptor interaction. *Nat. Cell Biol.* **12**, 267–272 (2010). Medline

27. F. G. Haj, P. J. Verveer, A. Squire, B. G. Neel, P. I. Bastiaens, Imaging sites of receptor dephosphorylation by PTP1B on the surface of the endoplasmic reticulum. *Science* **295**, 1708–1711 (2002). doi:10.1126/science.1067566 Medline

28. B. S. Kilpatrick, E. R. Eden, L. N. Hockey, E. Yates, C. E. Futter, S. Patel, An Endosomal NAADP-Sensitive Two-Pore Ca(2+) Channel Regulates ER-Endosome Membrane Contact Sites to Control Growth Factor Signaling. *Cell Reports* **18**, 1636–1645 (2017). doi:10.1016/j.celrep.2017.01.052 Medline

29. P. Sengupta, T. Jovanovic-Talisman, D. Skoko, M. Renz, S. L. Veatch, J. Lippincott-Schwartz, Probing protein heterogeneity in the plasma membrane using PALM and pair correlation analysis. *Nat. Methods* **8**, 969–975 (2011). doi:10.1038/nmeth.1704 Medline

30. E. Aboud-Pirak, E. Hurwitz, M. E. Pirak, F. Bellot, J. Schlessinger, M. Sela, Efficacy of antibodies to epidermal growth factor receptor against KB carcinoma in vitro and in nude mice. *J. Natl. Cancer Inst.* **80**, 1605–1611 (1988). doi:10.1093/jnci/80.20.1605 Medline

31. K. J. Shin, E. A. Wall, J. R. Zavzavadjian, L. A. Santat, J. Liu, J.-I. Hwang, R. Rebres, T. Roach, W. Seaman, M. I. Simon, I. D. C. Fraser, A single lentiviral vector platform for microRNA-based conditional RNA interference and coordinated transgene expression. *Proc. Natl. Acad. Sci. U.S.A.* **103**, 13759–13764 (2006). doi:10.1073/pnas.0606179103 Medline

32. C. C. Uphoff, H. G. Drexler, Comparative PCR analysis for detection of mycoplasma infections in continuous cell lines. *In Vitro Cell. Dev. Biol. Anim.* **38**, 79–85 (2002). doi:10.1290/1071-2690(2002)038<0079:CPAFDO>2.0.CO;2 Medline

33. P. J. Peters, M. Gao, J. Gaschet, A. Ambach, E. van Donselaar, J. F. Traverse, E. Bos, E. J. Wolffe, V. W. Hsu, Characterization of coated vesicles that participate in endocytic recycling. *Traffic* **2**, 885–895 (2001). doi:10.1034/j.1600-0854.2001.21204.x Medline

34. J. Rappsilber, M. Mann, Y. Ishihama, Protocol for micro-purification, enrichment, pre-fractionation and storage of peptides for proteomics using StageTips. *Nat. Protoc.* **2**, 1896–1906 (2007). doi:10.1038/nprot.2007.261 Medline

35. J. Cox, M. Mann, MaxQuant enables high peptide identification rates, individualized p.p.b.-range mass accuracies and proteome-wide protein quantification. *Nat. Biotechnol.* **26**, 1367–1372 (2008). doi:10.1038/nbt.1511 Medline

36. D. N. Perkins, D. J. Pappin, D. M. Creasy, J. S. Cottrell, Probability-based protein identification by searching sequence databases using mass spectrometry data. *Electrophoresis* **20**, 3551–3567 (1999). doi:10.1002/(SICI)1522-2683(19991201)20:18<3551:AID-ELPS3551>3.0.CO;2-2 Medline

37. A. I. Nesvizhskii, Protein identification by tandem mass spectrometry and sequence database searching. *Methods Mol. Biol.* **367**, 87–119 (2007). Medline

38. A. I. Nesvizhskii, O. Vitek, R. Aebersold, Analysis and validation of proteomic data generated by tandem mass spectrometry. *Nat. Methods* **4**, 787–797 (2007). doi:10.1038/nmeth1088 Medline

39. L. Penengo, M. Mapelli, A. G. Murachelli, S. Confalonieri, L. Magri, A. Musacchio, P. P. Di Fiore, S. Polo, T. R. Schneider, Crystal structure of the ubiquitin binding domains of rabex-5 reveals two modes of interaction with ubiquitin. *Cell* **124**, 1183–1195 (2006). doi:10.1016/j.cell.2006.02.020 Medline

40. J. Schindelin, I. Arganda-Carreras, E. Frise, V. Kaynig, M. Longair, T. Pietzsch, S. Preibisch, C. Rueden, S. Saalfeld, B. Schmid, J.-Y. Tinevez, D. J. White, V. Hartenstein, K. Eliceiri, P. Tomancak, A. Cardona, Fiji: An open-source platform for biological-image analysis. *Nat. Methods* **9**, 676–682 (2012). doi:10.1038/nmeth.2019 Medline

41. J. Schindelin, C. T. Rueden, M. C. Hiner, K. W. Eliceiri, The ImageJ ecosystem: An open platform for biomedical image analysis. *Mol. Reprod. Dev.* **82**, 518–529 (2015). doi:10.1002/mrd.22489 Medline

42. E. F. Meijering, FeatureJ: An ImageJ Plugin Suite for Image Feature Extraction (Erasmus Univ. Medical Center, Rotterdam, The Netherlands); https://imagescience.org/meijering/software/featurej/.

43. M. Heilemann, S. van de Linde, M. Schüttpelz, R. Kasper, B. Seefeldt, A. Mukherjee, P. Tinnefeld, M. Sauer, Subdiffraction-resolution fluorescence imaging with conventional fluorescent probes. *Angew. Chem. Int. Ed.* **47**, 6172–6176 (2008). doi:10.1002/anie.200802376 Medline

44. R. E. Thompson, D. R. Larson, W. W. Webb, Precise nanometer localization analysis for individual fluorescent probes. *Biophys. J.* **82**, 2775–2783 (2002). doi:10.1016/S0006-3495(02)75618-X Medline

45. G. T. Dempsey, J. C. Vaughan, K. H. Chen, M. Bates, X. Zhuang, Evaluation of fluorophores for optimal performance in localization-based super-resolution imaging. *Nat. Methods* **8**, 1027–1036 (2011). doi:10.1038/nmeth.1768 Medline

46. F. S. Wouters, P. J. Verveer, P. I. Bastiaens, Imaging biochemistry inside cells. *Trends Cell Biol.* **11**, 203–211 (2001). doi:10.1016/S0962-8924(01)01982-1 Medline

47. J. W. Slot, H. J. Geuze, Cryosectioning and immunolabeling. *Nat. Protoc.* **2**, 2480–2491 (2007). doi:10.1038/nprot.2007.365 Medline

48. M. Puhka, M. Joensuu, H. Vihinen, I. Belevich, E. Jokitalo, Progressive sheet-to-tubule transformation is a general mechanism for endoplasmic reticulum partitioning in dividing mammalian cells. *Mol. Biol. Cell* **23**, 2424–2432 (2012). doi:10.1091/mbc.E10-12-0950 Medline

49. M. Bonora, C. Giorgi, A. Bononi, S. Marchi, S. Patergnani, A. Rimessi, R. Rizzuto, P. Pinton, Subcellular calcium measurements in mammalian cells using jellyfish photoprotein aequorin-based probes. *Nat. Protoc.* **8**, 2105–2118 (2013). doi:10.1038/nprot.2013.127 Medline

50. P. Pinton, T. Pozzan, R. Rizzuto, The Golgi apparatus is an inositol 1,4,5-trisphosphate-sensitive Ca2+ store, with functional properties distinct from those of the endoplasmic reticulum. *EMBO J.* **17**, 5298–5308 (1998). doi:10.1093/emboj/17.18.5298 Medline

51. H. F. Renard, M. Simunovic, J. Lemière, E. Boucrot, M. D. Garcia-Castillo, S. Arumugam, V. Chambon, C. Lamaze, C. Wunder, A. K. Kenworthy, A. A. Schmidt, H. T. McMahon, C. Sykes, P. Bassereau, L. Johannes, Endophilin-A2 functions in membrane scission in clathrin-independent endocytosis. *Nature* **517**, 493–496 (2015). doi:10.1038/nature14064 Medline

52. R. Lakshminarayan, C. Wunder, U. Becken, M. T. Howes, C. Benzing, S. Arumugam, S. Sales, N. Ariotti, V. Chambon, C. Lamaze, D. Loew, A. Shevchenko, K. Gaus, R. G. Parton, L. Johannes, Galectin-3 drives glycosphingolipid-dependent biogenesis of clathrin-independent carriers. *Nat. Cell Biol.* **16**, 595–606 (2014). doi:10.1038/ncb2970 Medline

53. R. G. Parton, M. A. del Pozo, Caveolae as plasma membrane sensors, protectors and organizers. *Nat. Rev. Mol. Cell Biol.* **14**, 98–112 (2013). doi:10.1038/nrm3512 Medline

54. J. A. Swanson, Shaping cups into phagosomes and macropinosomes. *Nat. Rev. Mol. Cell Biol.* **9**, 639–649 (2008). doi:10.1038/nrm2447 Medline

55. E. Frittoli, A. Palamidessi, A. Pizzigoni, L. Lanzetti, M. Garrè, F. Troglio, A. Troilo, M. Fukuda, P. P. Di Fiore, G. Scita, S. Confalonieri, The primate-specific protein TBC1D3 is required for optimal macropinocytosis in a novel ARF6-dependent pathway. *Mol. Biol. Cell* **19**, 1304–1316 (2008). doi:10.1091/mbc.E07-06-0594 Medline

56. W. S. Garrett, L.-M. Chen, R. Kroschewski, M. Ebersold, S. Turley, S. Trombetta, J. E. Galán, I. Mellman, Developmental control of endocytosis in dendritic cells by Cdc42. *Cell* **102**, 325–334 (2000). doi:10.1016/S0092-8674(00)00038-6 Medline

57. D. A. Schafer, C. D'Souza-Schorey, J. A. Cooper, Actin assembly at membranes controlled by ARF6. *Traffic* **1**, 892–903 (2000). doi:10.1034/j.1600-0854.2000.011108.x Medline

58. C. Lamaze, A. Dujeancourt, T. Baba, C. G. Lo, A. Benmerah, A. Dautry-Varsat, Interleukin 2 receptors and detergent-resistant membrane domains define a clathrin-independent endocytic pathway. *Mol. Cell* **7**, 661–671 (2001). doi:10.1016/S1097-2765(01)00212-X Medline

59. A. Grassart, A. Dujeancourt, P. B. Lazarow, A. Dautry-Varsat, N. Sauvonnet, Clathrin-independent endocytosis used by the IL-2 receptor is regulated by Rac1, Pak1 and Pak2. *EMBO Rep.* **9**, 356–362 (2008). doi:10.1038/embor.2008.28 Medline

60. N. Naslavsky, R. Weigert, J. G. Donaldson, Characterization of a nonclathrin endocytic pathway: Membrane cargo and lipid requirements. *Mol. Biol. Cell* **15**, 3542–3552 (2004). doi:10.1091/mbc.E04-02-0151 Medline